Structural Studies of Prions and Prion Protein Polymorphisms in Chronic Wasting Disease

by

Sara Amidian

A thesis submitted in partial fulfillment of the requirements for the degree of

Doctor of Philosophy

Department of Biochemistry
University of Alberta

ABSTRACT

Prion diseases are a group of deadly neurological disorders caused by the abnormal folding of the prion protein into an infectious form known as PrP^{Sc}. Chronic wasting disease is a prion disease affecting cervids such as deer, elk, moose, and reindeer. Despite ongoing efforts to understand prion transmission barriers and ensure public health, the appearance of animal prion strains with zoonotic potential is a major concern. Therefore, a crucial element in addressing this concern is to understand the structure of PrP^{Sc} which can contribute to developing strategies aimed at preventing the accumulation and replication of PrP^{Sc}. To date, no structural investigations have been conducted on *ex-vivo* CWD prions. Moreover, due to the inherent flexibility of the N-terminal region of prions, there is a lack of structural data regarding this region across all prion strains. Therefore, in the first part of this study, electron microscopy was used to study the full-length and N-terminally truncated forms of chronic wasting disease (CWD) prions purified from the brains of CWD-positive tg33 mice and white-tailed deer. The CWD prions were found to be morphologically heterogeneous with larger diameters compared to other prion strains. Interestingly, the full-length CWD prion fibrils were decorated with striations while the N-terminally truncated form were not. This suggests a potential correlation between the striations and the N-terminal region of the CWD prions. This observation was likely made possible by the incorporation of ethylenediaminetetraacetic acid (EDTA) during the purification process. EDTA can remove cations that engage with the N-terminus, potentially allowing the N-terminus to independently structure itself, thereby becoming visible for

the first time. This finding opens the door to further investigating the N-terminal region of the prions.

Another interesting phenomenon in prion disease involves the polymorphisms found in the prion protein sequence, which can influence the susceptibility of animals to chronic wasting disease. In the second part of this research, we investigated the effect of white-tailed deer polymorphisms on the structure and stability of prion protein. We performed all-atom molecular dynamics simulations to study the structure and stability of white-tailed deer prion protein for wild type and three polymorphisms: 95H, 96S, and 116G. We demonstrated that proteins carrying polymorphisms display significant differences when compared to wild type protein. The root mean square deviation and radius of gyration calculations illustrated that the conformations in wild type prion protein, 95H, 96S, and 116G are unique and distinct from one another. Additional analyses were conducted by comparing the main-chain flexibility and distance maps of the prion protein residues. Several regions in 96S and 116G became less stable, in contrast to 95H, where increased stability was observed. Hydrogen bond and salt bridge calculations showed 95H, 96S, and 116G affected the bonding patterns within the prion protein structures as compared to the wild type. However, changes in the solvent-accessible surfaces were more substantial indicating that the polymorphisms most probably dictated their dynamic changes by altering the hydrophobic interactions. Using *in vitro* aggregation assay, we also demonstrated an opposite effect of these polymorphisms on the aggregation propensity of deer prion protein, with 95H favoring and 96S delaying its aggregation.

The structural and dynamical descriptors investigated in this study and the differences seen between the simulated structures may aid in better understanding how polymorphisms can affect CWD transmission.

PREFACE

This thesis is an original work of Sara Amidian, under the supervision of Dr. Holger Wille. Chapter 1 includes a general introduction and Chapter 4 is the overall conclusion and future directions.

Parts of Chapter 1 have been published by Wille, H., Dorosh, L., **Amidian, S**., Schmitt-Ulms, G., & Stepanova, M. (2019). "Combining molecular dynamics simulations and experimental analyses in protein misfolding" Advances in protein chemistry and structural biology, 118, 33–110.

The experiments presented in Chapter 2 are my original work, except for the bioassay experiments, which were conducted by Brian Tancowny and Chiye Kim, and the immunogold labelling experiment, performed by Dr. Vineet Subhash Rathod.

In Chapter 3, all the data is my original work, except for the real-time quaking-induced conversion assay, which was carried out by Dr. Leonardo M. Cortez and the recombinant deer PrP utilized in this study was graciously provided by the late Dr. Jose Miguel Flores-Fernandez. Figure 3-3 was crafted by Dr. Holger Wille, and I extend my gratitude to Dr. Lyudmyla Dorosh for her valuable assistance in facilitating the analysis of the molecular dynamics trajectories by generating scripts.

All the projects that required the use of animals received animal research ethics approval from the University of Alberta Animal Care and Use Committee and followed the guidelines provided by the Canadian Council on Animal Care. The research

protocols of these results were approved under AUP00000884 "Structural biology of infectious mammalian."

DEDICATION

To my beloved Mohammad, the anchor of my soul and the wind beneath my wings and to our 4AA.

This work is also dedicated to the brilliant minds unjustly denied the pursuit of their dreams.

ACKNOWLEDGEMENTS

I want to start by expressing my heartfelt gratitude to my mentor, Dr. Holger Wille. The transformation he enabled is something I'm profoundly thankful for. His trust in his students has nurtured our growth, and his dedication to our development as researchers has been a true inspiration. The words feel inadequate, but thank you, Dr. Holger Wille, for everything.

Next, I would like to extend my sincere appreciation to my supervisory committee members, Dr. Judd Aiken and Dr. Howard Young. Their consistent availability and willingness to address my inquiries have been invaluable. Dr. Young's expertise in teaching image processing techniques has been instrumental to my project. I'm also sincerely thankful to Dr. Juan Duque Velasquez, from the laboratory of Dr. Judd Aiken and Dr. Debbie McKenzie for providing the CWD-positive tg33 mice and white-tailed deer brains that played a vital role in my project.

A profound thank you extends to Dr. Nicolas Touret of the University of Alberta and Dr. Christina Sigurdson of the University of California San Diego for generously sparing their time and kind willingness to be on my PhD examining committee.

The Department of Biochemistry deserves special gratitude, with a heartfelt thanks to Dr. David Stuart, our graduate coordinator. The past and present program advisors – Kelsey Robertson, Kimberly Arndt, and Lisa Dublin – have been my guiding lights.

I'm indebted to Dr. Lyudmyla (Luda) Dorosh and Dr. Maria Stepanova for their unwavering support in my molecular dynamics simulation project. Luda, beyond being a remarkable collaborator and mentor, you've become a treasured friend. I am eternally grateful for all you taught me. Also, I would like to thank Dr. Leonardo M. Cortez and Dr. Jose Miguel Flores-Fernandez (RIP) for performing the real-time quaking-induced conversion assay, which was a great addition to my molecular dynamics study of the PrP polymorphisms.

Furthermore, heartfelt gratitude is extended to Dr. Xinli (Lili) for supplying the D 15.15 antibody, and to Dr. Adrianno Aguzzi from the University of Zürich and Dr. Vineet Subhash Rathod for providing the Fab3, Fab 29, and Fab69 antibodies. Dr. Rathod also conducted the immunogold labelling experiments presented in this thesis. Vineet, your contributions extend beyond research to the cherished friendship we've built.

To the incredible Wille lab team, including Dr. Vineet Subhash Rathod, Dr. Lyudmyla Dorosh, Dr. Jose Flores Fernandez (RIP), Aishwarya Sriraman, Dr. Xinli (Lili) Tang, Dr. Andrew Fang, Dr. Serene Wohlgemuth, Madeleine Fleming, Dr. Aliza Borenstein-Katz, and Brian Tancowny. Whether it was troubleshooting experiments together, or simply sharing a laugh during coffee breaks, your presence has enriched my experience and made the challenges much more manageable. I extend my gratitude to the former members of the Wille lab, specifically Dr. Maria Carmen (Mamen) Garza-Garcia, Dr. Ester Vázquez-Fernández, and Dr. Xiongyao Wang. Mamen, a remarkable individual to work with, played a pivotal role in teaching me the intricacies of protein purification. Ester shared her expertise in image processing and I'm grateful for the opportunity to learn from her. Xiongyao guided me in learning the use of the electron microscope.

The laughter we've shared and the heartfelt conversations we've exchanged have genuinely been a ray of light in my days. Through every high and low, your support has been a constant source of strength, and I am deeply thankful to you.

I extend my gratitude to the entire team at the Centre for Prions and Protein Folding Diseases. I'd like to give special recognition to those who have played a significant role in shaping my journey. Dr. Debbie McKenzie, your kindness brightened my days and uplifted my spirit. Dr. David Westaway, your feedback has been an invaluable compass guiding me to elevate my performance and research. Also, I would like to thank Klinton Shmeit for his unwavering support and dependable presence whenever assistance was needed.

I would like to dedicate a special note of gratitude to my parents, Tooba Jafari and Dr. Ali Asghar Amidian, whose boundless love has been the cornerstone of my journey. I am forever grateful for your unwavering presence, sacrifices, and the foundation of love and support that you've provided throughout my life. This accomplishment is as much yours as it is mine.

A special shoutout goes to my sister and lifelong best friend, Hajar, my beloved niece, Hannah (my bundle of joy) and my awesome brother, Amin. You three are my turbo boosters. The love and appreciation I have for you is beyond measure. Thank you for simply existing in my life.

Lastly, with all my heart, I want to thank my buddy, my absolute rock, and my teammate—Mohammad. Words can't capture how thankful I am for you. In those quieter moments, I find myself thinking about all the times you've had my back and the simple joy of having you by my side. You are the bright spark in my life, my go-to person, and the reason I keep pushing forward. Thank you, my love.

TABLE OF CONTENT

LIST OF TABLES

LIST OF FIGURES

LIST OF SUPPLEMENTARY FIGURES

ABBREVIATIONS

2D: two-dimensional

3D: three-dimensional

4RβS: 4-rung beta solenoid

BSA: Bovine serum albumin

BSE: bovine spongiform encephalopathy

CD: circular dichroism

CDI: conformation-dependent immunoassay

CJD: Creutzfeldt-Jakob disease

CWD: chronic wasting disease

EDTA: ethylenediaminetetraacetic acid

EM: electron microscopy

FFI: fatal familial insomnia

FT: Fourier Transform

FTIR: Fourier-transform infrared spectroscopy

fCJD: familial Creutzfeldt-Jakob disease

GPI: glycosyl-phosphatidylinositol

GSS: Gerstmann-Sträussler-Scheinker disease

HB: hydrogen bond

HR: hydrophobic region

H/D: hydrogen/deuterium

IC: intra-cerebrally

iCJD: iatrogenic Creutzfeldt-Jakob disease

MD: molecular dynamics

MBM: meat-and-bone meals

OR: octapeptide repeat region

PBS: phosphate-buffered saline

PDB: protein databank

PE: pronase E

PIRIBS: parallel in-register intermolecular β-sheet

PK: proteinase K

PMSF: phenylmethylsulfonyl fluoride

PrP: prion protein

PRNP: human prion protein gene

Prnp: animal prion protein gene

***Prnp*$^{0/0}$**: lacking the Prnp gene

PTA: phosphotungstate anion

Rg: radius of gyration

RMSD: root-mean-square deviation

RMSF: root-mean-square fluctuation

RT-QuIC: real-time quaking-induced conversion assay

SASA: solvent accessible surface area

SB: salt bridges

sCJD: sporadic Creutzfeldt-Jakob disease

SDS: sodium dodecyl sulfate

SDS PAGE: Sodium dodecyl sulfate polyacrylamide gel electrophoresis

SS: secondary structure

ssNMR: solid-state nuclear magnetic resonance spectroscopy

TBS: tris-buffered saline

TME: transmissible mink encephalopathy

TSE: transmissible spongiform encephalopathies

vCJD: variant Creutzfeldt-Jakob disease

VMD: Visual Molecular Dynamics software

WT: wild type

WTD: white-tailed deer

XRD: X-ray diffraction

AMINO ACIDS

Alanine: A

Arginine: R

Asparagine: N

Aspartic Acid: D

Cysteine: C

Glutamine: Q

Glutamic Acid: E

Glycine: G

Histidine: H

Isoleucine: I

Leucine: L

Lysine: K

Methionine: M

Phenylalanine: F

Proline: P

Serine: S

Threonine: T

Tryptophan: W

Tyrosine: Y

Valine: V

Chapter 1: Introduction

1.1 INTRODUCTION TO PRION DISEASES

Proteins are complex macromolecules that play critical roles in numerous cellular processes. Protein structure, function, and stability are closely interrelated and, therefore, any perturbations in the structural properties of a protein can lead to protein misfolding and associated diseases. Often, misfolded proteins cannot perform their intended functions, leading to a "loss of function" phenotype. However, misfolded proteins may also result in a toxic "gain of function" phenotype that can lead to cell death or disease complications.

The prion protein (PrP), a glycosyl-phosphatidylinositol (GPI) anchored glycoprotein, is an example of a protein that can misfold and induce the misfolding of other prion proteins, leading to neurodegenerative disorders known as transmissible spongiform encephalopathies (TSEs) or prion diseases. The origins of prion disease can be traced back to the 18th century when scrapie was first identified in sheep, initially thought to be caused by a "slow virus" (Eklund et al. 1967). In 1959, it was discovered that Creutzfeldt-Jakob disease (CJD) and Kuru, both of which affect humans, shared similar neuropathologies (Klatzo et al. 1959). William Hadlow recognized that these pathological features were also found in the brains of sheep infected with scrapie, which was already known to be a transmissible disease (Hadlow 1959). This led to the proposal that Kuru and CJD were also transmissible, which was subsequently confirmed (Gibbs et al. 1994). The discovery that the agents responsible for scrapie and CJD were resistant to nucleic acid-destroying procedures such as ultraviolet and ionizing radiation led to the recognition of a new class of

pathogens (Alper et al. 1967, Gibbs et al. 1978). Dr. Stanley B. Prusiner proposed a ground-breaking hypothesis in 1982, suggesting that a new class of infectious agents, consisting solely of protein molecules, was responsible for scrapie disease. He coined the term "proteinaceous infectious particle" or "prion" to describe this novel pathogen (Prusiner 1982).

1.2 THE CELLULAR PRION PROTEIN

The *PRNP* gene, located on chromosome 20 in humans, encodes for the cellular prion protein (PrP^C). PrP^C is a glycoprotein that is predominantly expressed in the central nervous system but is also found in other tissues. The mature human PrP^C is composed of approximately 210 amino acid residues and consists of two domains: an unstructured N-terminal domain (residues 23-120, human numbering) and a structured C-terminal domain (residues 121-231, human numbering) (Riek et al. 1996). The N-terminal region consists of two charged clusters, CC1 and CC2, an octapeptide repeat region (OR), and a hydrophobic region (HR) (Aguzzi et al. 2008). The OR is a repetitive sequence of eight amino acids (PHGGGWGQ) that occurs four times and serves a critical function in coordinating divalent anions, particularly copper and zinc. This region has been shown to contribute to the pathogenic transformation of the prion protein into the infectious form, PrP^{Sc} (Millhauser 2023).

The C-terminal domain of PrP consists of three α-helices, two β-strands, a disulfide bond, and two N-glycans (Figure 1-1) (Turk et al. 1988). The two possible

glycosylation sites can result in un-, mono-, or di-glycosylated forms of PrP. Additionally, PrP is attached to the cell membrane's outer surface through a GPI anchor (Figure 1-1) (Stahl et al. 1987).

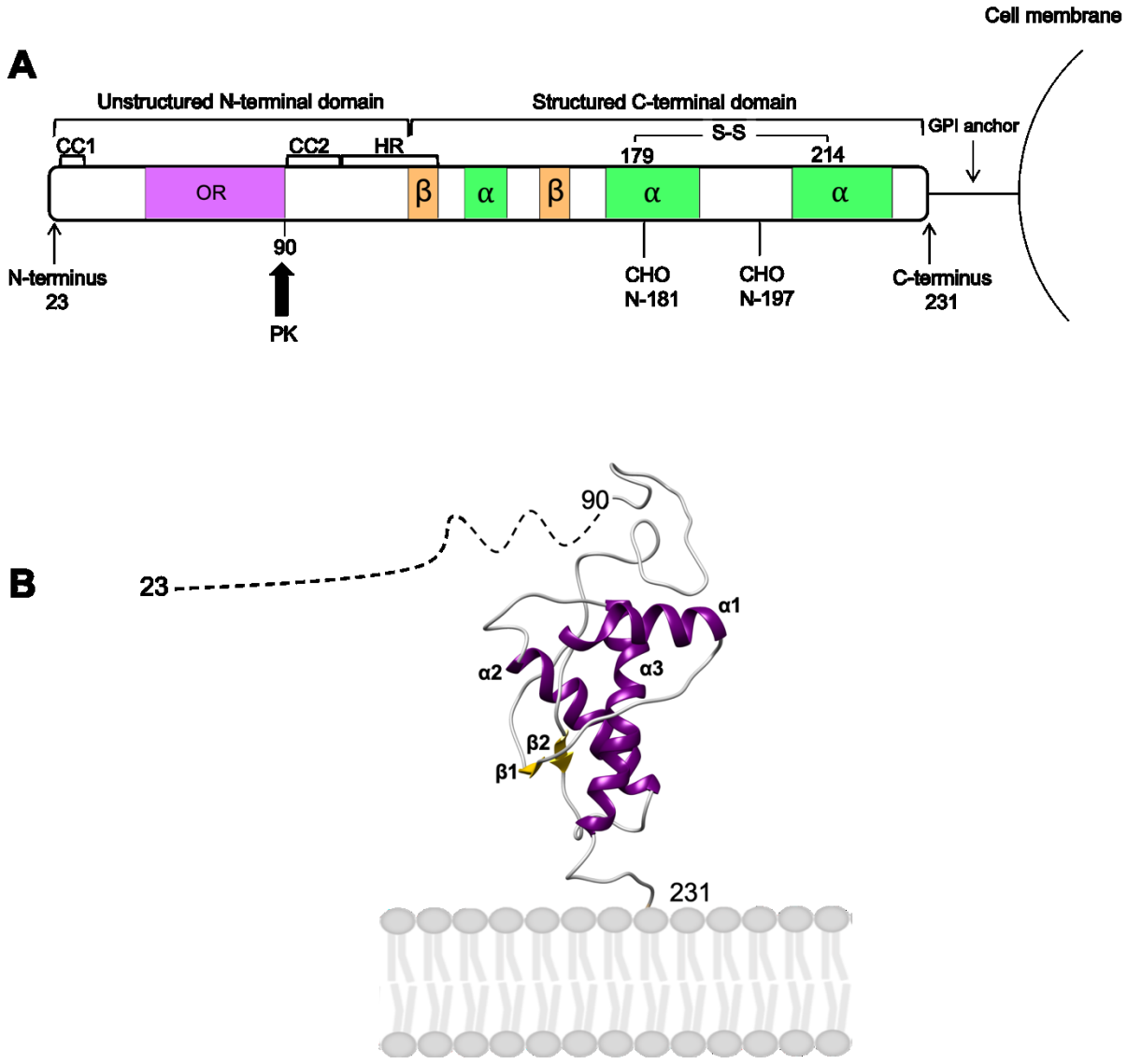

Figure 1-1. Schematic Representation of PrP^{C} Structure. (**A**) Mature PrP^{C}, which consists of approximately 210 amino acids, can be divided into two distinct domains: the N-terminal disordered domain and the structured C-terminal domain. The flexible

N-terminal region comprises two charged clusters, CC1 and CC2, an octapeptide repeat region (OR), and a hydrophobic region (HR). The C-terminal domain is composed of three α-helices, two β-sheets, a disulfide bond, and two N-glycans (CHO; positions 181 and 197). The figure is adapted from Kovač et al. (2022), and the numbering corresponds to the human PrP sequence. (**B**) The three-dimensional structure of PrP^{C} is illustrated. The coordinates for residues 124 to 231 were obtained from the PDB ID: 4YXH (Baral et al. 2015).

Over the past two decades, research has shown that PrP^{C} plays significant roles in the brain including supporting myelin development (Bremer et al. 2010), promoting neuron development (Kanaani et al. 2005), and protecting nerve cells from chemical and oxidative damage (Klamt et al. 2001). Although PrP^{C} cannot be identified as having a sole function like a signaling molecule, enzyme, or transporter, it is essential for proper neurological function (Kovač and Čurin Šerbec 2022). It is noteworthy that most studies investigating its role have associated PrP^{C} with metal ion binding, especially to copper and zinc (Salzano et al. 2019, Millhauser 2023).

1.3 THE INFECTIOUS PRION PROTEIN

Prion diseases can arise sporadically, be acquired, or result from a genetic mutation (Prusiner 1998). In these diseases, PrP^{C} undergoes a conformational change to its infectious form, referred to as PrP^{Sc} or prions (Prusiner 1998). Although the primary structure remains the same, the secondary, tertiary, and quaternary structures of PrP^{Sc} differ from PrP^{C}. The acronym "Sc" in PrP^{Sc} originates from scrapie, the first identified prion disease (Prusiner 1998).

The exact mechanism for the conversion from PrP^{C} to PrP^{Sc} is not fully understood but it is thought to involve a template-assisted process, in which PrP^{Sc} acts as a seed that triggers the misfolding of PrP^{C} (section 1.4). Compared to PrP^{C}, PrP^{Sc} has a higher beta-sheet content (section 1.9) that promotes its aggregation into amyloid fibrils, which are highly resistant to degradation and can accumulate in various tissues, primarily in the central nervous system (Prusiner 1982). Accumulation of PrP^{Sc} can cause neuronal loss, astrogliosis, and spongiform changes in the brain tissue, leading to the clinical symptoms of TSEs such as neurological and cognitive dysfunction (Prusiner et al. 1998).

Prion diseases are invariably fatal to both animals and humans and no effective treatments or vaccines are currently available.

1.3.1 PrP 27-30 or PK-resistant PrP^{Sc}

The identification of PrP^{Sc} is typically achieved through infectivity bioassays, although this method is limited by the long incubation periods. Alternatively, the insolubility and partial resistance of PrP^{Sc} to proteolysis is utilized to identify its presence in a given sample. This partial resistance is specifically observed with proteinase K (PK) treatment which forms the basis of the tests developed for its detection. Unlike PrP^{C}, PrP^{Sc} is not completely digested by PK due to its preceding conformational changes. Instead, when subjected to PK digestion, an undigested fragment, approximately entailing residues around 90 through to the C-terminus remains intact. This PK-

resistant form of the prion protein has an apparent molecular mass of 27–30 kDa and is thus referred to as PrP 27-30, (Bolton et al. 1982). PrP 27-30 retains its infectious properties and can form three bands on a western blot, corresponding to the un-, mono-, and di-glycosylated isoforms of the prion protein (Weissmann 2004).

1.3.2 Protease-sensitive PrP^{Sc}

Early studies initially suggested that infectivity in certain prion disease cases was present without any noticeable PK-resistant material, leading to the mistaken belief that PrP^{Sc} was absent (Lasmézas et al. 1997). However, subsequent investigations by Safar et al. revealed that a proportion of PrP^{Sc} is not resistant to PK (Safar et al. 1998). Safar and his team used a conformation-dependent immunoassay (CDI) to detect and quantify PrP^{Sc} in the presence of PrP^{C} without relying on PK-limited proteolysis. The CDI approach capitalizes on the increased reactivity of antibodies to PrP epitopes that are cryptic in PrP^{Sc} but become exposed after guanidine hydrochloride denaturation, whereas these epitopes are endogenously exposed in PrP^{C} without the requirement of denaturation (Safar et al. 1998). Furthermore, the researchers discovered that the application of PK to prion samples before the CDI assay significantly reduced the signal following guanidine hydrochloride denaturation, indicating the presence of a PK-sensitive fraction of PrP^{Sc} (Safar et al. 1998). Additional studies by Tzaban et al. suggested that the PK sensitivity of PrP^{Sc} may be affected by its quaternary structure, with smaller aggregates being less resistant (Tzaban et al. 2002). Pastrana et al. subsequently identified a PK-sensitive fraction of PrP^{Sc} which was found to be infectious (Pastrana et al. 2006, Sajnani et al. 2012),

although the precise determinants of its properties remain unclear. Notably, novel prion strains have been artificially created *in vitro* that are entirely protease-sensitive, indicating that protease resistance is not an essential prerequisite for prion infectivity (Legname et al. 2004, Colby et al. 2010).

1.4 PRION REPLICATION

The process by which PrP^{C} misfolds into PrP^{Sc} is not yet fully understood but it can be explained through two models: the templating model and the seeding model. According to the templating model (Prusiner et al. 1990, Cohen et al. 1994), the interaction between PrP^{C} and PrP^{Sc} lowers the energy barrier for the conversion from PrP^{C} to PrP^{Sc}, where PrP^{Sc} acts as a catalyst (Figure 1-2A). On the other hand, the seeding model (Come et al. 1993, Jarrett and Lansbury 1993) proposes that the conversion of PrP^{C} to PrP^{Sc} is a ubiquitous process that occurs at low levels but is inherently unstable and undetectable. Upon the formation of a sufficiently large PrP^{Sc} seed, it becomes stabilized and can recruit PrP^{C} at a faster rate upon amyloid fragmentation (Figure 1-2B).

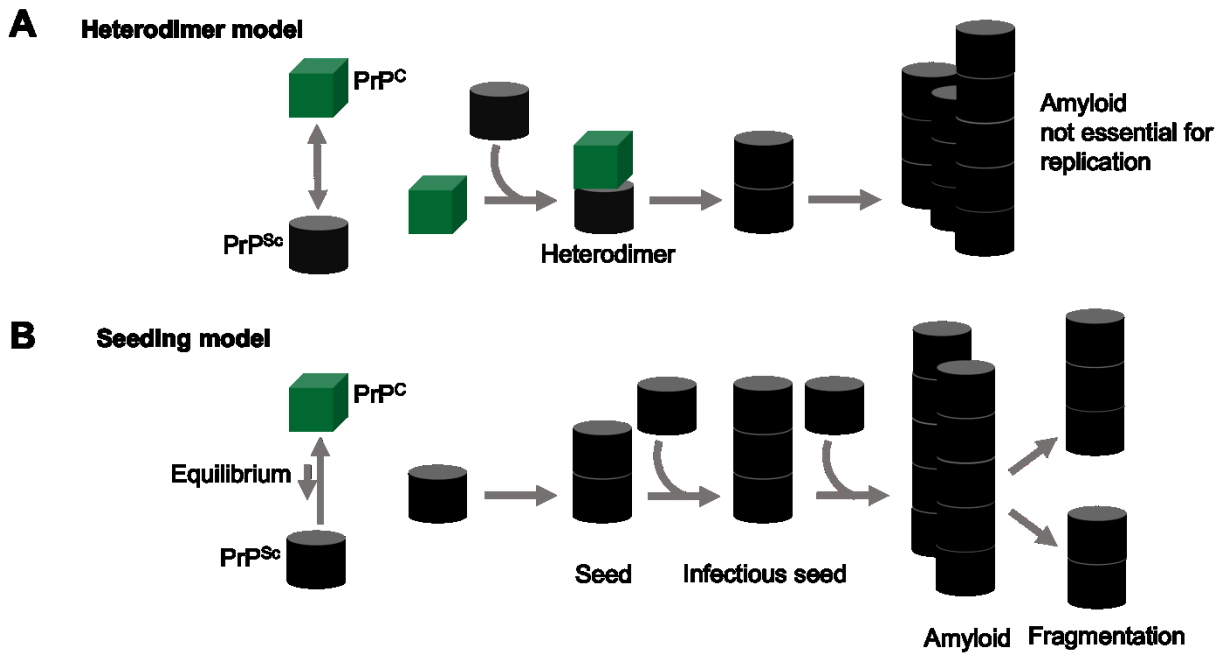

Figure 1-2. Prion conversion models. The two models used to explain prion conversion are the heterodimer (templating) and seeding models. (**A**) According to the heterodimer model, the spontaneous formation of PrP^{Sc} from PrP^{C} is hindered by an energy barrier, which can only be overcome by the presence of exogenous PrP^{Sc} as a catalyst. (**B**) In the seeding model, PrP^{C} and PrP^{Sc} are in equilibrium, with PrP^{Sc} slowly forming a seed that becomes an infectious seed capable of self-replication. The figure has been adapted from Aguzzi et al. (2001).

1.5 PRION STRAINS

In biology, strains can refer to genetic differences that are inheritable and lead to varying phenotypes within a subset of a population. Since prions do not have a nucleic acid component, their unique properties are believed to be encoded in their higher-order aggregate structures. While the host genome encodes PrP^{C}, prions themselves encode several phenotypic prion variants, referred to as prion strains

(Carta and Aguzzi 2022). Prion strains can be distinguished based on their unique biochemical properties, which include the glycoforms of PrP^{Sc}, the extent of PK resistance of PrP^{Sc}, its electrophoretic mobility, and its stability under denaturing conditions. The aforementioned properties can have an impact on various clinical features including the incubation period, clinical symptoms, and histopathological profile. It has been well demonstrated that differences in prion strains are linked to differences in the conformation of PrP^{Sc} (Bessen and Marsh 1992, Collinge et al. 1996, Telling et al. 1996, Safar et al. 1998, Manka et al. 2023).

1.6 THE SPECIES BARRIER

While prions can infect different mammalian species, transmission between individuals of the same species is much more efficient than transmission between different species. This phenomenon is called “the species barrier” or “transmission barrier” and is believed to be related to the differences in amino acid sequences and the conformational variations of different prion strains in various species (Gajdusek et al. 1965, Prusiner 1998). In terms of prion strains, it is believed that their properties play a crucial role in determining their ability to cross species barriers. For example, while variant CJD (section 1.7.3), a type of prion disease found in humans, can be transmitted to laboratory mice, the transmission of sporadic CJD (section 1.7.2), another type of human prion, to the same mouse line has proven to be very difficult (Gibbs and Gajdusek 1973). Studying the structure of PrP^{Sc} in various host species, such as humans, cattle, and cervids, can greatly assist in understanding the molecular mechanisms underlying the species barrier.

1.7 HUMAN PRION DISEASES

1.7.1 Kuru

Kuru is a prion disease originating in the Fore tribe in Papua New Guinea, propagated by ritualistic endocannibalism practices during funerary ceremonies. Kuru, which means "to shake", is characterized by involuntary tremors. The disease was successfully eradicated through the cessation of endocannibalism in the 1950s, with only one or two cases reported annually from 1996 to 2004 with the last known case reported in March 2005 (Collinge et al. 2006). Recent research suggests that the Fore population propagated a genetic variant, *PRNP* G127V, that protects against the development of kuru and prevents transmission with 100% efficiency in transgenic (Tg) mice expressing human G127V prion protein (Mead et al. 2009, Asante et al. 2015). The discovery of this genetic mutation is a remarkable example of rapid human evolution under selection pressure from a locally common disease.

1.7.2 Sporadic Creutzfeldt-Jakob disease

Creutzfeldt-Jakob disease was initially reported in the 1920s by Creutzfeldt and Jakob although not all their cases met the current diagnostic criteria for a human prion disease (Creutzfeldt 1920, Jakob 1921). The most common type of CJD is sporadic Creutzfeldt-Jakob disease (sCJD), accounting for approximately 84% of all human prion disease cases, with a rate of 1-1.5 cases per million people per year (Ladogana et al. 2005). The origin of sCJD is unknown, but it is believed to result

from the spontaneous development of PrP^{Sc}, which then spreads within the host. A typical variation of *PRNP*, the gene encoding prion protein in humans, plays a crucial role in CJD development. At codon 129 either a methionine or a valine can be encoded and individuals who are heterozygous at this position are protected when compared to homozygotes (Palmer et al. 1991).

1.7.3 Variant Creutzfeldt-Jakob disease

The United Kingdom first reported variant Creutzfeldt-Jakob disease (vCJD), a form of CJD which is believed to be linked to the consumption of BSE-infected cattle (cattle with prion disease) (Will et al. 1996). This hypothesis is further supported by the transmission and neuropathological studies conducted on rodent models which showed that the BSE and vCJD agents have similar transmission properties and brain lesion profiles (Bruce et al. 1997, Hill et al. 1997). On the other hand, vCJD differs from sCJD in terms of onset age, neuropathological patterns, and disease duration, with younger individuals being more likely to be affected. The majority of UK vCJD patients have the 129MM genotype, indicating a significant genetic risk factor (Collinge et al. 1991). An examination of archived appendix samples in a recent epidemiological study suggested that 1 in 2000 individuals in the UK might be silent carriers of vCJD infectivity (Gill et al. 2020). Most of the appendices that tested positive for PrP^{Sc} belonged to individuals expressing the 129V polymorphism. These findings suggest that the onset of vCJD might be slower in individuals carrying this *PRNP* allele, but there is a possibility of future cases.

1.7.4 Iatrogenic Creutzfeldt-Jakob disease

Iatrogenic Creutzfeldt-Jakob disease (iCJD) can occur due to inadequate decontamination during medical or surgical procedures, leading to the transfer of CJD prions between patients. Most iatrogenic Creutzfeldt-Jakob disease cases arise from the use of human products obtained from cadavers during medical procedures, accounting for less than 1% of all cases of CJD. This mode of transmission became evident when a corneal transplant recipient developed CJD 18 months after the surgery, and the donor was confirmed to have died of CJD (Duffy et al. 1974). Two more cases were reported in patients who received seemingly sterile electrodes that were previously implanted in a CJD patient. Sterilization procedures were not sufficient to decontaminate CJD infectivity, as demonstrated by spongiform encephalopathy resulting from implanting a suspected electrode in the cortex of a chimpanzee (Brown et al. 2012). Injection of human-derived growth hormones or use of dura mater grafts obtained from human cadavers has also caused iCJD (Brown et al. 2012). Some instances of prion disease have also been associated with blood transfusions received from subclinical CJD patients (Urwin et al. 2016). A recent case of iCJD was likely linked to laboratory exposure to BSE-infected transgenic mice expressing human prion protein (Brandel et al. 2020).

1.7.5 Genetic prion diseases in humans

Approximately 15% of human prion disease cases are caused by autosomal dominant mutations in *PRNP* that alter the structure of PrP^C, increasing the likelihood of misfolding and aggregation (Liemann and Glockshuber 1999). These mutations can involve single amino acid changes, premature stop codons, or sequence duplications. Inherited prion diseases are subdivided into three groups based on clinical presentation: Familial Creutzfeldt-Jakob disease (fCJD), fatal familial insomnia (FFI), and Gerstmann-Sträussler-Scheinker disease (GSS).

fCJD, which represents approximately 15% of all CJD cases worldwide, is characterized by rapidly progressive dementia and myoclonus (Masters et al. 1979). The substitution of glutamate (E) for lysine (K) at codon 200 (E200K) is the most common mutation causing fCJD. This mutation is found in various clusters worldwide, particularly in a community of Libyan Jews, accounting for approximately 38% of fCJD cases (Goldgaber et al. 1989, Goldfarb et al. 1990, Kovačs et al. 2005). Aspartic acid (D) to asparagine (N) mutation at codon 178 (D178N) is another common mutation that, when combined with polymorphism 129V (valine at codon 129), leads to fCJD.

FFI is a hereditary prion disease that was initially observed in an Italian family in 1986 and is characterized by a progressive and profound inability to sleep that results in hallucinations and eventual death (Lugaresi et al. 1986). The average survival time

after the onset of clinical symptoms is roughly 18 months (Gambetti et al. 1995). This disease is caused by a single known mutation, D178N, which is linked to the existence of the methionine polymorphism at codon 129 (Medori et al. 1992), whereas a valine at this position is linked to fCJD (Goldfarb et al. 1992).

GSS was first described by Gerstmann, Sträussler, and Scheinker in the early nineteen hundreds as a familial disease with autosomal dominant inheritance (Gerstmann et al. 1935). It is linked to *PRNP* mutations such as proline (P) to leucine (L) substitution at codon 102 (P102L), alanine (A) to valine (V) substitution at codon 117 (A117V), and phenylalanine (F) to serine (S) substitution at codon 198 (F198S). This disease manifests as a slowly progressive disease with ataxia and motor dysfunction (Hsiao et al. 1989).

1.8 ANIMAL PRION DISEASES

1.8.1 Scrapie

Scrapie, the oldest known prion disease, was first recorded 300 years ago in England (Brown and Bradley 1998). Its name comes from the behavior of infected sheep and goats scraping off their coats on objects. Sheep's susceptibility to classical scrapie is influenced by their *Prnp* gene's polymorphisms, exposure age, infectious dose, and route of infection. There are three sheep PrP polymorphisms that affect susceptibility to scrapie: alanine to valine substitution at codon 136 (A136V), histidine to arginine at codon 154 (H154R), and arginine to glutamine at codon 171 (R171Q) (Goldmann et

al. 1994, Westaway et al. 1994, Hunter et al. 1996). Scrapie is mainly transmitted through oral consumption of PrP^{Sc} by young sheep, including prenatal and periparturient transmission, nursing, and environmental exposure (Cassmann and Greenlee 2020). Infected sheep shed PrP^{Sc} through saliva, urine, and feces, which can lead to horizontal transmission (Cassmann and Greenlee 2020). Shedding during the subclinical stage of the disease is a concern for scrapie control. Atypical scrapie (Nor98) is a type of scrapie first identified in sheep in Norway in 1998 and later found in the United States, Australia, and New Zealand (Benestad et al. 2003). It affects single, older animals within a flock and is considered a spontaneous prion disease (Benestad et al. 2008). Atypical scrapie occurs in sheep with genotypes that are resistant to classical scrapie and differs from classical scrapie in terms of the distribution of brain lesions (Benestad et al. 2008, Moore et al. 2008). Research on the zoonotic potential of the scrapie agent indicates low risk as the prion phenotypes of human TSE patients and those from sheep with scrapie are not compatible (Greenlee and Greenlee 2015). However, transgenic mice overexpressing human PrP^{C} show susceptibility to some classical scrapie strains, indicating potential zoonotic risk (Cassard et al. 2014). Non-human primates are also susceptible but with a long incubation period (Comoy et al. 2015).

1.8.2 Bovine spongiform encephalopathy (BSE)

Bovine spongiform encephalopathy (BSE), commonly known as mad cow disease, serves as a prime example of the potential risks of prion diseases to animal and human health. The disease was first identified in the UK during the 1980s and was

linked to the feeding of meat-and-bone meals (MBM) to cattle, which is now prohibited (Wells et al. 1987, Brown et al. 2001). The ban led to a significant decrease in BSE cases, falling below surveillance levels. BSE is categorized as classical, represented by C-BSE, or atypical, including L-BSE and H-BSE, which share the same *Prnp* gene sequence but have different biochemical characteristics, age of disease onset, lesion profiles in the brain, and incubation periods (Biacabe et al. 2004, Casalone et al. 2004). The origin of BSE in the UK is unknown, and several hypotheses have been proposed, including feeding cattle with scrapie-infected sheep and the possibility that BSE started sporadically in cattle and was transmitted through MBM (Baron et al. 2007). The origin and characteristics of atypical BSE strains are also not well understood but it is hypothesized that they may have initially emerged sporadically in cattle (Biacabe et al. 2008). BSE is the only confirmed zoonotic prion disease affecting humans among all animal prion diseases, causing variant Creutzfeldt-Jakob disease.

1.8.3 Transmissible mink encephalopathy (TME)

Transmissible mink encephalopathy (TME) was first discovered in 1947 in ranch-raised mink in Brown County, Wisconsin, USA. The disease has a mortality rate of 100% in mink over one year of age and is caused by exposure to contaminated feedstuffs (Hartsough and Burger 1965). TME was officially identified and characterized in the 1960s (Marsh et al. 1969), with the last known outbreak occurring in 1985 (Marsh et al. 1991). The disease primarily affects mink over the age of one and has an incubation period of around six months. Symptoms include

behavioral changes and neurological disorders. TME has been transmitted to various hosts, including hamsters, and has resulted in the emergence of two distinct disease phenotypes/strains known as hyper and drowsy (Bessen and Marsh 1992). Despite having the same primary protein structure, these strains differ in their biochemical properties and symptoms. The hyper strain of the disease is identified by its brief incubation period, hyperaesthesia, and cerebellar ataxia, whereas the drowsy strain is distinguished by its prolonged incubation period and lethargy (Bessen and Marsh 1992).

1.8.4 Chronic wasting disease

Chronic wasting disease (CWD) is a highly contagious prion disease that affects various species of the Cervidae family and is the only known prion disease that affects both wild and farmed animals (Williams and Young 1980, Spraker et al. 1997). Its highly contagious nature, combined with its widespread presence and persistence in the environment, make controlling the disease in deer populations difficult.

The origin of CWD is still unknown. In North America, it was first identified in captive mule deer (*Odocoileus hemionus*) in Colorado in 1967 and was officially diagnosed as a transmissible spongiform encephalopathy in 1978 (Williams and Miller 2002, Williams 2005). Since then, the disease has spread to wild mule deer, white-tailed deer (*Odocoileus virginianus*), elk (*Cervus canadensis*), reindeer (*Rangifer tarandus*), and moose (*Alces alces*). Its geographic range has continued to expand, with CWD

now reported in four Canadian provinces, thirty American states, as well as South Korea, Norway, Finland, and Sweden. The emergence of CWD in Canada was first reported in 1996 when it was identified in farmed elk from Saskatchewan (Williams and Miller 2002). CWD likely entered Saskatchewan farms via captive elk imported from South Dakota (Williams and Miller 2002). The source of the outbreak in wild Canadian cervids remains unknown but contact between wild deer and infected farmed elk is a possible transmission route. Subsequently, CWD was detected in farmed white-tailed deer in Alberta and in wild cervid populations from Alberta, Saskatchewan, and Manitoba (Kahn et al. 2004). While CWD was detected in wild moose from Alberta in 2013 (Benestad and Telling 2018), it has not been reported in the wild North American subspecies of caribou (*Rangifer tarandus spp*) to date. The initial detection of chronic wasting disease in Europe occurred in 2016 when a free-ranging Norwegian reindeer (*Rangifer tarandus tarandus*) tested positive (Benestad et al. 2016). The origin of the outbreak is still unknown but the transmission of Norwegian CWD isolates into bank voles confirmed the presence of distinct strains that differ from those found in North America, indicating that these cases are not epidemiologically linked (Nonno et al. 2020). Additionally, the importation of cervids into Norway is prohibited, making it improbable that the infections were introduced by imported positive animals, as seen in the CWD cases in Korea. To date, more than 30 cervids in Norway have tested positive for CWD, including 20 reindeer, 11 moose, and two red deer (Tranulis et al. 2021). CWD is an unprecedented threat to cervids in North America, with millions at risk of infection due to the expanding geographic range and increasing disease prevalence. CWD prevalence in North America has

been increasing exponentially for years, reaching over 80% in farmed herds and over 45% in wild populations (Keane et al. 2008, Otero et al. 2021). In Alberta, mule deer males are most affected, followed by mule deer females, white-tailed males, and white-tailed females (Otero et al. 2021). The burden of CWD in wild elk in Alberta is not as extensive as in deer.

Deer and elk with CWD exhibit weight loss, behavioral changes, and excessive salivation. These symptoms progress gradually, resulting in emaciation and a lack of fear towards humans (Williams 2003). In North America, CWD is characterized by extensive deposition of PrP^{Sc} in the central nervous system and lymphoid tissues, with detectable levels of PrP^{Sc} in the latter at an early stage (Sigurdson et al. 1999, Fox et al. 2006). PrP^{Sc} or infectivity has also been detected in other tissues and bodily fluids including skeletal muscle (Angers et al. 2006), pancreas (Sigurdson et al. 2001), adrenal gland (Sigurdson et al. 2001), cardiac muscle (Jewell et al. 2006), saliva (Mathiason et al. 2006), blood (Mathiason et al. 2006), urine, and fecal material from subclinical deer (Haley et al. 2009). CWD prions have even been detected in fetal tissue from white-tail deer (Bravo-Risi et al. 2021, Nalls et al. 2021).

1.8.4.1 *Prnp* polymorphisms in cervids

Although the *Prnp* coding sequence is highly conserved among cervid species, many key polymorphisms have been identified that can significantly influence the susceptibility to CWD in deer and elk (Figure 1-3) (Arifin et al. 2021).

Early genetic analyses showed a variation at codon 132 in North American elk PrP, which encodes either methionine (M) or leucine (L) (Schätzl et al. 1997). 132M is the more common allele. This variation is equivalent to codon 129 in the human *PRNP*, which influences susceptibility to prion diseases. Experimental studies suggest that elk with at least one L allele have reduced susceptibility to CWD, with 132LL elk being the most resistant (O'Rourke et al. 1999, O'Rourke et al. 2007). However, they are still susceptible with longer incubation periods than 132ML and 132MM elk.

The susceptibility of mule deer to CWD is influenced by a polymorphism at codon 225 that codes for either serine (S) or phenylalanine (F) (Brayton et al. 2004). The presence of the 225F allele reduces susceptibility to CWD. Homozygous deer with the 225SS genotype was found to be 30 times more likely to develop CWD than heterozygous deer with the 225SF genotype (Jewell et al. 2005). In CWD-negative deer, the frequency of the 225SF and 225FF genotypes was 9.3% while, in CWD-positive deer, it was only 0.3% according to a study by Jewell et al. in 2005 (Jewell et al. 2005).

Polymorphisms in white-tailed deer have been reported at codons 95, 96, 116, and 226, encoding glutamine (Q) or histidine (H), glycine (G) or serine (S), alanine (A) or glycine (G), and glutamine (Q) or lysine (K), respectively (Raymond et al. 2000, Heaton et al. 2003, Johnson et al. 2003, O'Rourke et al. 2004).

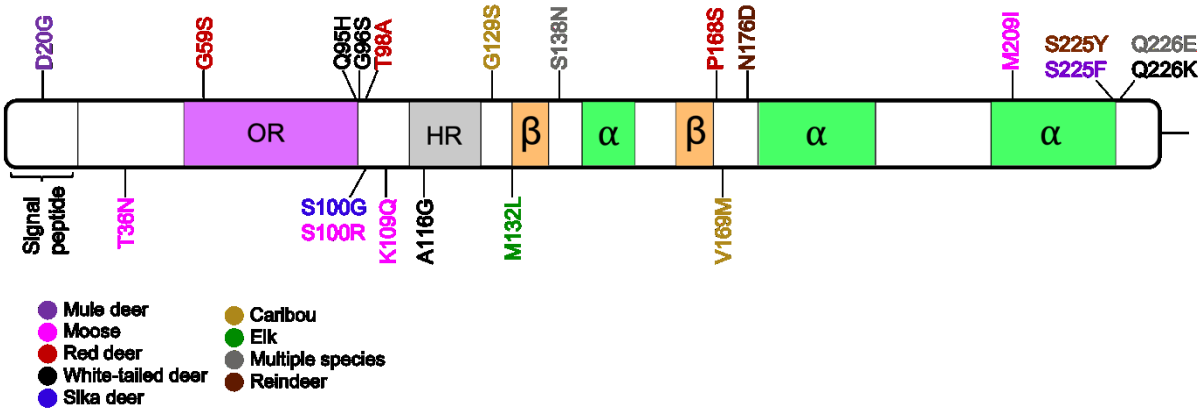

Figure 1-3. Cervid polymorphisms. Each color represents a cervid species. Grey stands for multiple species since S138N exists in white-tailed deer, mule deer, caribou, and fallow deer. Q226E has been described in red deer, sika deer, elk, and fallow deer. All numbering is cervid numbering. The figure has been adapted from Otero et al. (2023).

Deer with the 96S allele and infected with CWD had slower disease progression compared to those with the 96G allele (Johnson et al. 2006). The 95H allele is rare in the wild population (1–2%) but deer carrying it are affected by CWD at a lower rate relative to its allelic frequency indicating that it may confer some protection against the disease (O'Rourke et al. 2004, Johnson et al. 2006, Haley et al. 2019). An experimental study was conducted where deer with different *Prnp* alleles, wild type (WT) (95Q/96G), 96S/ WT (96S/95Q), 95H/ WT (95H/96G), or 95H/96S, were orally inoculated with PrP^{Sc} from wild type deer (Otero et al. 2019). While all the inoculated WTD eventually developed clinical CWD, those carrying the 96S/ WT genotype survived approximately 9 months longer compared to the wild type animals. The WTD

carrying the 95H allele had the longest survival of up to 2.5 years post-infection (Otero et al. 2019). The A116G polymorphism in WTD is rare in the wild population and its effect on CWD susceptibility is uncertain - some studies show no effect (O'Rourke et al. 2004) while others suggest it may reduce susceptibility (Hannaoui et al. 2017). However, this polymorphism is significant because it is located in the central hydrophobic region of PrP, which is essential for prion conversion (Wang et al. 2010).

Studies have shown that North American moose (*Alces alces spp*) exhibit polymorphisms at position 36 (threonine or asparagine), position 100 (serine or arginine), and position 209 (methionine or isoleucine) in its PrP sequence (Huson and Happ 2006, Wik et al. 2012). The PrP sequence of European moose (*A. a. alces*) is similar to that of North American moose, except for a difference at position 109 (lysine to glutamine) (Wik et al. 2012). All identified cases of CWD in moose have been observed in those with the wild type PrP sequence (Pirisinu et al. 2018).

1.8.4.2 CWD strains

CWD1 and CWD2 were the first CWD strains identified based on clinical and histological characteristics in Tg1536+/- cervidized mice that overexpresses deer PrP (Angers et al. 2010). Elk and deer CWD isolates were tested on these mice, resulting in different incubation periods and distinct neuropathologies. CWD1 had a short incubation period, high levels of vacuolation, and widespread PrP^{Sc} deposition,

whereas CWD2 had a longer incubation period, low vacuolation, and asymmetrical distribution of PrP^{Sc}. Despite these differences, both strains had similar glycosylation patterns and denaturation profiles. The researchers concluded that deer brains usually contain a mixture of CWD1/CWD2, whereas elk are generally infected with only one strain.

Deer expressing different *Prnp* polymorphisms (Q95/G96 (WT / WT), S96/ WT, H95/ WT or H95/S96) were experimentally infected with CWD, and the results showed that these polymorphisms affect the incubation period (Johnson et al. 2011). Homozygous wild type deer had a shorter incubation period, while heterozygous deer had longer incubation periods, indicating partial resistance to the disease. Passaging of these deer isolates in transgenic mouse lines (Tg33 (WT) and Tg60 (S96)) provided further understanding of these agents (Duque Velasquez et al. 2015, Duque Velasquez et al. 2020). In Tg33 mice, regardless of the CWD lineage received, neuropathological profiles and PrP^{Sc} type were similar and highly resembled WT / WT deer CWD prions, indicating adaptation of a common strain to all lineages (called Wisc-1). When transgenic mice expressing S96-PrP^{C} were used, a unique strain named H95+ emerged. The H95+ strain of CWD, unlike the Wisc-1 strain found in wild type deer, is capable of causing prion disease in Tg60 mice, which were previously thought to be resistant to CWD. Wisc-1 and H95+ have distinct biochemical and neuropathological characteristics, as well as different host ranges in wild type rodents (Duque Velasquez et al. 2015, Duque Velasquez et al. 2020).

In a study by Hannaoui et al. it was found that deer with the A116G *Prnp* polymorphism were able to replicate a new strain of CWD (Hannaoui et al. 2017, Hannaoui et al. 2021). The researchers compared the Wisc-1 CWD strain from wild type deer with prions obtained from a hunter-harvested, A116G heterozygous deer. The amino acid substitution of G116 in the hydrophobic core region of PrP^{C} led to lower conformational stability in guanidine hydrochloride, reduced resistance to proteases, and decreased RT-QuIC seeding activity compared to the Wisc-1 strain. RT-QuIC (real-time quaking-induced conversion assay) is a highly sensitive cell-free technique used for amplifying prions. The differences between the two strains were maintained after passage in transgenic mice, indicating that the G116 deer contained a distinct CWD strain (Hannaoui et al. 2017, Hannaoui et al. 2021).

Elk *Prnp* exhibits variability at amino acid 132, where methionine and leucine can occur. In an experimental study, elk expressing the three different 132 *Prnp* genotypes displayed varying degrees of CWD progression, with MM132 elk being the first to succumb, followed by ML132 elk, and finally, LL132 elk. LL132 elk exhibited different patterns of CWD lesions in their brains, as well as distinct protease-resistant PrP^{Sc} patterns, fibril stability, abundance in the brain, and RT-QuIC seeding activity compared to MM132 and ML132 elk prions (O'Rourke et al. 2007, Moore et al. 2018). Strain typing of these isolates in transgenic mice expressing MM132 elk PrP^{C} leads to prolonged incubation periods for LL132 isolates and the PrP^{Sc} produced in the mice

shows reduced accumulation in the brain and lower molecular weight than the PrP^{Sc} detected in mice inoculated with MM132 or ML132 brain homogenates. However, no significant differences in disease phenotype were observed between mice inoculated with MM132 or ML132 CWD. The experimentally infected elk's phenotypic characteristics persisted after two passages of LL132, MM132, and ML132 isolates into mice expressing MM132 PrP^{C}. Therefore, the CWD prions that developed in LL132 elk represent a new CWD strain (Moore et al. 2020).

In 2016, the detection of CWD in European cervids raised concerns regarding its origin (Benestad et al. 2016). To investigate if European and North American CWD cases were related, scientists conducted a study where they infected bank voles (a model efficiently infected with the widest range of prions) with various CWD isolates (Nonno et al. 2020). Surprisingly, the CWD prions in Europe were found to be distinct from those in North America and at least four different CWD strains were identified, including one found in all Canadian CWD cases, one in Norwegian reindeer CWD (R-NO1), and two distinct strains in Norwegian moose (M-NO1 and M-NO2) (Nonno et al. 2020). The strain typing of European CWD isolates is still ongoing.

1.8.4.3 Transmission of CWD

CWD is a prion disease that is highly efficient in its transmission in the wild, and its contagious nature is unparalleled when compared to other prion diseases (Miller et al. 2000, Miller and Williams 2003). The disease has been observed to be remarkably

contagious in captive mule deer populations, with 90% of the population developing the disease over two years (Williams and Young 1980). Although the exact natural route of CWD transmission is not known, it is believed to be mainly transmitted laterally through the ingestion of contaminated forage or water, which may be contaminated with CWD-infected carcasses, saliva, blood, urine, and feces (Williams and Miller 2002, Miller and Williams 2004, Mathiason et al. 2006, Haley et al. 2009, Tamgüney et al. 2009). Vertical transmission from mother to offspring has also been observed in Muntjac deer (Nalls et al. 2021). Elk antler velvet may also play a role in CWD transmission since bioassays have detected that it contains CWD prions and it is shed annually (Angers et al. 2009). Prions can associate with soil microparticles, increasing their transmissibility (Johnson et al. 2007, Kuznetsova et al. 2014, Kuznetsova et al. 2020). Plants, including grass, can also serve as reservoirs for CWD contamination and transmission, with contaminated pastures remaining infectious for at least two years (Miller et al. 2004).

Understanding the various strains of chronic wasting disease and how they may transmit between species is important, particularly considering the potential for human exposure. The emergence of variant Creutzfeldt-Jakob disease after exposure to bovine spongiform encephalopathy has raised concerns about the human species barrier to other animal prion diseases, including CWD (Otero et al. 2021, Hannaoui et al. 2022, Pritzkow 2022). CWD has been detected in the skeletal muscle and fat of infected animals, which raises concerns about the possibility of humans consuming CWD prions through the consumption of contaminated meat or antler velvet, which is

used in traditional Asian medicine (Angers et al. 2006, Angers et al. 2009). The zoonotic potential of CWD is still not fully understood. Current surveillance has not detected any evidence of CWD transmission to humans. However, extensive *in-vitro* and *in-vivo* models have been developed to investigate the transmission barrier of CWD to humans. *In vitro* studies have indicated the presence of a strong barrier, although two studies have shown efficient conversion of human prion protein by CWD prions *in vitro* (Barria et al. 2011, Wang et al. 2021). *In vivo* studies have utilized non-human primate models and transgenic mice to evaluate the species barrier of CWD. Regarding CWD transmission to non-human primates, squirrel monkeys have exhibited susceptibility to CWD, while cynomolgus macaques have not (Race et al. 2009, Race et al. 2014, Race et al. 2018). Transgenic mice expressing human prion protein have been instrumental in studying prion disease transmission. To date, eight different research groups have examined the susceptibility of humanized mice to CWD infection. Seven of these groups have reported no substantial evidence of CWD transmission to these humanized mice (Kong et al. 2005, Sandberg et al. 2010, Wilson et al. 2012, Kurt et al. 2015, Race et al. 2019, Wadsworth et al. 2022) (Tamgüney et al. 2006). However, a recent study by Hannaoui et al. revealed atypical disease manifestations and prion shedding in the feces of transgenic mice expressing human prion protein when infected with deer prions, suggesting the potential for zoonotic transmission of CWD (Hannaoui et al. 2022). Overall, these findings underscore the need for further investigation to enhance our understanding of the zoonotic potential of CWD.

1.9 THE STRUCTURE OF PrP^{Sc}

Recent advancements in experimental techniques have provided researchers with powerful tools to analyze the atomic-level structures and dynamics of proteins. Among these techniques, X-ray crystallography and solution-state nuclear magnetic resonance spectroscopy have played a significant role in determining the native structures of globular proteins, including cellular prion protein (section 1.2).

Unlike native globular folds, products of misfolding have been difficult to study by classic structural biology methods. The insolubility of amyloid fibrils and the scarcity of well-ordered three-dimensional (3D) crystalline forms have hindered high-resolution imaging of fibrils until recent years when the advent of solid-state nuclear magnetic resonance spectroscopy (ssNMR) and cryo electron microscopy has made structural analyses of amyloid prion fibrils with near-atomic resolution possible (Eisenberg and Sawaya 2017, Flores-Fernández et al. 2018, Kraus et al. 2021, Hallinan et al. 2022, Hoyt et al. 2022, Hoyt et al. 2022, Manka et al. 2022, Manka et al. 2023).

Over the years researchers have combined multiple complementary techniques to investigate the structure of PrP^{Sc}. Below some of these techniques are briefly introduced.

Fourier-transform infrared (FTIR) spectroscopy and circular dichroism (CD) spectroscopy commonly used to determine the secondary structure of proteins, have demonstrated a substantial β-sheet content in PrP^{Sc} and PrP 27–30 (Safar et al. 1993) (Caughey et al. 1991, Pan et al. 1993). Initially, the FTIR data suggested the retention of some α-helical structure from the original PrP^{C} fold in PrP^{Sc} and PrP 27–30. However, more recent investigations have revealed that the ~1660 cm^{-1} band observed in the FTIR spectra, previously associated with α-helical conformation, is also present in the spectrum of recombinant PrP amyloid fibrils (Smirnovas et al. 2011). These fibrils are known to have a parallel in-register β-structure and completely lack α-helical elements (Cobb et al. 2007). Therefore, the ~1660 cm^{-1} FTIR band has been redefined as indicative of turns and coils (Smirnovas et al. 2011). Currently, it is widely acknowledged that the structural conformation of the PrP^{Sc} does not contain α-helices and is predominantly composed of β-strands.

Two additional techniques, limited proteolysis, and hydrogen/deuterium (H/D) exchange played a crucial role in providing valuable insights into the structure of PrP^{Sc}. These techniques focus on different aspects of the solvent accessibility of the prion protein. Limited proteolysis is based on the principle that proteases, under limiting conditions, preferentially cleave protein regions exhibiting accessible and flexible secondary structures, such as α-helices and loops, while sparing β-strands (Hubbard 1998). On the other hand, H/D exchange relies on the observation that unstructured protein regions in solution undergo a rapid exchange of hydrogen for

deuterium ions at backbone amides, compared to the relatively slower exchange in α-helices and β-sheets (Smirnovas et al. 2011).

Through limited proteolysis using PK, early studies demonstrated the strong resistance of PrP^{Sc} fibrils to proteolytic cleavage, except for the N-terminal residues (~23–90), which were found to be particularly labile (Sajnani et al. 2008). It is noteworthy that PrP^{Sc} fibrils, even after N-terminal digestion by PK treatment, retained their full infectivity.

More recently, these techniques were applied to generate a comprehensive PK-sensitivity map of anchorless PrP^{Sc}, allowing the identification of the approximate locations of β-strands and loops (Vázquez-Fernández et al. 2017). The analysis also highlighted the C-terminal half, as the most resistant part of PrP^{Sc}. Subsequent H/D exchange analyses supported these findings by showing relatively low exchange rates in a significant portion of the PrP^{Sc} C-terminus, specifically residues ~90 to 224, which is consistent with regions rich in β-strands (Smirnovas et al. 2011). Collectively, the data further substantiate the notion that the structure of PrP^{Sc} primarily consists of β-strands interconnected by short loops and/or turns, without the presence of α-helices.

Despite low-resolution techniques offering fundamental constraints that significantly contribute to our present understanding of the structure of PrP^{Sc}, they have been unable to provide the essential level of detail. Therefore, the application of high-resolution techniques to unravel the structure of PrP^{Sc} became imperative.

For decades, X-ray (XRD) crystallography has been extensively utilized to determine the atomic structures of proteins (Dill and MacCallum 2012, Shi 2014). It has been particularly successful in identifying high-resolution tertiary structures of globular amyloidogenic proteins like PrP (Riesner 2003, Moore et al. 2009). However, when applied to amyloid fibrils, crystalline material could only be obtained for small peptides, resulting in well-ordered nano- or micro-crystals (Balbirnie et al. 2001, Sawaya et al. 2007, Eisenberg and Sawaya 2017). More than 100 high-resolution amyloidogenic structures have been obtained from XRD of such samples (Eisenberg and Sawaya 2017). These structures often feature a motif called steric zipper, characterized by tightly packed b-sheets stabilized by hydrogen bonds (Riek and Eisenberg 2016, Eisenberg and Sawaya 2017). While these findings have significantly contributed to our understanding of amyloid stability's structural origins, it's important to note that the crystalized fragments are short, and their direct relevance to actual full-length misfolded species is not guaranteed. Due to these constraints, scientists have turned to X-ray fibre diffraction analyses, employing the amyloid fibrils themselves to generate XRD patterns (Eisenberg and Sawaya 2017, Flores-Fernández et al. 2018). These patterns exhibit prominent meridional signals representing a distance of 4.7-4.8 Å, which is interpreted as the spacing between β-

strands arranged perpendicular to the fibre axis (Sunde et al. 1997, Wille et al. 2009, Fitzpatrick et al. 2013, Wan et al. 2015). This particular structural arrangement, known as the cross-β structure, has been consistently observed in all identified amyloid fibrils (Iadanza et al. 2018). However, the fibre diffraction analyses are limited by the availability of well-aligned fibril specimens.

Solution NMR is another technique employed for the examination of the native fold of globular proteins. Acquisition and processing of NMR data are more straightforward when the molecules are in solution (Ziarek et al. 2018). However, solid-state NMR techniques are also available (Habenstein and Loquet 2016) making it possible to characterize the insoluble amyloid fibrils to near-atomic resolution (Eisenberg and Sawaya 2017, Loquet et al. 2018). The successful analysis of PrP^{Sc} using NMR spectroscopy relies on the availability of infectious recombinant PrP^{Sc}, as it requires high titer, ^{13}C- and ^{15}N-labeled samples. Researchers have employed solid-state NMR to investigate PrP amyloid fibrils. However, the amyloid samples exhibited only a moderate level of infectivity (Cobb et al. 2007, Tycko et al. 2010, Müller et al. 2014). NMR-based investigations demand considerable amounts of structurally homogenous samples, and this poses a significant challenge for all structural biology approaches, particularly given the ability of PrP to adopt various infectious conformations.

Electron microscopy (EM) is another powerful structural technique with a rich history of biological applications (Orlova and Saibil 2011). It holds the promise of achieving

sub-nanometric resolution, enabling 3D image reconstruction, and accommodating small sample sizes. However, it has faced challenges, such as the need to operate in a vacuum chamber, potential damage to biological samples, and low imaging contrast. To overcome these challenges, the widely used technique of negative staining EM comes into play. This method involves embedding biological samples in a thin layer of solid material containing a heavy metal salt (De Carlo and Harris 2011). By doing so, the image contrast is dramatically enhanced, making it a valuable approach for improving EM imaging quality. Negative stain electron microscopy was the method that enabled the initial visualization of infectious prions, which appeared as "prion rods," with widths ranging from 10 to 20 nm (Prusiner et al. 1983). Prior to this, earlier reports described "abnormal fibrillar structures" known as "scrapie-associated fibrils" or "SAFs" in the brains of scrapie-affected mice and hamsters (Merz et al. 1981). Negative stain electron microscopy is a frequently employed method for determining the fibril diameters of amyloid. The average protofilament diameters may vary depending on factors such as the prion strain, host species, the presence or absence of the GPI anchor, and other experimental conditions (Sim and Caughey 2009, Wille et al. 2009). For example, a study utilizing electron microscopy to investigate GPI anchorless prion fibrils derived from mouse-adapted scrapie strains (RML, ME7, and 22L) revealed that these strains exhibit similar fibrillar morphology but display variations in their periodicity and fibril diameter. The examination of fibrils using negative stain electron microscopy indicated a reported width of 4-6 nm (Sim and Caughey 2009). Moreover, the identification of two-dimensional (2D) crystals composed of PrP 27–30 enabled the application of multi-step image processing

techniques to extract low-resolution structural information concerning this conformation (Wille et al. 2002, Wille et al. 2007). This information was then utilized to constrain molecular models for the structure of PrP^{Sc} and to propose the concept of a parallel β-helix or β-solenoid (Wille et al. 2002, Govaerts et al. 2004). However, the application of negative stain electron microscopy limited the extent of structural data that could be acquired from these 2D crystals.

A pivotal invention has been freezing of biological samples to cryogenic temperatures in a thin layer of non-crystalline ice (vitreous ice) to protect their structural integrity against degradation during EM exposures (Taylor and Glaeser 1976, Dubochet et al. 1982, Adrian et al. 1984). This gave rise to cryo EM, a method described as a revolution in structural biology in recent years (Callaway 2015, Shen 2018). As the contrast of cryo EM imaging is typically low, it took nearly three decades after its invention until the progress of direct electron detectors in tandem with advanced image processing procedures allowed achieving an unprecedented structural resolution. Combining cryo EM images from amyloidal fibrils with a regular helical twist allowed generating 3D reconstructions with atomic detail as has been reported recently for a few prion strains (Kraus et al. 2021, Hallinan et al. 2022, Hoyt et al. 2022, Hoyt et al. 2022, Manka et al. 2022, Manka et al. 2023) (described in section 1.9.2).

In conclusion, by employing a combination of techniques, researchers have put forth two models for PrP^{Sc}: a 4-rung beta solenoid (4RβS) model (Figure 1-4A) described in section 1.9.1 (Wille et al. 2002, Wille et al. 2009, Vázquez-Fernández et al. 2016, Spagnolli et al. 2019, Kamali-Jamil et al. 2021) and the parallel in-register intermolecular β-sheet (PIRIBS) architectures (Figure 1-4B) described in section 1.9.2 (Kraus et al. 2021, Hallinan et al. 2022, Hoyt et al. 2022, Hoyt et al. 2022, Manka et al. 2022, Manka et al. 2023).

It is possible that various structures may exist for different prion diseases or even within a single disease, giving rise to different prion strains. Furthermore, the quaternary fibrillar structure of PrP^{Sc} is also still not fully understood, as recent studies have shown both one- and two-protofilament fibrils (Kamali-Jamil et al. 2021, Manka et al. 2023).

Indeed, the recent advancements in the structural study of infectious prions offer a promising opportunity to establish a comprehensive encyclopedia of the structure of various prion strains. Such a resource could pave the way for structure-based drug design and a deeper understanding of strain and species barriers.

In addition to the significance of unravelling the structure of infectious prion fibrils, studying the oligomers that emerge during the early stages of misfolding is equally

crucial, as they have been found to possess infectious properties. A study conducted by Silveira et al. demonstrated that aggregates beyond a certain size threshold of approximately 5 units exhibit infectivity, with oligomers containing about 14 to 28 units being the most infectious among the aggregates. However, investigating oligomers presents considerable complexities. They constitute a heterogeneous ensemble of short-lived species and are often present in low quantities. Achieving high-resolution characterization would necessitate selectively enriching and stabilizing each oligomeric species. Furthermore, the misfolding mechanism represents another crucial phenomenon that requires thorough investigation and comprehension. Studying the misfolding event itself presents significant challenges with many experimental approaches, as the timescale and resolution of these events often fall outside the easily observable parameter space. Molecular dynamics simulations can fill this gap by their intrinsic, molecular perspective and the step-by-step iterative process that forms the basis of the simulations (described in section 1.12).

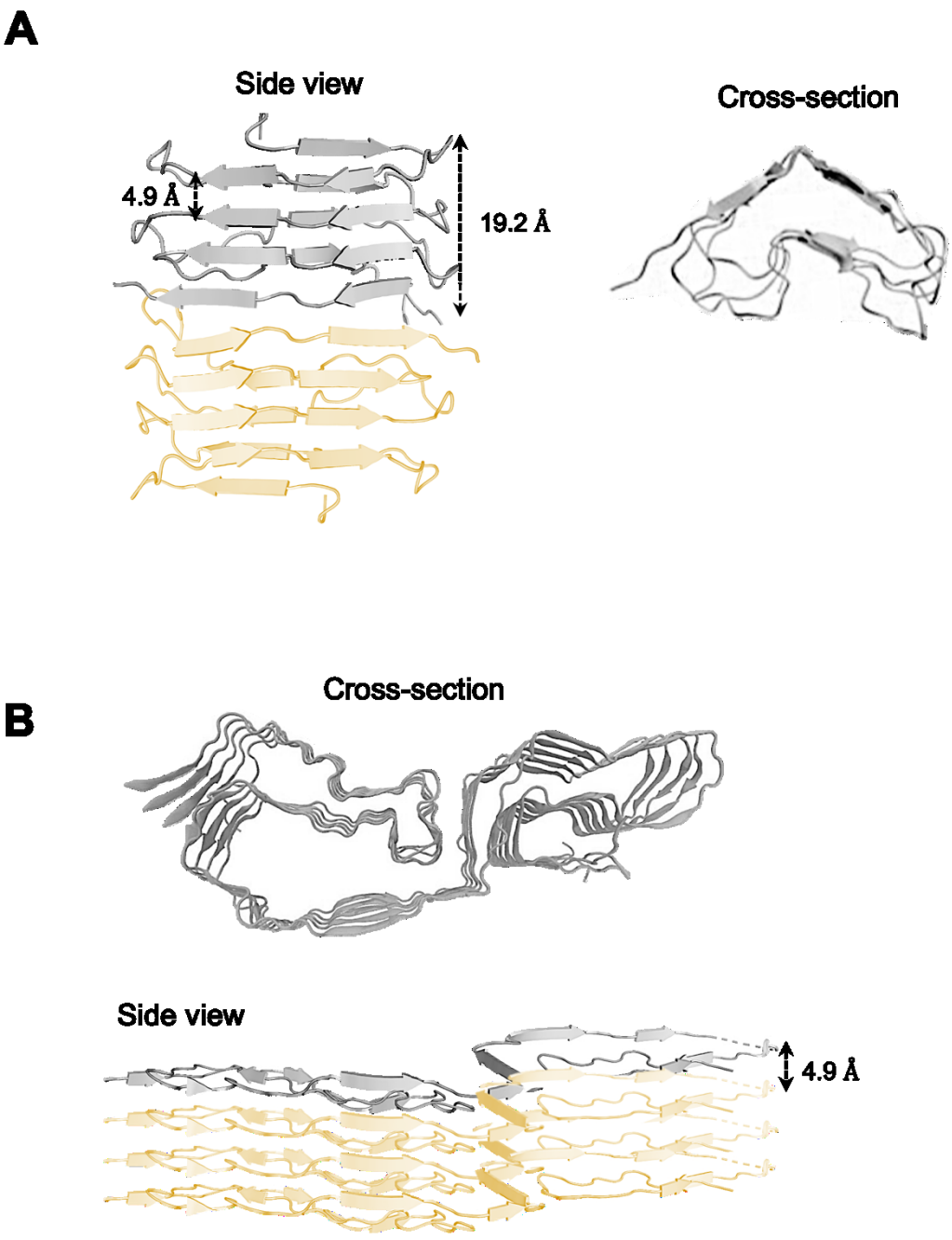

Figure 1-4. 4RβS model and PRIBS structure of PrP^{Sc}. (**A**) 4RβS model adapted from Spagnolli et al. (2019) for the anchorless RML prions. In the 4RβS model, the height of each monomer is 19.2 Å. (**B**) PIRIBS structure adapted from Kraus et al. (2021) for the N-terminally truncated 263K prions (PDB: 7lna). In the PIRIBS structure, the height of each monomer is 4.9 Å.

1.9.1 Four-rung beta solenoid model (4RβS)

Through electron crystallography on 2D crystals of PrP27-30 and a variant of only 106 residues, $PrP^{Sc}106$, it was determined that the β-solenoid fold was a crucial feature of the infectious conformer (Wille et al. 2002, Govaerts et al. 2004). However, X-ray fibre diffraction provided the first biophysical evidence that each monomer of PrP^{Sc} is arranged as a β-solenoid, demonstrating that the height of each PrP^{Sc} monomer was represented by a repeating unit of 19.2 Å, corresponding to the height of 4 β-strands (4 x 4.8 Å) (Wille et al. 2009). The absence of the 10 Å equatorial signal that characterizes stacked beta-sheet amyloid structure led to the suggestion of a beta-solenoid model for the architecture of PrP 27-30 molecules. Cryo-low dose electron micrographs of brain-derived GPI anchorless RML prion fibrils were used to generate 3D reconstructions, which revealed important details about the molecular architecture of the protein subunits (Vázquez-Fernández et al. 2016). Signals at 4.8 Å, which corresponded to the cross-β signals seen with X-ray fibre diffraction, were regularly detected by Fourier-transform analyses of unprocessed images from individual PrP^{Sc} amyloid fibrils. The 3D reconstructions of isolated PrP^{Sc} amyloid fibrils could resolve two intertwined protofilaments and provided enough detail to calculate the height of individual PrP^{Sc} molecules, which was approximately 18 Å, consistent with the repeating unit size of 19.2 Å determined by X-ray fibre diffraction. In addition, molecular dynamics simulation was utilized to construct an atomistic model of PrP^{Sc} based on available experimental data (Spagnolli et al. 2019). The model was found to be compatible with the four-rung β-solenoid arrangement. In

addition, a recent low-resolution negative stain-EM of brain-derived PrP27-30 of BSE-L type fibril also supports the four-rung β-solenoid model (Kamali-Jamil et al. 2021).

1.9.2 Parallel in-register intermolecular beta-sheet structure (PIRIBS)

The proposal of the Parallel In-Register Intermolecular Beta-Sheet model was grounded in the solid-state NMR data obtained from recombinant PrP amyloid fibrils, which were formed spontaneously or through prion-seeding (Cobb et al. 2007, Tycko et al. 2010, Theint et al. 2018, Shannon et al. 2019). Although synthetic fibrils are expected to have either no infectivity or significantly reduced infectivity rates, the proposed structures align with the recently resolved high-resolution cryo EM structure of the infectious *ex-vivo* 263K (Syrian hamster scrapie) strain, which revealed a PIRIBS structure (Kraus et al. 2021). Moreover, high-resolution cryo EM structures of both GPI-deficient (anchorless) and WT forms of various rodent-adapted scrapie prion strains, including RML, ME7, and 22L, also exhibited PIRIBS structures (Hoyt et al. 2022, Hoyt et al. 2022, Manka et al. 2022, Manka et al. 2023). In addition, cryo EM was employed to determine the structures of infectious prion proteins in humans (Hallinan et al. 2022). These filaments were obtained post-mortem from the brains of two patients suffering from Gerstmann-Sträussler-Scheinker disease and carrying the phenylalanine to serine mutation at codon 198. The outcomes indicated that the GSS (F198S) fibrils also exhibit a PIRIBS conformation.

1.10 THE N-TERMINAL REGION OF PRION PROTEIN

Despite the abundance of information on the structure of the cellular prion protein (section 1.2), the focus of research on the infectious prions is limited to the protease-resistant core region (section 1.9). The N-terminal region of infectious prions remains poorly understood due to its inherent flexibility, with even full-length prion studies failing to provide structural details on this region. On the other hand, numerous pieces of evidence highlight the role of the N-terminal region in the function of the prion protein and prion diseases, highlighting the knowledge gap in this regard and the need for further research on the structure of the N-terminal region of PrP in its infectious form.

As shown in Figure 1-1A, The N-terminal domain includes several characteristic regions, including two charged clusters, CC1 and CC2, which are rich in positively charged residues, an octapeptide repeat region, and a hydrophobic region. The following two sections provide a concise description of some of the findings that describe how these regions are associated with the normal function of PrP^{C} and prion disease.

1.10.1 The function and role of the N-terminal domain of PrP^{C}

Studies have demonstrated that mice lacking the *Prnp* gene (*Prnp*$^{0/0}$) are highly vulnerable to infection with influenza A viruses, experiencing more severe symptoms and higher levels of inflammation, apoptotic cell death, and oxidative stress in their lungs (Chida et al. 2018). Administration of a scavenger for reactive oxygen species

improved survival rates in *Prnp*$^{0/0}$ mice infected with influenza A viruses (Chida et al. 2018). Notably, PrP molecules lacking the octapeptide repeat region were ineffective at protecting *Prnp*$^{0/0}$ mice from lethal influenza A virus infection (Mitteregger et al. 2007, Chida et al. 2018). This suggests that PrP^{C}, mediated by the OR region which binds copper, may have a protective role against oxidative stress. The OR region-bound copper (section 1.11) may function as a transporter to copper/zinc-dependent superoxide dismutase, thereby regulating enzyme activity and ultimately providing this protection against oxidative stress. While some studies have suggested that PrP^{C} may have superoxide dismutase-like activity (Brown et al. 1999), contrasting findings have been reported by other research (Jones et al. 2005). The OR region is also suggested to be involved in other cell-protective mechanisms of PrP^{C}. Evidence suggests that overexpression of PrP^{C}, but not an OR-deficient PrP molecule, confers protection against apoptosis, suggesting that PrP^{C} could function as an anti-apoptotic molecule through the OR region (Bounhar et al. 2001). Also, studies reported that autophagy was activated in *Prnp*$^{0/0}$ cultured cells under serum deprivation and that expression of PrP^{C} prevented the activation of autophagy in the cells, but an OR-deleted PrP mutant did not, suggesting that PrP^{C} might manage autophagy activity in neuronal cells through the OR region (Oh et al. 2008). The charged cluster region is also suggested to be involved in the anti-oxidative activity of PrP^{C} (Haigh et al. 2009). Other roles have also been reported for this region, such as its involvement in facilitating the interaction of PrP^{C} with tubulin (Osiecka et al. 2009) or glycosaminoglycan (Pan et al. 2002), mediating the cleavage of the Alzheimer's

amyloid precursor protein through ß-secretase (Parkin et al. 2007, Bravard et al. 2015), and DNA repair.

1.10.2 The N-terminal domain and prion diseases

Transgenic mice expressing truncated variants of PrP^{C} devoid of either residues 32-93 (Flechsig et al. 2000) or 23-88 (Supattapone et al. 2001) were used to study the significance of the N-terminus of PrP in prion disease. These mice can still propagate prions, although with an increased incubation time, suggesting that the unstructured domain of PrP^{C} modulates prion propagation. Additionally, mice expressing a PrP^{C} variant with only residues 23-31 deleted are notably less susceptible to prion infection and accumulate lower levels of PrP^{Sc}, indicating an essential role of the CC1 domain of PrP^{C} in the conversion to PrP^{Sc} (Das et al. 2020). On the other hand, transgenic mice expressing PrP^{C} that lack residues 23-111 do not accumulate PrP^{Sc} and remain healthy after exposure to scrapie prions (Westergard et al. 2011). These findings highlight the roles played by the N-terminal region in conversion of PrP^{C} to PrP^{Sc}.

1.10.3 The N-terminal region in structural studies

Recently, researchers used high-resolution cryo electron microscopy to investigate the structure of various rodent-adapted scrapie prion strains including RML, ME7, and 22L, as well as the infectious *ex-vivo* 263K Syrian hamster scrapie strain (Kraus et al. 2021, Hoyt et al. 2022, Hoyt et al. 2022, Manka et al. 2022, Manka et al. 2023). The results revealed a PIRIBS structure for these infectious prions, although the high-

resolution information was only available for the structured core region and residues 23-90 were eliminated using proteinase K. Structural studies have also been conducted on recombinant full-length prions with the N-terminus attached, yet due to the inherent flexibility of the N-terminus, high-resolution information was solely available for the core region (Wang et al. 2020, Wang et al. 2021).

A recent study examined four PrP variants without octapeptide repeats and with 1, 5, and 8 octapeptide repeats (Yu et al. 2021). These variants showed differences in overall amyloid structure, thermal stability, and cytotoxicity. Interestingly, the deletion of the octapeptide repeat region resulted in fewer twisted fibrils and weaker cytotoxicity. Although no detailed structural information was reported, the study implies that the presence or absence of certain regions of the N-terminus (e.g., the OR) could impact amyloid fibril conformation. This emphasizes the importance of conducting more research on the structure not only of the PK-resistant core but also of infectious prions carrying the N-terminal region.

1.11 EFFECT OF METAL IONS ON THE STRUCTURE OF PrP^{C} AND PrP^{Sc}

PrP^{C} is known for its metal ion binding capability through its N-terminal region (Hornshaw et al. 1995, Millhauser 2023), which led to further investigations on the role of metal ions in PrP^{C} physiology and prion pathogenesis. The N-terminal domain of PrP^{C} (residues 23-120, human numbering), which is largely unstructured, consists of two charged clusters, CC1 and CC2, an octapeptide repeat region, and a

hydrophobic region (Figure 1-1A) (Aguzzi et al. 2008). The OR is a repetitive sequence of eight amino acids (PHGGGWGQ) with histidines and tryptophans that can coordinate up to four copper ions each, with different binding affinities and geometries (Walter et al. 2007, Millhauser 2023). Two additional histidines (His96 and His111), located in the non-OR copper binding site, are also capable of binding copper (Walter et al. 2009).

There is a limited understanding of how metal binding affects the *in vivo* function of PrP^C. Nevertheless, Cu(II)-binding PrP^C has been proposed to have multiple functions, such as promoting endocytosis and trafficking of PrP^C (Pauly and Harris 1998, Brown and Harris 2003), acting as a copper uptake protein, and having an antioxidant function similar to superoxide dismutase (Brown et al. 1997). Moreover, Cu (II) can play a role in either promoting or reducing β-sheet conversion and amyloidal aggregation (Jones et al. 2004, Wells et al. 2006). While the atomic-level mechanisms of Cu (II)-mediated structural changes are still not fully understood, there is strong evidence indicating that copper helps in stabilizing interactions between the N-terminal and C-terminal domains leading to a compact PrP^C folding (Evans et al. 2016, McDonald et al. 2019).

The effects of copper on prion diseases are still a subject of debate, with conflicting results from various studies (Hijazi et al. 2003, Sigurdsson et al. 2003, Bocharova et al. 2005, Mitteregger et al. 2007). For instance, an experiment conducted on scrapie-infected mice revealed that administering a copper chelator delayed the onset of TSE

and decreased the levels of copper in the brain and blood, indicating that copper has a prion-promoting effect (Sigurdsson et al. 2003). In contrast, a different study on scrapie-infected hamsters demonstrated that administering copper delayed the onset of prion disease (Hijazi et al. 2003).

Although the structural impact of copper ions on the structure of PrP^{C} is somewhat understood, there is limited data available for the structural changes mediated by copper ions on the PrP^{Sc} structure. A study conducted by Wadsworth and colleagues examined the metal-ion occupancy in PrP^{Sc} isoform obtained from two biochemically distinct strains of sporadic CJD (Wadsworth et al. 1999). They used ethylenediaminetetraacetic acid (EDTA), a metal-chelating agent, to disrupt PrP^{Sc} copper binding sites and observed altered electrophoretic mobility of the cleavage products after PK digestion. As a result, the authors suggested that metal ions can impact the conformation of PrP^{Sc} (Wadsworth et al. 1999).

The aforementioned research indicates that the presence or absence of metal ions can influence the structural conformation of both PrP^{C} and PrP^{Sc} (Salzano et al. 2019). This presents an opportunity to manipulate the N-terminal conformation using chelators such as EDTA to favorably position the N-terminal for structural investigations. By selectively chelating metal ions, it may be possible to stabilize or destabilize certain conformations of the protein, allowing for more detailed structural studies of the N-terminus.

1.12 MOLECULAR DYNAMICS SIMULATION

Molecular dynamics (MD) simulation is a computational technique used to study the behavior and dynamics of atoms and molecules over time. The fundamental concept behind an MD simulation is straightforward - by knowing the precise positions of all atoms in a biomolecular system (such as a protein immersed in water, Figure 1-5, and potentially surrounded by a lipid bilayer), it becomes possible to calculate the forces exerted on each atom by all the other atoms. Consequently, Newton's laws of motion can be utilized to forecast the spatial positions of each atom over time. To achieve this, a stepwise progression through time is taken, involving the iterative calculation of forces on each atom, and subsequently utilizing these forces to update the position and velocity of each atom. Ultimately, the outcome is akin to a three-dimensional movie, providing a depiction of the system's atomic-level configuration at each moment during the simulated time span. These simulations offer notable advantages for multiple reasons. Firstly, they effectively capture the position and motion of every atom at any given time, which proves challenging with experimental techniques alone. Secondly, the simulation conditions are precisely defined and can be controlled. Factors such as the initial conformation of a protein, the presence of bound ligands, the existence of mutations or post-translational modifications, and the inclusion of other molecules in the environment can all be precisely manipulated. By conducting simulations under different conditions and comparing the results, one can discern the effects of various molecular perturbations across a wide range of scenarios (Wille et al. 2019, Rahman et al. 2022).

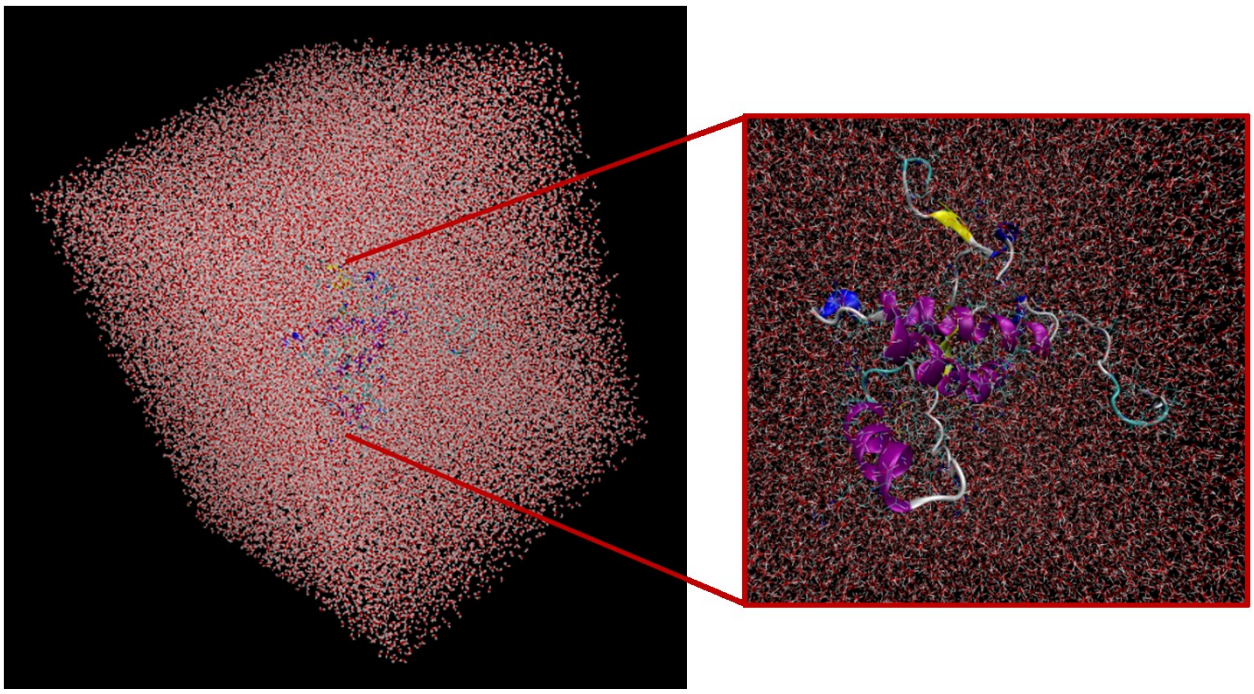

Figure 1-5. A molecular dynamics simulation box. The protein of interest, highlighted within a zoomed-in red box, is immersed in a water environment within a simulation box of specific dimensions.

1.12.1 Principles of molecular dynamics simulation

Solving the equations of atomic motions underlying the MD simulation method starts with setting the initial hypothetical positions and velocities of all atoms in the system. The starting configurations are normally obtained from the Protein Data Bank (PDB) (Rose et al. 2017). These starting structures are determined by X-ray crystallography, NMR techniques, or cryo EM. Only high-resolution structures can be used and, often, positions of missing atoms need to be assigned during the structure preparation (for example, parts of a protein that are too flexible to be determined experimentally or the hydrogen atoms that are not observed in X-ray experiments, must be added *in silico*).

Building such missing parts or introducing mutations or amino acid insertions can be done using several software packages such as Accelrys Discovery Studio Visualizer(BIOVIA 2017), VMD (Humphrey et al. 1996) or Chimera (Pettersen et al. 2004). After obtaining an initial conformation and incorporating solvent molecules in optimized positions, the system is ready to be initiated. To set the system in motion, velocities are randomly assigned at a specific temperature. These initial velocities, along with atomic masses, are used to calculate the forces acting on each atom throughout the MD simulation. These forces are determined based on a classical potential energy function referred to as the force field. A force field represents the dependence of the potential energy of the system on the position of each atom, taking into account details of chemical bonds such as the energy, length, and angles with respect to other bonds, as well as non-bonded interactions (Mackerell 2004). In turn, the corresponding forces determine how each atom's coordinates and velocities change with time.

While molecular dynamics simulations have made significant contributions to scientific research, it is important to acknowledge their limitations. These limitations stem from factors such as computational power and the constraints of time and length scales that can be effectively simulated. In many cases, MD simulations can only capture time scales that are orders of magnitude shorter than real-time processes. This means that simulating large systems or extended time periods can be computationally demanding and unfeasible, particularly when dealing with complex biological systems or materials. With current computational powers, simulations up to

the microseconds regimes are conceivable for systems of up to 10^5 atoms (Piana et al. 2014). In applications for the misfolding of proteins, such timescales might be sufficient to capture early misfolding events, given that they occur close to local energy minima. However, some of the misfolding events may involve the crossing of certain barriers in the free energy landscape, limiting the likelihood of capturing such events in a short MD trajectory. Furthermore, MD simulations heavily rely on force fields, which are mathematical models describing the interactions between atoms and molecules. These force fields are approximations based on empirical data and theoretical assumptions, introducing limitations to their accuracy. As computational efficiency continues to improve and advancements are made in force fields and algorithms, the potential for longer timescale simulations with higher accuracy in molecular dynamics will increase. This ongoing progress holds the promise of making MD simulations an even more valuable tool in the future.

1.12.2 Analysis of molecular dynamics trajectories

The positions and velocities of atoms as functions of time, extracted from MD trajectories, can serve as a valuable source of information. However, in most cases, drawing conclusions about the nature of misfolding events requires post-simulation processing and interpretation of the data in terms of physical, chemical, and structural biology descriptors that could be compared with experiments or used to interpret experimental findings. For these purposes, many techniques are available and used extensively.

Since amyloidogenic misfolding, by definition, results in a conversion of proteins from their native form into cross-β structured fibrils, changes in secondary structure (SS), as predicted by MD simulations, are amongst the most commonly reported analyses. Variations in secondary structure predicted in MD simulations are commonly interpreted as an indication of weak conformational integrity, local structural instability, and/or a sign of early stages of misfolding (Wille et al. 2019).

Root-mean-square deviation (RMSD) of backbone atoms in conformations generated by MD from an initial structure is a second major structural characteristic in MD analyses. RMSD provides a simple quantitative assessment of the general stability of the analyzed structure and, as such, it is commonly used to verify the convergence of MD simulations (Wille et al. 2019). It is natural to associate large RMSDs of globular domains in proteins with their structural vulnerability.

A closely related characteristic, root-mean-square fluctuations (RMSFs), is calculated at a per-residue basis and provides an indication for local backbone mobility. In globular proteins, RMSF is usually high in regions of flexible loops and relatively low for stable SS elements (Wille et al. 2019).

To characterize the dimensions of proteins or their aggregates, the radius of gyration (Rg) is frequently used. Rg is determined as the root-mean-square distance of atoms or residues from the center of mass of the chain or aggregate (Wille et al. 2019).

Electrostatic interactions between polar groups determine the stability of major SS elements in a protein and play an important role in maintaining the tertiary structure (Zhou and Pang 2018). Importantly, the identification of hydrogen bonds (HBs) and salt bridges (SB) formed or lost provides crucial atomic-level detail behind the propensity of a protein to misfold and on the stability of an aggregate. It has been hypothesized that the onset of PrP misfolding involves a disruption of the bonding network resulting in the exposure of the hydrophobic region. To characterize such changes, calculations of the solvent accessible surface area (SASA) are employed extensively. An increased exposure of hydrophobic residues is often interpreted as a sign of high structural vulnerability in an aqueous environment (Wille et al. 2019).

1.12.3 Studying the impact of mutations on PrP structure using MD simulation

The prion protein's conformational dynamics have been extensively investigated using molecular dynamics simulations. Various force fields, setups, and analyses have been employed for this purpose. Most MD simulations of PrP include only the protein component, i.e., the unglycosylated form without the GPI anchor. These simulations represent the recombinant PrP which is commonly used in laboratory studies. Early MD studies mainly captured local dynamics but more recent

investigations have provided a more comprehensive understanding of the protein's conformational dynamics and stability. Many mutations and polymorphisms have been identified in the prion protein, which contributes to the development and susceptibility of prion diseases, respectively. Nevertheless, the impact of these amino acid substitutions on the structure of PrP at the molecular level remains unknown. However, MD models by their nature are very well suited for probing the molecular-level impact of variations in the amino acid sequence. Replacements of individual residues, deletions, or insertions in the initial structure can be done easily in most cases and the resulting alterations in conformational dynamics can be directly determined. A vast number of studies employed MD simulations to investigate the effect of point mutations on PrP (Wille et al. 2019, Rahman et al. 2022). Numerous MD studies indicate that the pathogenic mutations V180I (fCJD), F198S (GSS), and V210I (fCJD) in the area of the hydrophobic core of PrP may destabilize the structure and dynamics of the bonding network across helix2, helix3, and the β1 and β2 bundle (van der Kamp and Daggett 2010, Meli et al. 2011, Rossetti et al. 2011, Behmard et al. 2012, Doss et al. 2013, Jahandideh et al. 2015, Chandrasekaran and Rajasekaran 2016). Therefore, various characteristics, such as the secondary structure and the number of hydrogen bonds of PrP are frequently found to be altered. For instance, MD studies of PrP monomers and dimers indicated that the T183A (fCJD) mutation may facilitate a α→β conversion in helix2 (Chebaro and Derreumaux 2009). Mutants such as Q212P (fCJD) exhibit significant differences in bonding between helix3 and other regions in comparison to WT PrP (Jahandideh et al. 2015). Other pathogenic substitutions in the globular domain, D178N (fCJD/FFI), T188R/K/A (fCJD) and

E200K (fCJD), also have been found to alter the bonding network in PrP (Meli et al. 2011, Guo et al. 2012, Doss et al. 2013). Comparative analyses of N-terminal mutations P101L (GSS), P104L/T/S (GSS), G113V (GSS), and A116V (GSS) in mouse PrP (Cong et al. 2013) revealed substantial variations in main-chain flexibility of the N-terminal region across the mutant proteins, with an increase in β-content for P101L (GSS). The comparison of numerous MD results for various PrP mutations is challenging due to the often differing conditions used, such as the temperature, pH, PrP construct length, and force fields.

1.12.4 Studying the impact of CWD polymorphism on PrP Structure using MD simulation

Compelling evidence supports the notion that cervid *Prnp* polymorphisms (described in section 1.8.4.1) have an impact on susceptibility to CWD. This prompts the question of how these individual amino acid substitutions influence the structure of PrP^C. While *in silico* molecular dynamics simulations have yielded valuable biophysical insights, the analysis has been limited to a small subset of the known polymorphisms.

Angers et al. investigated the impact of amino acid substitutions at codon 225 using MD simulation. It was observed that the presence of phenylalanine (F) at this position, which corresponds to the 225F PrP allele found in mule deer with lower susceptibility to CWD infection, facilitates the formation of side-chain hydrogen bonds

between tyrosine (Y) at codon 228 of the helix3 and aspartate (D) at codon 170 of the β2-α2 loop. This interaction is likely to contribute to the formation of a more stable protein structure (Angers et al. 2014). In another *in silico* study focusing on wild type 116A and the 116G polymorphism in white-tailed deer PrP, it was discovered that the 116G variant adopts a less stable conformation based on various parameters. Compared to the WT sequence, the 116G PrP variant exhibits increased structural fluctuations, with a larger radius of gyration (Hannaoui et al. 2017). The validity of these computational findings is supported by RT-QuIC assay, a highly sensitive cell-free technique used for amplifying prions. RT-QuIC involves the repetitive cycles of shaking and incubating the prion seed in a mixture containing recombinant PrP and Thioflavin T, which emits fluorescence when it binds to amyloid aggregates. When 116G or 116A recombinant PrP substrates were used with CWD-infected brain homogenate from WTD as a seed, the 116G variant displayed a higher rate of conversion (Hannaoui et al. 2017).

Overall, studies investigating the structural effects of polymorphism on the prion protein are very limited. More research is required to establish connections between PrP stability and susceptibility to CWD.

1.13 RESEARCH GOALS

The emergence of variant CJD in the UK, resulting from exposure to BSE prions in cattle, prompted global efforts to understand prion species barriers for the protection

of public health. While measures have limited human exposure to BSE prions, concerns remain about the human species' barrier to other animal prion diseases, such as CWD.

The primary structure variations in PrP^{C} across different species have a critical impact on the species barrier phenomenon. Mutations and polymorphisms in the amino acid sequence can modify this barrier and affect the susceptibility to chronic wasting disease. Moreover, distinct conformations of PrP^{Sc}, associated with specific prion strains, also contribute to the species barrier. Therefore, in this study, I have focused on examining the structural characteristics of both PrP^{C} and PrP^{Sc} in the context of chronic wasting disease. Such research is critical for understanding the disease mechanism and prion transmission, developing therapeutic strategies, and assessing the potential risks to both animal and human health.

The N-terminal region of infectious prions remains poorly understood due to its inherent flexibility, with even full-length prion studies failing to provide structural details on this region. However, various evidence emphasizes the significance of the N-terminal region in the function of the prion protein and the development of prion diseases. This highlights the existing knowledge gap and emphasizes the necessity for further investigation into the structure of the N-terminal region of infectious PrP. This study, for the first time, offers insights into the structural architecture of full-length and truncated brain-derived CWD prions. These prions were extracted from the

brains of CWD-infected cervidized transgenic mice and white-tailed deer. For this project, we hypothesize that the observed striation on the structure of full-length CWD prions potentially corresponds to the N-terminal component of the structure. Negative stained electron microscopy and immunogold labelling techniques were employed for the analysis, as detailed in Chapter 2.

In the second part of my thesis, I conducted all-atom molecular dynamics simulations to examine the protein structure of the white-tailed deer prion protein. The simulations included the wild type sequence as well as structural models incorporating three specific polymorphisms: 95H, 96S, and 116G. Utilizing various analysis tools, I investigated the structural and dynamic changes associated with each polymorphism. We hypothesize that the presence of these polymorphisms in deer PrP alters its stability and dynamics compared to the wild type PrP.

These findings have the potential to contribute to our understanding of both cellular and infectious prion protein associated with chronic wasting disease.

Chapter 2: Ex-vivo characterization of infectious CWD prions

2.1 INTRODUCTION

Prion protein (PrP) is a glycosyl-phosphatidylinositol (GPI) anchored glycoprotein of uncertain function found in all vertebrates (Prusiner 1982, Prusiner 1998, Aguzzi et al. 2008). Its normal form, PrP^{C}, contains an unfolded N-terminal domain and a well-defined C-terminal structure consisting of three α-helices and two β-strands. PrP^{C} can misfold and create an infectious form called PrP^{Sc} (Prusiner et al. 1982, Prusiner 1998, Aguzzi et al. 2008). This pathogen causes fatal neurodegenerative diseases in both animals and humans, including Creutzfeldt–Jakob disease, variant CJD, kuru, fatal familial insomnia, and Gerstmann–Sträussler–Scheinker disease in humans, bovine spongiform encephalopathy (BSE) in cattle, scrapie in sheep and goats, and chronic wasting disease (CWD) in cervids (Prusiner 1998, Colby and Prusiner 2011). CWD has affected various species, including elk, deer, moose, and reindeer since it was first detected in captive mule deer in 1967 (Williams and Miller 2002, Williams 2005). The disease has now spread to wild mule deer, white-tailed deer (WTD), elk, reindeer, and moose in different regions of the world, including 4 Canadian provinces, 30 American states, South Korea, Norway, Finland, and Sweden (Arifin et al. 2021, Otero et al. 2021, Tranulis et al. 2021, Otero et al. 2023).

The emergence of variant CJD in humans in the UK due to exposure to BSE prions from cattle led to global efforts to understand prion transmission barriers for public health protection (Wells et al. 1987, Nathanson et al. 1997). Although measures have limited human exposure to BSE prions, the emergence of animal prion strains with zoonotic potentials, like CWD, is a major concern (Hannaoui et al. 2022). Gaining

atomic-level information about the structure of PrP^{Sc} is a viable approach to prevent its accumulation and replication. However, compared to PrP^{C}, mammalian PrP^{Sc} is challenging to study due to its insolubility and tendency to aggregate. Despite these challenges, two distinct structural folds for prion fibrils have been proposed: a parallel in-register intermolecular β-sheet (PIRIBS) structure (Kraus et al. 2021, Hoyt et al. 2022, Hoyt et al. 2022, Manka et al. 2022, Manka et al. 2023) and a 4-rung beta solenoid (4RβS) model (Wille et al. 2009, Vázquez-Fernández et al. 2016, Spagnolli et al. 2019). The 4RβS model was initially established through X-ray fibre diffraction analysis of N-terminally truncated PrP^{Sc}, termed PrP 27-30 fibrils, and validated through low-resolution cryo electron microscopy studies of brain-derived and GPI anchorless mouse prion fibrils, as well as negatively stained imaging of brain-derived BSE prion fibrils. These studies demonstrated repeating structural features along the fibril axis with a spacing of 19.2 Å and a spacing of 4.8 Å between β-sheet strands. On the other hand, the PIRIBS model was established through high-resolution cryo EM studies of the brain-derived infectious prion protein, which showed monomers stacking in-register with a height of 4.9 Å per prion molecule. Both models were proposed for N-terminally truncated PrP, which lacks the N-terminal residues ~26 to ~93 (deer numbering).

The N-terminal region of the prion protein is crucial for the propagation of prion diseases, as highlighted by Hara et al.(2020). However, the N-terminal region of infectious prions remains poorly understood due to its inherent flexibility, with even full-length prion studies failing to provide structural information on this region.

Enzymes like proteinase K (PK) and Pronase E (PE) effectively degrade PrP^{C}, encompassing both its flexible N-terminal and structured C-terminal domains. Conversely, PrP^{Sc}, when subjected to PK digestion, residues ~ 90 to the C-terminus remain intact, while the N-terminus (residues ~23 to ~90) undergoes degradation. Interestingly, treatment of PrP^{Sc} with Pronase E preserves both the N-terminus and C-terminus of PrP^{Sc}, resisting digestion by PE. The N-terminal region's resistance to Pronase E digestion suggests an ordered structure that shields it from enzymatic breakdown.

In this study, electron microscopy was employed to examine full-length and N-terminally truncated chronic wasting disease prions purified from the brains of CWD-positive tg33 mice and white-tailed deer. The CWD prions were found to be morphologically heterogeneous with larger diameters compared to other prion strains. Interestingly, the full-length CWD prion fibrils were decorated with striations while the N-terminally truncated form were not. This suggests a potential correlation between the striations and the N-terminal region of the CWD prions. This observation was likely made possible by the incorporation of Ethylenediaminetetraacetic acid (EDTA) during the purification process. EDTA's ability to remove cations that engage with the N-terminus, potentially allowed the N-terminus to independently structure itself, thereby becoming visible for the first time. This finding opens the door to further investigating the N-terminal region of the prions.

2.2 MATERIAL AND METHODS

2.2.1 Animals

The animal experiments were carried out in compliance with the guidelines and policies of the Canadian Council on Animal Care, with approval from the Health Sciences Animal Care and Use Committee of the University of Alberta.

Tg33 mice: Transgenic mouse lines expressing the deer WT-*PrnP* allele were generated using procedures described in Meade-White et al. (Meade-White et al. 2007). 20% brain homogenates in phosphate-buffered saline (PBS) of experimentally infected WT/WT white-tailed deer carrying Wisc-1 strain (Johnson et al. 2006) was used as inoculum to infect tg33 mice. The CWD-positive tg33 mice brains were kindly provided by Dr. Juan Duque Velasquez, from the laboratory of Dr. Judd Aiken and Dr. Debbie McKenzie, Center for Prions and Protein Folding Diseases, University of Alberta.

White-tailed deer: A group of purifications were done on CWD-positive white-tailed deer samples that were provided by Dr. Juan Camilo Duque Velasquez, from the laboratory of Dr. Judd Aiken and Dr. Debbie McKenzie, Center for Prions and Protein Folding Diseases, University of Alberta. These samples were WT/WT CWD-positive farmed white-tailed deer whole-brain powder. The white-tailed deer was from a farm in North Battlefield, Saskatchewan and the brain was powdered in liquid nitrogen.

This animal was not in the clinical phase of CWD but was positive for PrP^{Sc} in both brain and lymph nodes.

2.2.2 Purification of CWD prions

CWD prions were purified from the brains of CWD-infected tg33 mice (transgenic mouse lines expressing the deer WT allele). Purification steps are based on Safar et al. 's previously developed protocol (Safar et al. 1998). Initially, four CWD-infected tg33 mice brains were homogenized at a final concentration of 20% (w/v) in PBS. Brain homogenates were then centrifuged at 500g for 5 min at 4 °C, and the supernatants were collected. 4% sarkosyl in PBS was added to reach a final concentration of 10% (w/v). The samples were then aliquoted in 1 ml screw-top centrifuge tubes and treated with PK at a final concentration of 50 µg/ml for one hour at 37°C with agitation. To stop the enzymatic reactions, phenylmethylsulfonyl fluoride (PMSF) was added at a final concentration of 1mM. The process was followed by adding sodium phosphotungstic acid (PTA), pH 7.2, to a final concentration of 2% for overnight incubation at 37 °C. Next, the samples were centrifuged for 30 minutes at 16,000g, and “pellet 1” was obtained and resuspended in 150 microliters of 0.2% sarkosyl in PBS. In CWD prion purification from the brain of CWD-positive white-tailed deer, pellet 1 went through another round of PTA purification and centrifugation (16,000g for 30 minutes) to obtain the “final pellet” which is better purified than pellet 1 with less background. However, in purification performed on the CWD-positive tg33 mice brains, sucrose step gradient was used as an alternative approach. In this method, pellet 1 was loaded onto a 40% and 80% sucrose column and centrifuged at

115,000g for 16 hours at 4 °C. After centrifugation, fractions of 500 microliters were drawn from the top to the bottom of the sucrose column and labelled alphabetically. The bottom of the column was washed with 100 microliters of sucrose buffer (10 mM Tris HCl pH 7, 1 mM NaN3, 0.2% sarkosyl) and labelled as “pellet wash”. This was done to recover the pelleted proteins from the bottom of the sucrose column. All samples were stored at -80°C.

For Pronase E (Protease Type XIV from Streptomyces griseous; Sigma Aldrich, cat. no. P5147) purification, a similar approach to PK purification was taken by replacing PK with 30 minutes PE (final concentration of 100 µg/m) incubation.

In some of the PK and PE purification, after the addition of PMSF, Ethylenediaminetetraacetic acid was added to a final concentration of 10mM as a chelating agent that binds to metal ions.

2.2.3 Bioassay

For the bioassay experiment, a total of 64 tg33 mice expressing deer PrP (Meade-White et al. 2007) were inoculated intra-cerebrally (IC) at 4 to 5 weeks of age. PK and PE purification protocols were used to purify fibrils from CWD-positive tg33 mice brains. 30 microliters of 1% infectious brain homogenates (PK and PE purified samples), 1% pellet 1 (PK and PE purified samples), 1% pellet wash (PK purified samples), and 1% interface fraction of sucrose column (for PE purified samples) were used to inoculate 48 tg33 mice (six groups of 8 mice). As negative controls, a total of

16 mice (four groups of 4 mice) were inoculated with 1% normal brain homogenate and 1% normal pellet 1 (PK and PE purified). Following inoculation, positive control mice were monitored until the appearance of clinical symptoms such as hunched back, weight loss, rigid tail, ataxia, and kyphosis. At this point, the mice were euthanized, and the brains were harvested, rinsed in PBS, and stored at -80°C. Negative control mice were monitored and euthanized after all the positive control mice had shown clinical signs and been euthanized. In each group of mice, half were male, and half were females.

2.2.4 Western blotting

An equal volume of 2x Laemmli Sample Buffer (Bio-Rad) and purified samples were mixed and heated at 100°C for 10 minutes. The samples were electrophoresed on 12% polyacrylamide gel (Bio-Rad) and ran for one hour at 150 Volts. The separated proteins were then transferred to polyvinylidene difluoride (PVDF; Millipore) membranes at 100 Volts for one hour. The blots were blocked with 5% (w/v) Bovine serum albumin (BSA) in 1x tris-buffered saline (TBS)-0.05% Tween 20 (TBST) at 4°C overnight. Incubation with primary antibody (D15.15; anti-PrP antibody used at 1:5000 dilution) was done at room temperature for one hour. Membranes were subsequently incubated for one hour with secondary alkaline phosphatase-conjugated anti-mouse IgG antibody (BioRad) at 1:10000 in TBST and developed by adding an alkaline phosphatase substrate (Bio-Rad). Images were acquired by chemiluminescent visualization using ImageQuant (GE Life Science).

2.2.5 Silver Staining

Purified samples were loaded onto a 12% polyacrylamide gel for 60 minutes (150 Volts). The gels were then fixed in 50% methanol and 12% acetic acid for 30 minutes and incubated in an sodium dodecyl sulfate (SDS) removal solution containing 10% ethanol and 5% acetic acid for another 30 minutes. To enhance PrP staining, the gels were incubated in the Farmer's solution (containing 0.15 g potassium ferricyanide, 0.05 g sodium carbonate, and 0.3 g sodium thiosulfate) for 2 minutes. Subsequently, the gels were rinsed with distilled water and transferred to a 0.2% (w/v) silver nitrate solution for 20 minutes. Finally, the gels were rinsed in distilled water and developed using a solution of 6% sodium carbonate in formaldehyde (stock solution of 30%). Once the signal was visible, the development was stopped using a 0.2% acetic acid solution.

2.2.6 Negative stain electron microscopy

To visualize the purified CWD prions and to assess the quality and quantity of the fibrils, negative stain electron microscopy was performed. 10 µl of purified samples were loaded onto a freshly glow-discharged 400 mesh carbon-coated copper grid (Ted Pella Inc. Redding, CA). Samples were adsorbed onto the grid surface for 1 minute and washed with one drop of (50 µl) 0.1 M and 0.01 M ammonium acetate solutions, respectively. Grids were then stained with freshly filtered 2% (w/v) uranyl acetate and air-dried after the excess solution was removed by blotting with Whatman

paper. The negatively stained samples were analyzed with an FEI Tecnai G20 electron microscope (FEI Company) with an acceleration voltage of 200 kV. Micrographs were recorded on an Eagle 4k x 4k CCD camera (FEI Company).

2.2.7 Width measurements

The maximum diameter between two crossovers of 135 and 221 fibrils was measured for PE and PK purified fibrils, respectively. Measurements were conducted using Adobe Photoshop's ruler tool. The pixel size of the micrographs was initially calculated by referencing the scale bar on the raw images. Subsequently, the measurement scale of the ruler tool was customized to match the pixel size of the micrographs.

2.2.8 Immunogold labelling

The immunogold labelling of the CWD fibrils was carried out using anti-PrP antibodies, namely Fab 29 and Fab 3. These Fab fragments detect prion protein epitopes at different positions. Fab3 and Fab 29 react with epitopes within residues 26KKRPKPGGWNTG37 and 218TQYQRESQAYYQ230 located at the N- and C-terminal regions of the deer prion protein, respectively (Senatore et al. 2020). Based on a previously published immunogold labelling protocol (Wille et al. 2007, Kamali-Jamil et al. 2021), purified CWD prions were deposited onto glow-discharged formvar/carbon-coated nickel grids (Ted Pella, Inc.) by adsorbing 5 µl of the prions onto the grids for approximately 5 minutes. The grids were then washed with three

drops (50 µl) of 0.1M and 0.01M ammonium acetate buffer, which was adjusted to pH 7.4. To enhance the accessibility of the epitopes, samples intended for labelling with Fab 29 antibodies underwent a treatment step involving incubation with 50 µl of 3M urea for 10 minutes. The samples were then incubated with the primary antibody (Fabs 3 and Fab 29) for 3 hours, followed by rinsing with 0.1% BSA in TBS solution five times. Next, the samples were incubated with a bridging goat F(ab)2 anti-human IgG F(ab')2 (Abcam ab98531) for 2 hours. The grids were then rinsed with 0.1% BSA in TBS solution five times, followed by incubation with a 5-nm gold-conjugated rabbit anti-goat IgG (Abcam ab202670) for 2 hours. This was followed by additional rinsing with 0.1% BSA in TBS solution five times, twice with TBS alone and twice with water. Control samples were processed in the same manner but without the primary Fab. Finally, the grids were rinsed with TBS solution and water, placed onto two drops of 2% PTA for final staining, air-dried, and stored for electron microscopy analysis.

The analysis of the samples was conducted using a Tecnai G20 transmission electron microscope (FEI Company) that operates with an acceleration voltage of 200 kV. The electron micrographs were captured using an Eagle 4k x 4k CCD camera (also manufactured by FEI Company).

2.2.9 Two-Dimensional (2D) Class Averaging

To classify the isolated fibrils based on their ultrastructural similarities, reference-free two-dimensional class averaging was performed. This is done by segmenting the fibrils, aligning and grouping the dataset into morphologically similar classes and

averaging the similar segments to enhance the signal-to-noise- ratio. In this study, the segmentation of the isolated fibrils was done by applying 50% overlapping boxes of 200 by 200 pixels (64 nm by 64 nm) using EMAN's boxer program (Ludtke et al. 1999), and the final class averaging was done using the EMAN's startnrclasses program.

2.2.10 3D helical reconstruction of amyloid fibrils

From hundreds of electron microscope images, only the fibril images that contained an isolated fibril with a complete helical twist (180°) were selected. Micrographs acquired for image processing purposes were recorded at a nominal magnification of 29,000x with a pixel size of 3.07 Å per pixel. Using EMAN's boxer program (Ludtke et al. 1999), the suitable fibrils were segmented along their helical axis into overlapping boxes of 300 by 300 pixels (equal to 92.1 by 92.1 nm). The boxes were centered and spaced with 95%-99% overlap between the segments. Based on the repeat distance of the helical fibril, the angular orientation of each box was calculated. Back projection is the method used to generate a preliminary three-dimensional (3D) reconstruction based on the angles assigned to each box in the set (Vázquez-Fernández et al. 2016, Kamali-Jamil et al. 2021). The image processing software SPIDER was used for the reconstruction (Frank et al. 1996). The reconstruction was then refined, and low-pass filtered to 20 Å, and a two-fold symmetry was applied. Other 3D reconstructions of the same fibril were generated by changing the overlap between the boxes. All the generated reconstructions went through an iterative process of alignment and averaging to help refine the final 3D reconstruction. The

software UCSF Chimera (Pettersen et al. 2004) will be used to visualize the 3D reconstruction.

2.2.11 Two-dimensional Fourier transform

The spacing of the striations was accessed using Gwyddion, an open-source software (Nečas and Klapetek 2012).

2.3 RESULTS

Transgenic mice expressing the deer WT-*Prnp* allele (Meade-White et al. 2007) were intracerebrally inoculated with 20% brain homogenates in PBS from experimentally infected WT/WT white-tailed deer (Johnson et al. 2006, Duque Velasquez et al. 2015). Infectious protein were purified from the brains of terminally ill CWD-positive tg33 mice and subjected to subsequent structural analyses. Another set of purifications was performed on brain samples of WT/WT CWD-positive farmed white-tailed deer, which was obtained from a farm in Saskatchewan. This animal was not in the clinical phase of CWD but tested positive for the abnormal prion protein, PrP^{Sc}, in both the brain and lymph nodes.

2.3.1 Purification of CWD prions

Proteinase K is a serine endoprotease originally discovered in the fungus Engyodontium album (Ebeling et al. 1974). PK has been traditionally used to detect

and isolate prions due to its capability to hydrolyse PrP^{C} and other proteins while preserving the amyloid core (residues 93 to 233) of PrP^{Sc}, also known as PrP 27-30 or N-terminally truncated PrP^{Sc} (Prusiner et al. 1983, Safar et al. 1998, Leffers et al. 2005). To isolate the infectious prions in this study, PTA was added as a precipitating agent for PrP^{Sc}, in addition to PK (Figure 2-1A) (Safar et al. 1998, Lee et al. 2005, Wille et al. 2009, Levine et al. 2015). To compare the full-length and N-terminally truncated forms of CWD prions, a similar experiment was conducted with the use of Pronase E instead of PK, which eliminates PrP^{C} but leaves the full-length PrP^{Sc} intact (D'Castro et al. 2010) (Figure 2-1C). In addition to the PTA purification, we incorporated a sucrose step gradient centrifugation step to enhance the purification and eliminate the lipids and peptides. For this purpose, the semi-purified “pellet 1” from the PTA purification step was subjected to ultracentrifugation and passed through a sucrose step gradient (40% and 80%) . The prion protein with a density of ~1.2 g/ml was projected to move to the interface between 40% and 80% sucrose, with densities of 1.1 g/ml and 1.4 g/ml, respectively. Following ultracentrifugation, fractions were sequentially collected from the top to the bottom of the sucrose step gradient column and labelled as fractions A to H. The bottom of the column was subsequently washed with 100 µl of sucrose buffer and designated as "pellet-wash." After the CWD prions were isolated from the CWD-positive tg33 mice brains, the quality and purity of the samples were evaluated by performing Western blotting and silver-stained SDS gels (Figure 2-1). The silver stain signals indicate that the level of impurities in the sample is decreasing with each step of the purification process (Figure 2-1A and C). The Western blot signal exhibits an increase in the prion protein

concentration throughout the purification process, with the strongest signals detected in the "pellet 1" and "pellet-wash" fractions, indicating that the purification process successfully enriched the prion protein (Figure 2-1B and D). According to Levine et al. PrP may form a complex with PTA, increasing its density to around 1.4 g/ml (Levine et al. 2015), which explains the strong signal observed for the pellet-wash sample.

Pellet 1 and pellet-wash for both PK and PE isolated prions displayed the characteristic three bands corresponding to di-, mono-, and no glycosylated isoforms (black and white arrowheads, Figure 2-1B and D). As anticipated, full-length prions purified using PE have a larger molecular mass, ranging from 25 kDa to 36 kDa, than those purified using PK, which have a smaller molecular weight range from 16 kDa to about 30 kDa.

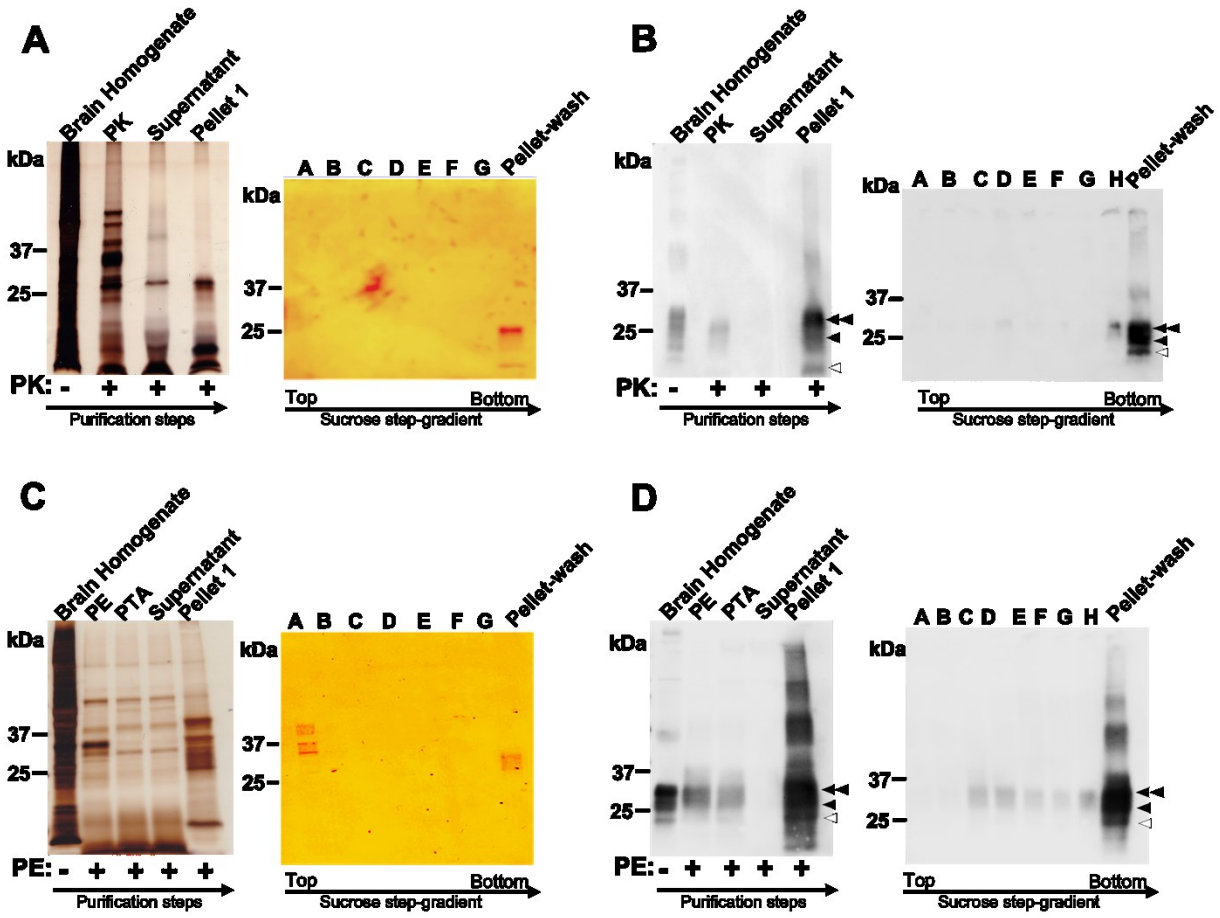

Figure 2-1. Purification of CWD prions from CWD-positive tg33 mice brain using PK and PE. (**A**) Silver stain SDS-PAGE gel of samples taken from different steps of the purification using PK. Sucrose step gradient centrifugation fractions were analyzed on a separate gel showing the purity of the sample with a weak signal for pellet-wash (the SDS-PAGE gel image was enhanced for the signal to become visible). Fractions A to H are samples taken from top to bottom of the sucrose step gradient tube, and pellet-wash is the resuspension of the pellet from the bottom of the sucrose step gradient tube. (**B**) The representative Western blot for the same brain samples of the PTA purification process and the sucrose step gradient fractions. The PK-digested pellet 1 and pellet-wash display the characteristic three bands corresponding to di-, mono-, and un-glycosylated isoforms (double black arrowhead, single black arrowhead and single white arrowhead, respectively). Fraction D was taken from the 40% and 80% sucrose interface showing a slightly stronger signal for prions. However, the pellet-wash fraction shows the strongest signal for CWD prions.

(**C**) Silver stain SDS-PAGE gel of samples taken from different steps of the purification using PTA and PE. Fractions A to H from the sucrose step gradient centrifugation were analyzed on a separate gel showing the purity of the sample with a weak signal for pellet-wash (the SDS-PAGE gel image was enhanced for the signal to become visible). (**D**) The representative *W*estern blot for the same brain samples was purified using PTA and PE and the sucrose step gradient fractions. The PE-digested pellet 1 and pellet-wash displayed the characteristic three bands corresponding to full-length di-, mono-, and no glycosylated isoforms (black and white arrowheads). Fraction C was taken from the 40% and 80% sucrose interface showing a slightly stronger signal for prions. However, the pellet-wash fraction shows the strongest signal for CWD prions. All *W*estern blots were developed using the D15.15 anti-PrP monoclonal antibody.

To confirm whether the purified CWD prions are infectious, we intracerebrally inoculated tg33 mice with 1% infectious brain homogenates (PK and PE purified samples), 1% pellet 1 (PK and PE purified samples), 1% pellet-wash (pelleted proteins recovered from the bottom of the sucrose step-gradient column) from PK purified samples, and 1% from 40% and 80% sucrose interface fraction from the PE purified samples. Following inoculation, mice were monitored until the appearance of clinical symptoms such as hunched back, weight loss, rigid tail, ataxia, and kyphosis. At this point, the mice were euthanized. Clinical symptoms of prion disease were observed in all groups of infected mice, confirming that these preparations contain infectivity. As negative controls, tg33 mice were inoculated with 1% normal brain homogenate and 1% normal pellet 1 (PK and PE purified), and none of these mice showed clinical symptoms of prion disease. As seen in Table 2-1, tg33 mice inoculated with brain homogenate and pellet 1 (both for PK and PE experiment)

showed slightly shorter incubation time compared to mice inoculated with sucrose step gradient interface fraction or pellet-wash.

Table 2-1. Infectivity of the purified CWD prions. Intracerebral inoculation of tg33 mice with the CWD prion samples obtained during purification experiments. (**A**) transgenic mice were inoculated with brain homogenate, pellet 1, and pellet-wash from PK-treated samples, and all came down with CWD in 349, 360, and 369 days past inoculation, respectively. (**B**) Transgenic mice were inoculated with brain homogenate, pellet 1, and 40% and 80% sucrose interface fraction from PE-treated samples, and all came down with CWD in 333, 330, and 399 days past inoculation, respectively.

A

Mouse Line	Inoculum PK-purified	Sick/Total	Incubation Time (Days ± SEM)
Tg33	Brain Homogenate	7/8 One found dead	349± 16
Tg33	Pellet 1	6/8 two found dead	360±18
Tg33	Sucrose Step gradient pellet (pellet-wash)	7/8 One found dead	369±16

B

Mouse Line	Inoculum PE-purified	Sick/Total	Incubation Time (Days ± SEM)
Tg33	Brain Homogenate	7/8 One found dead	333± 8
Tg33	Pellet 1	7/8 One found dead	330±6
Tg33	Interface of %40 and %80 sucrose	7/8 One found dead	399±24

2.3.2 Transmission electron microscopy of CWD fibrils

Following the successful isolation of CWD prions from the brains of CWD-positive tg33 mice, CWD fibrils were observed and their morphology was investigated using transmission electron microscopy. Pellet 1 and all fractions (A to H) of the sucrose step gradient purification (Figure 2-1) were subjected to negative-stain electron

microscopy. As expected, and in correlation with the signal intensity in the Western blot (Figure 2-1B), pellet 1 and pellet-wash from PK-purified samples exhibited a high quantity of fibrils with a clear background (Figure 2-2A). All other sucrose step gradient fractions, including fraction D (40% and 80% interface), which revealed faint bands on the Western blot, had no or very few fibrils (Figure 2-1B). On the other hand, pellet 1 from PE-purified samples had a dense background (Supplementary Figure 2-1), whereas fraction C (interface of 40% and 80%) and pellet-wash micrographs showed a clear background with a high quantity of fibrils (Figure 2-2B), which was consistent with their Western blot signal in Figure 2-1D. Other sucrose step gradient fractions showed no or very few fibrils, which correlated with their faint band on the Western blot (Figure 2-1D).

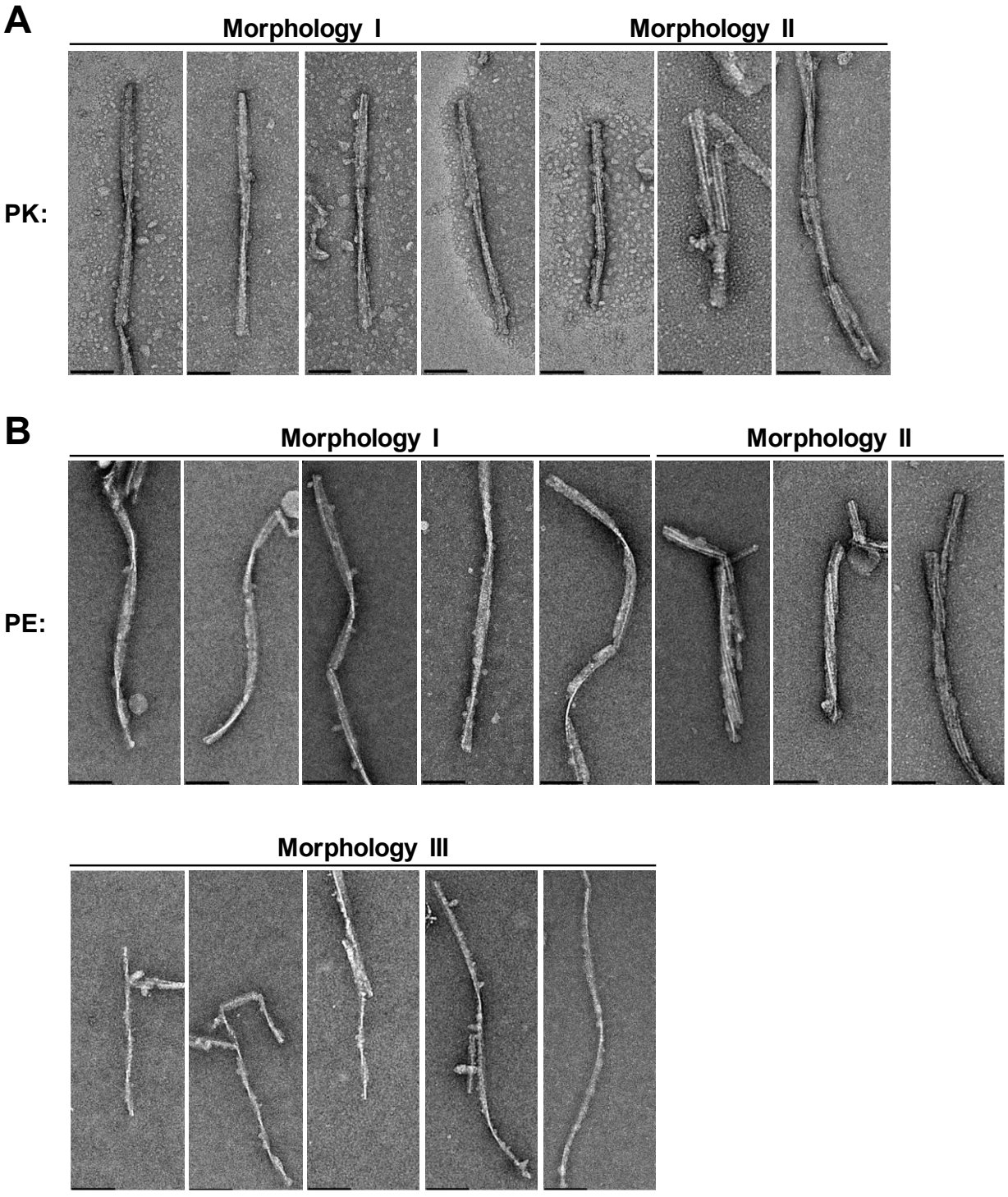

Figure 2-2. Gallery of negatively stained electron micrographs of purified CWD prion fibrils showing heterogeneous morphologies. (**A**) N-terminally truncated

(PrP 27-30) PK-purified CWD prion fibrils displaying ribbon-like (morphology I) and cylindrical-shaped (morphology II) fibrils. These fibrils have a width of about 35 nm. (**B**) Full-length PE-purified CWD fibrils display three types of morphologies. Ribbon-like (morphology I) and cylindrical shaped (morphology II) with a width of about 35 nm. Plus, thinner fibrils with a width of about 25nm are named morphology III. Scale bar = 100 nm.

Various fibril morphologies were observed in both PK and PE purifies fibrils (Figure 2-2). Morphology I, with a ribbon-like twist, was the dominant morphology in both PK and PE purified samples (Figure 2-2). Morphology II, with a cylindrical shape, was the second dominant morphology in PK and PE-isolated fibrils (Figure 2-2). Interestingly, A third recognizable morphology was only seen in PE-purified samples (Morphology III in Figure 2-2B). These fibrils are thinner (maximum width of less than 25 nm) compared to Morphology I and II fibrils, which have a maximum width of about 35 nm.

The PK-sensitive prion, a disease-associated isoform of PrP, is eliminated by PK treatment (Safar et al. 1998, Safar et al. 2005, D'Castro et al. 2010). Pronase E, on the other hand, has been shown to preserve not only full-length prions but also PK-sensitive prions through a mild digestion (D'Castro et al. 2010). Thus, it can be hypothesized that Morphology III observed only in PE-purified samples may be associated with the PK-sensitive prion forms, which are exclusively retained in PE-treated samples.

To conduct further analysis of the negatively stained micrograph, we measured the maximum diameter between two crossovers of 93 and 156 fibrils for PK and PE purified fibrils, respectively (Figure 2-3). This measurement included all different morphologies. The results show that PK-treated fibrils have a mean width of 32 nm, while full-length PE-treated fibrils are significantly wider with a mean width of 36 nm (p-value of 1.68281E-05). In correlation with the thinner fibrils (Morphology III) seen in the PE purified samples, there are about 10 fibrils with a width of 25 nm and under, while PK fibrils have a width of greater than 26 nm (Figure 2-3). The variability in fibril widths within the PE-treated samples (Figure 2-3B) highlights the heterogeneity of these fibrils in comparison to the PK fibrils.

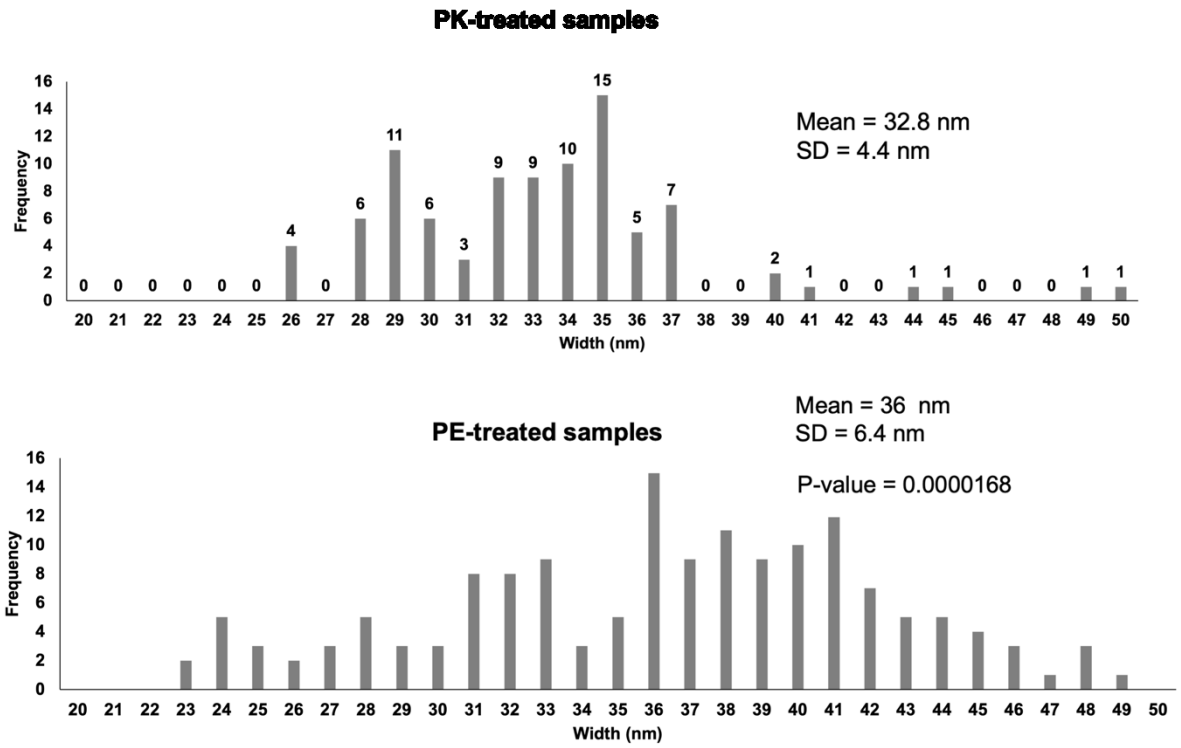

Figure 2-3. Width distribution of negatively stained PK and PE purified prion fibrils. (**A**) Histogram of the maximum width of 92 PK-treated samples with a mean of 32.8 nm and a standard deviation (SD) of 4.4nm. The numbers above the bars represent the number of fibrils with that width. (**B**) Histogram of the maximum width of 156 PE-treated samples with a mean of 36 nm and a standard deviation of 6.4nm. The measurements were done using Adobe Photoshop's ruler tool (section 2.2.7).

2.3.3 Striations of the PE-treated CWD fibrils

Intriguingly, when comparing the negatively stained micrographs of PK- and PE-treated samples, a significant observation was made. The fibrils derived from the PE-treated samples displayed a distinct pattern of striations along the fibril axis (Figure 2-4A). These striations were solely present on the PE-treated samples and were never observed on the PK-treated samples. However, not all the fibrils from the PE-treated

samples had these striations. The PK- and PE-treated samples differ solely in the presence of the N-terminal region (residues ~26 to ~93) in the latter. This suggests a potential connection between the striations and the N-terminal portion of the CWD prions and possibly marks the first time the N-terminus has become visible as a distinct structure on the infectious prion fibrils. This observation was likely made possible by the incorporation of EDTA during the purification process. EDTA can remove cations that engage with the N-terminus, potentially allowing the N-terminus to independently structure itself (further discussed in section 2.3.4).

Using Gwyddion software, the fast Fourier Transform (FT) was calculated on a PE-treated fibril that had clear striations. The diffraction pattern revealed two peaks, indicating the presence of repeating units (striations), as depicted in Figure 2-4A. We used these peaks to calculate the distance between striations, which was approximately 3.5 nm. To verify the accuracy of the calculations, we strengthened the striation pattern using 2D class averaging and improved the signal-to-noise ratio, as demonstrated in Figure 2-4B. We then subjected the resulting 2D class average image to fast FT calculation using Gwyddion software, which generated well-defined peaks on the diffraction pattern (Figure 2-4B) that once again confirmed the 3.5 nm spacing of the striations.

We hypothesize that the striations might be the N-terminal component of the structure, as they were only observed on the PE-treated samples and not on the PK-

treated sample. This is supported by the fact that Pronase E retains the N-terminal region (residues ~26 to ~93) while PK digests these residues. Furthermore, the alignment of some of the fibril striations along one side of the fibril, as depicted in the zoomed-in image of Figure 2-4A, further strengthens our hypothesis.

Despite the critical function of the N-terminal region in the propagation of prion diseases (Hara and Sakaguchi 2020), all brain-derived investigations at high resolution have only been conducted on PK-treated samples that lack this region. This is mostly because the N-terminus (residues ~26 to ~93) is considered an unstructured domain that is flexible and contributes to lower-resolution structural observations. However, the fact that an enzyme like PE cannot digest the N-terminal region alone implies that this region has an ordered structure that prevents the enzyme from interacting with and digesting it. Therefore, we conducted further experiments with a focus on the striations to explore the possibility that the N-terminal residues of the prion protein could be responsible for the formation of the striations.

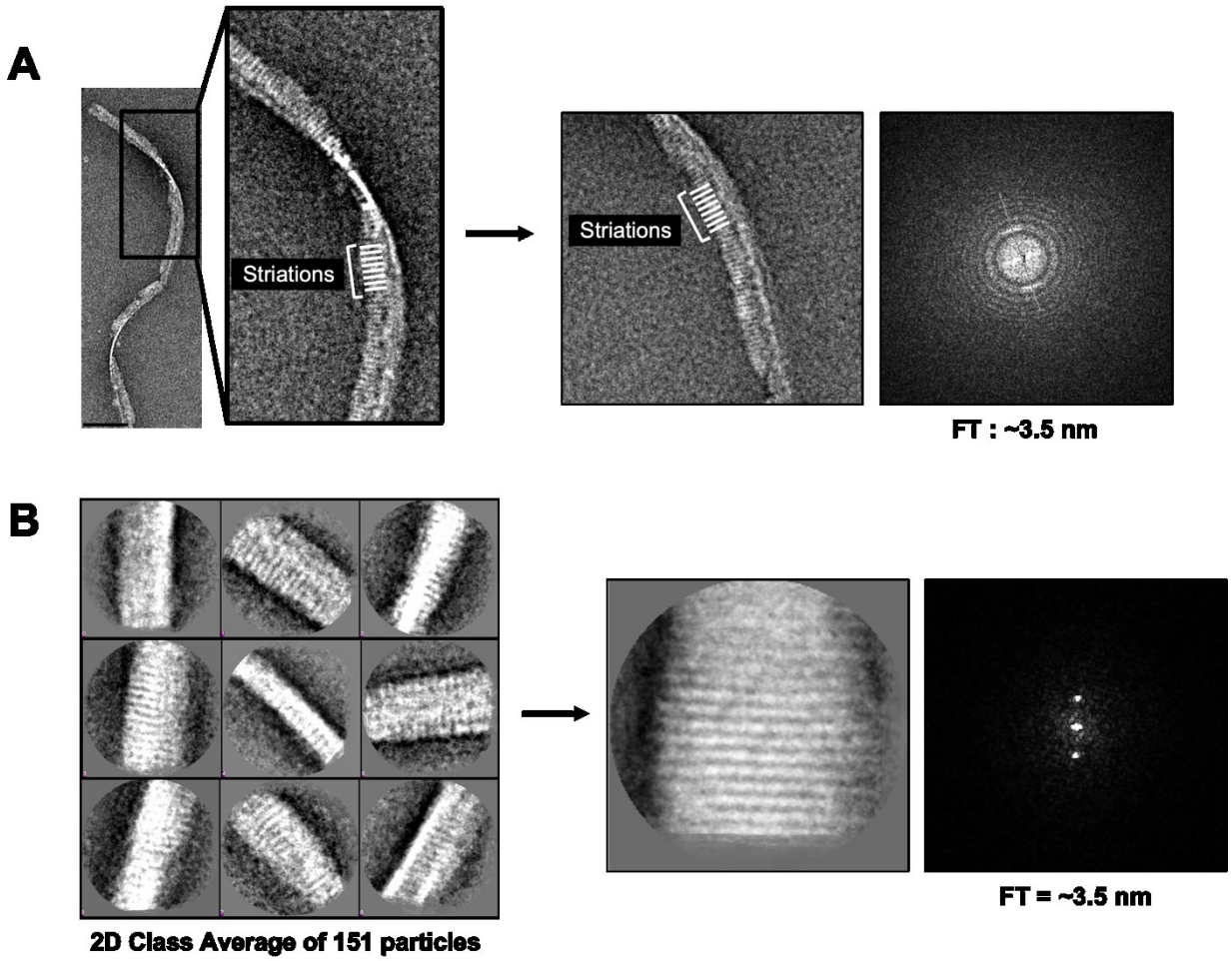

Figure 2-4. Negatively stained micrographs of fibrils with striations in PE-treated samples. (**A**) A zoomed-in view of a negatively stained PE-treated sample demonstrating striation and its diffraction pattern. The recurrence of the striations creates peaks on the diffraction pattern that aids in determining the spacing of the striations, which is around 3.5 nm. (**B**) Two-dimensional class average of fibrils with striations. A total of 151 particles were collected, categorized, and averaged based on their similarity. The diffraction pattern of the 2D class average image displays two strong peaks for the striations with a separation of roughly 3.5 nm.

2.3.4 Effect of Ethylenediaminetetraacetic acid on the striations

EDTA is a chelating agent that can bind to divalent metal ions such as copper with high affinity. The N-terminal region of the prion protein contains the octapeptide repeat region, which contains histidine and tryptophan residues that can coordinate up to four copper ions (Zahn et al. 2000, Walter et al. 2006, Salzano et al. 2019). The use of EDTA during prion purification can prevent the N-terminal region from interacting with copper ions, potentially altering its conformation. In this study, the purification protocols used to isolate CWD prions from the brains of infected tg33 mice were comparable, except for the use of proteolytic enzymes (PK or PE) and EDTA. In the first set of experiments (Figure 2-1), EDTA was used with PE and was eliminated when PK was used due to the importance of calcium as a cofactor for proteinase K. In previously presented data (Figure 2-2 and 2-4), the observed striations on PE-treated samples were a result of the purification process involving EDTA. To explore the impact of EDTA on striations, the same experiment was repeated without the use of EDTA. Figure 2-5A and B show the *W*estern blot for the purification process and fibrils morphology, respectively. Interestingly, Figure 2-5C shows that the striations of the fibrils were less orderly than those observed in the experiment with EDTA (Figure 2-4).

Further analysis using FT calculation gave a spacing value of around 3.3 nm for the striations. When the diffraction patterns of the fibrils treated with EDTA and without EDTA were compared, it was observed that the peaks for the striations were stronger in the former, indicating that EDTA can affect the arrangement of the striations.

Previous studies have suggested that the conformation of PrP^{C} and PrP^{Sc} can be influenced by the presence or absence of metal ions. Several studies on PrP^{C} have proposed that copper ion binding to the N-terminus can facilitate N- to C-terminus interactions (Salzano et al. 2019). Furthermore, it has been demonstrated by Wadsworth et al. that metal ions could influence the conformation of the PrP^{Sc} (Wadsworth et al. 1999). Based on these observations, it is possible that metal ion removal by EDTA can have an impact on the arrangement of the N- and C-terminus, resulting in changes in the appearance of the striations on negatively stained micrographs.

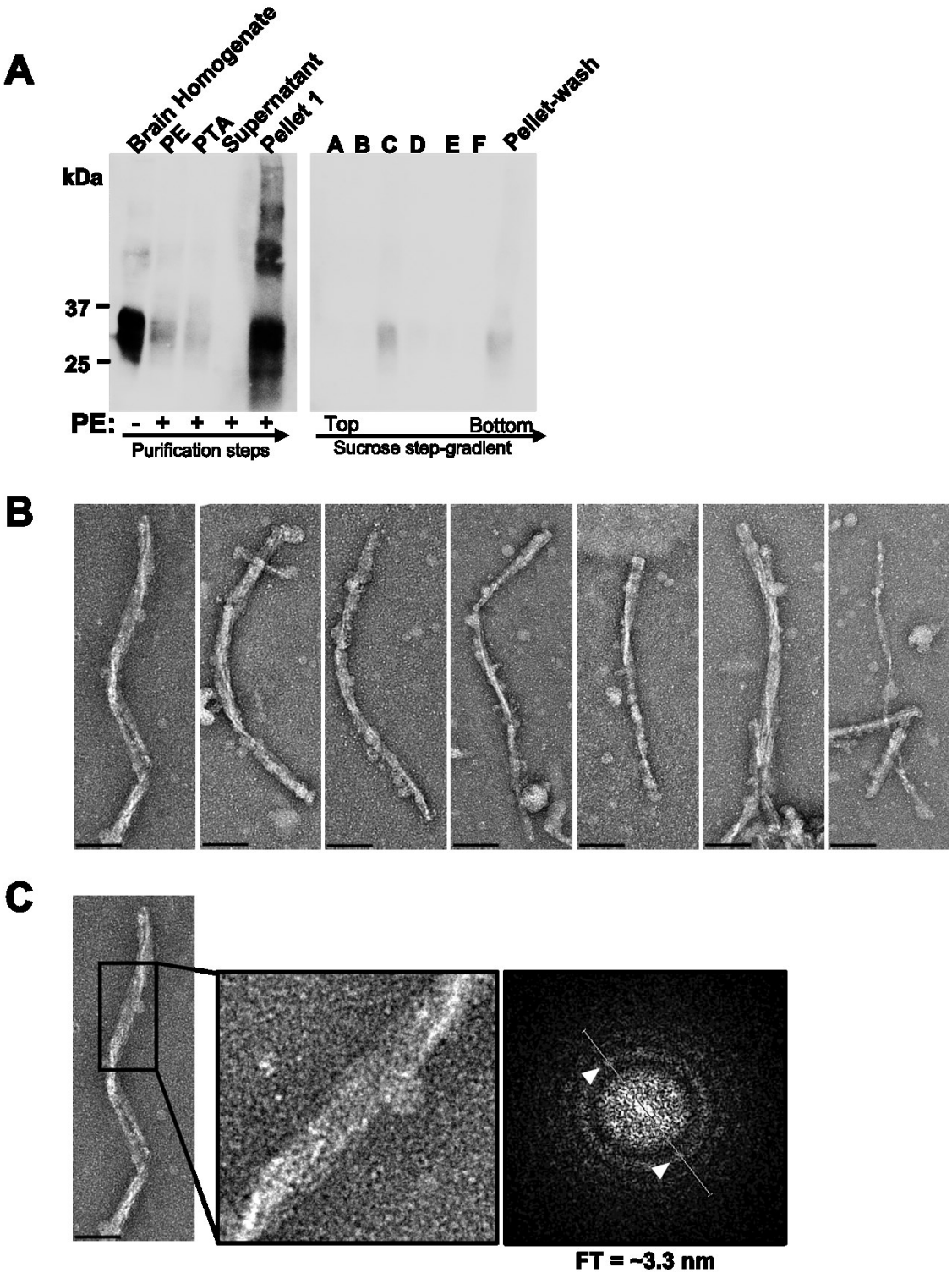

Figure 2-5. Purification of CWD prions from brains of infected tg33 mice using PE in the absence of EDTA. (**A**) The *W*estern blot of samples taken from different

steps of the purification. Fractions A to F from the sucrose step gradient centrifugation were analyzed on a separate gel. CWD prion signal is observed in the PE-digested pellet 1, fraction C, and pellet-wash. The *W*estern blots were developed using the D15.15 anti-PrP monoclonal antibody. (**B**) Gallery of negatively stained electron micrographs of full-length PE-treated CWD fibrils purified in the absence of EDTA. Scale bar = 100 nm. (**C**) A zoomed-in view of a negatively stained micrograph demonstrating weak striation and its representative diffraction pattern. The recurrence of the striations creates peaks on the diffraction pattern (denoted with white arrowheads), which aids in determining the spacing of the striations, which is around 3.3 nm.

The previously presented data on the PK-treated sample (Figure 2-1A and B, and Figure 2-2A) did not involve the use of EDTA, and striations were not observed on the fibrils. However, we conducted an experiment where PK was used in the presence of EDTA to confirm that the observed striations in the PE-treated sample were not due to the presence of EDTA. The *W*estern blot analysis for the purification process and fibrils morphology are shown in Figure 2-6A and B, respectively. As expected, the striations were not observed on the fibrils (Figure 2-6B). The fast Fourier transform analysis of the fibrils produced using PK in both conditions, with and without EDTA, was calculated in Figure 2-6C. No visible peaks were observed in the diffraction patterns, indicating the absence of striations (repeating units). The results of this experiment have demonstrated that under identical purification conditions and by only altering the proteolytic enzyme, the striations emerge on the PE-treated fibrils.

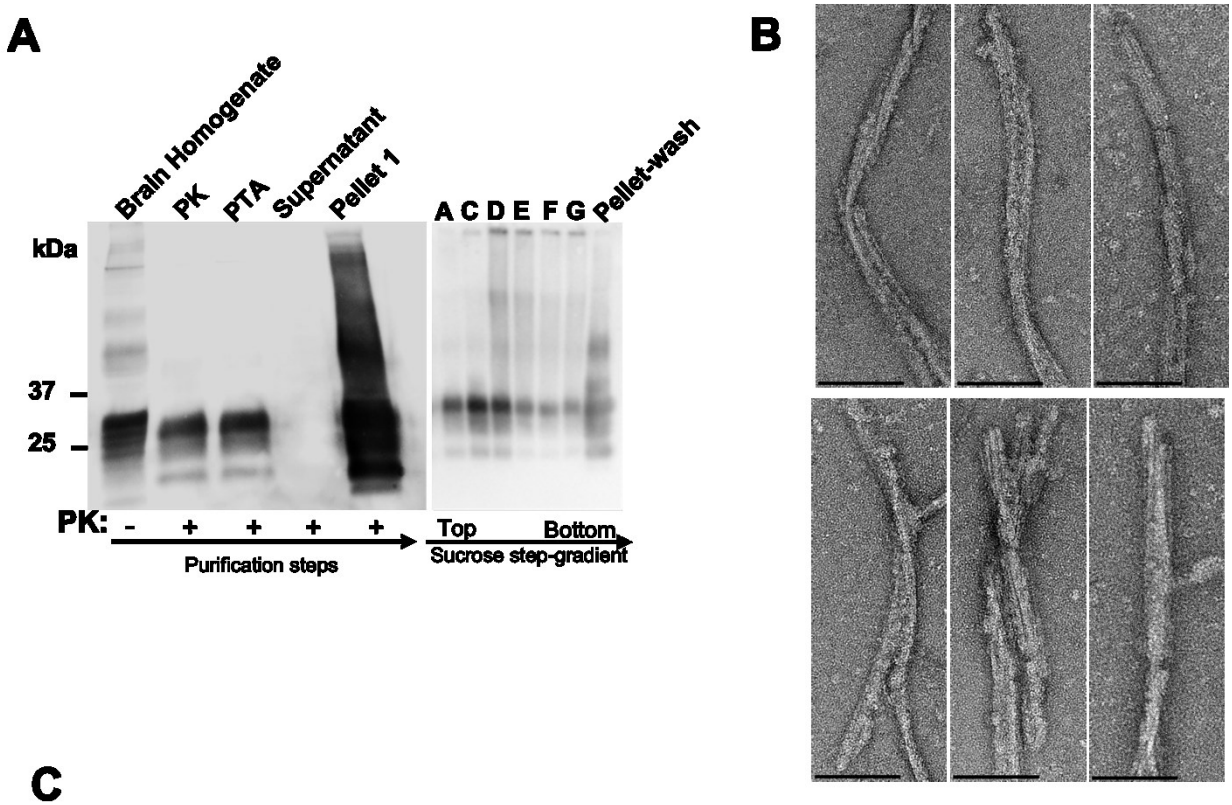
A
Brain Homogenate
PK
PTA
Supernatant
Pellet 1
A C D E F G
Pellet-wash
kDa
37
25
PK: - + + + +
Purification steps
Top
Bottom
Sucrose step-gradient
B
C
PK (-)
EDTA
PK (+)
EDTA

Figure 2-6. Purification of CWD prions from the brain of infected CWD-positive mice brain using PK and EDTA. (**A**) The Western blot of samples taken from different steps of the purification. Fractions A to G from the sucrose step gradient centrifugation were analyzed on a separate gel. CWD prion signal is observed in the PK-digested pellet 1 and all fractions of the sucrose step gradient. The *W*estern blots were developed using the D15.15 anti-PrP monoclonal antibody. (**B**) Gallery of negatively stained electron micrographs of N-terminally truncated PK-treated CWD fibrils purified in the presence of EDTA. Scale bar = 100 nm. (**C**) A zoomed-in view of a negatively stained micrograph of fibrils purified from PK-treated samples with and without the use of EDTA, demonstrating no striation and no peaks on their diffraction pattern.

To confirm the presence and absence of the N-terminal region (residues ~26 to ~93) in the PE- and PK-treated samples, two experiments were conducted: Western blot and immunogold labelling. Western blot analysis was carried out using anti-PrP antibody fragments, Fab 3(26-37) and Fab 69(91-101), which target the very N-terminus and truncated N-terminal regions, respectively. Fab 3 and Fab 69 react to linear epitopes, 26KKRPKPGGWNTG37 and 91GGWGQGGTHSQ101, of the deer prion protein, respectively (Senatore et al. 2020). The results revealed that Fab3 was unable to detect prions in the PK-treated sample as the epitope was digested during PK treatment, while Fab 69 was able to detect it. However, both Fab3 and Fab 69 were able to detect the full-length prions in the PE-treated samples. These findings are illustrated in Figure 2-7.

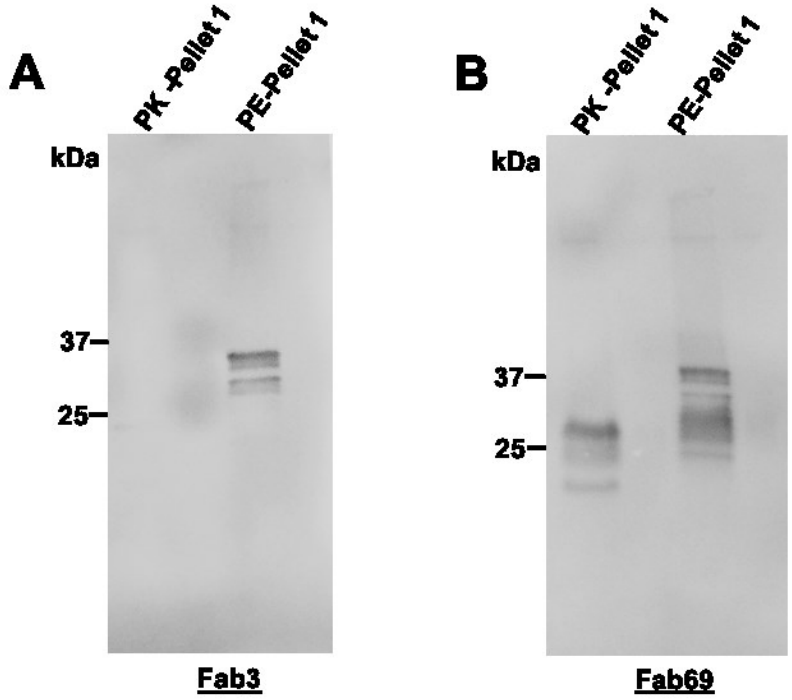

Figure 2-7. Western blot analysis showing immunoreactivities of purified CWD prions to anti-PrP antibody Fab 3 and Fab 69. (**A**) Anti-PrP Fab 3 binds strongly to the polybasic stretch of the prion protein's N-terminal. No bands are detected for pellet 1 of PK-treated samples. However, clear signals are seen for pellet 1 for PE-treated samples, indicating N-terminal is present in the PE-treated samples. (**B**) Anti-PrP Fab 69 detects residues 91 to 101 of the prion protein. The high reactivity of Fab 69 to both PE and PK-treated samples is observed. The higher molecular weight band for PE-pellet 1 is another indicator of the intact length of the prion protein in this sample.

To investigate the presence of the N-terminal region (residues ~26 to ~93) in the tertiary structure of fibrils from PE- and PK-treated samples, an immunogold labelling experiment was conducted using the pellet-wash (pelleted proteins recovered from the bottom of the sucrose step gradient column) from the purification process

containing EDTA. Two anti-PrP Fab fragments were used, Fab 29 and Fab 3, which recognize the very C- and N-terminal regions of the prion protein, respectively.

Fab 29 binds within residues 218TQYQRESQAYYQ230 of deer prion protein which is present in both PE- and PK-treated samples. This region is situated in the globular domain of PrP, and therefore purified samples underwent an epitope retrieval step using urea as a denaturing agent. However, despite this pre-treatment, Fab 29 mainly detected PrP aggregates in both PE- and PK-treated samples (Figure 2-8), and not many gold particles were attached to the fibrils. This suggests that Fab 29 epitopes are not easily accessible in PrP's fibrillar state. The negative control samples, where the primary Fab fragment was not used, had very few or no gold particles, indicating the specificity of the immunogold labelling.

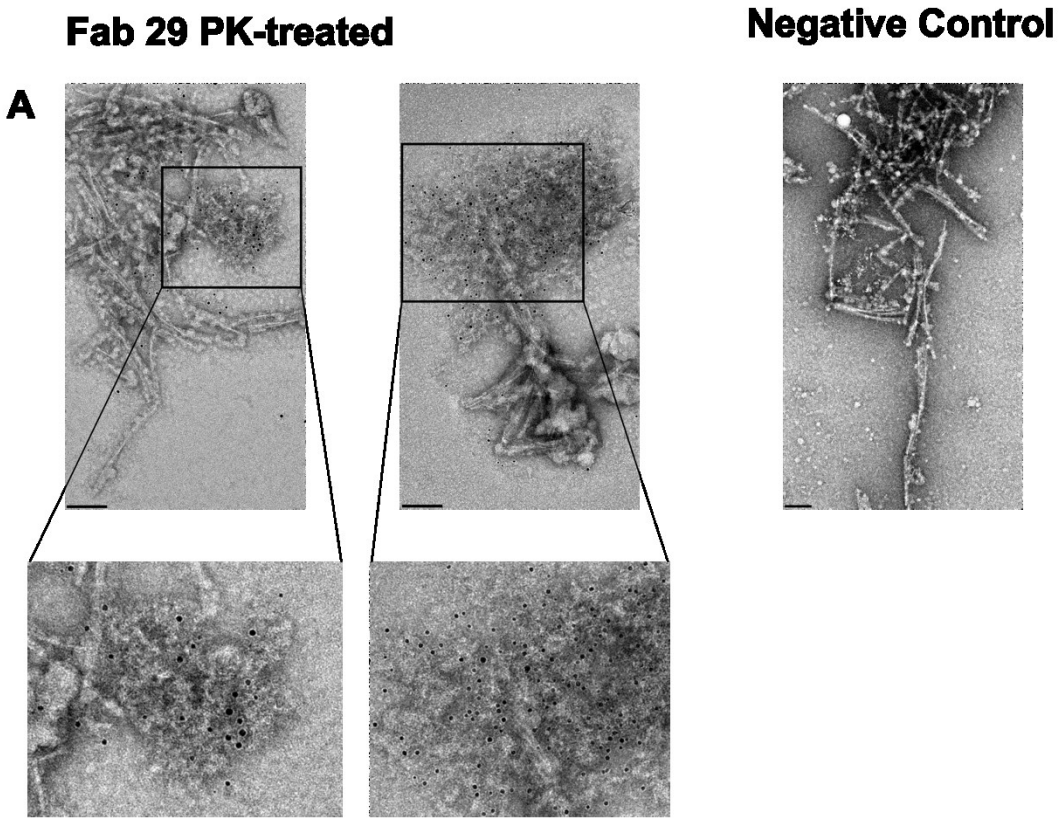
Fab 29 PK-treated
Negative Control
A
Fab 29 PE-treated
Negative Control
B

Figure 2-8. Immunogold electron microscopy of purified CWD fibrils with Fab 29. Anti-PrP Fab 29 recognizes an epitope between residues 218 and 230 at the globular domain of PrP. (**A**) Immunogold labelling of PK-treated samples with anti-PrP Fab 29. Mostly PrP aggregates are labelled with gold particles seen in the zoomed-in regions. The far-right panel shows a negative control image that had very rare gold particles. (**B**) Immunogold labelling of PE-treated samples with anti-PrP Fab 29. Mostly PrP aggregates are labelled with gold particles seen in the zoomed-in regions. The far-right panel shows a negative control image with no specific labelling. Scale bar = 100 nm.

Fab 3 targets epitopes within residues 26 to 37 of the full-length prion protein. As demonstrated in Figure 2-9A, Fab 3 was not able to detect PrP in the PK-treated sample. However, fibrils from the PE-treated sample were labelled with Fab 3 (Figure 2-9B). Interestingly, most PE-digested fibrils were only labelled at their ends (black boxes in Figure 2-9B), suggesting that the N-terminal residues are only accessible before PrP fully folds into its quaternary structure. Negative control samples for both PE- and PK-treated samples did not show any gold particles, indicating the specificity of the immunogold labelling (Figure 2-9).

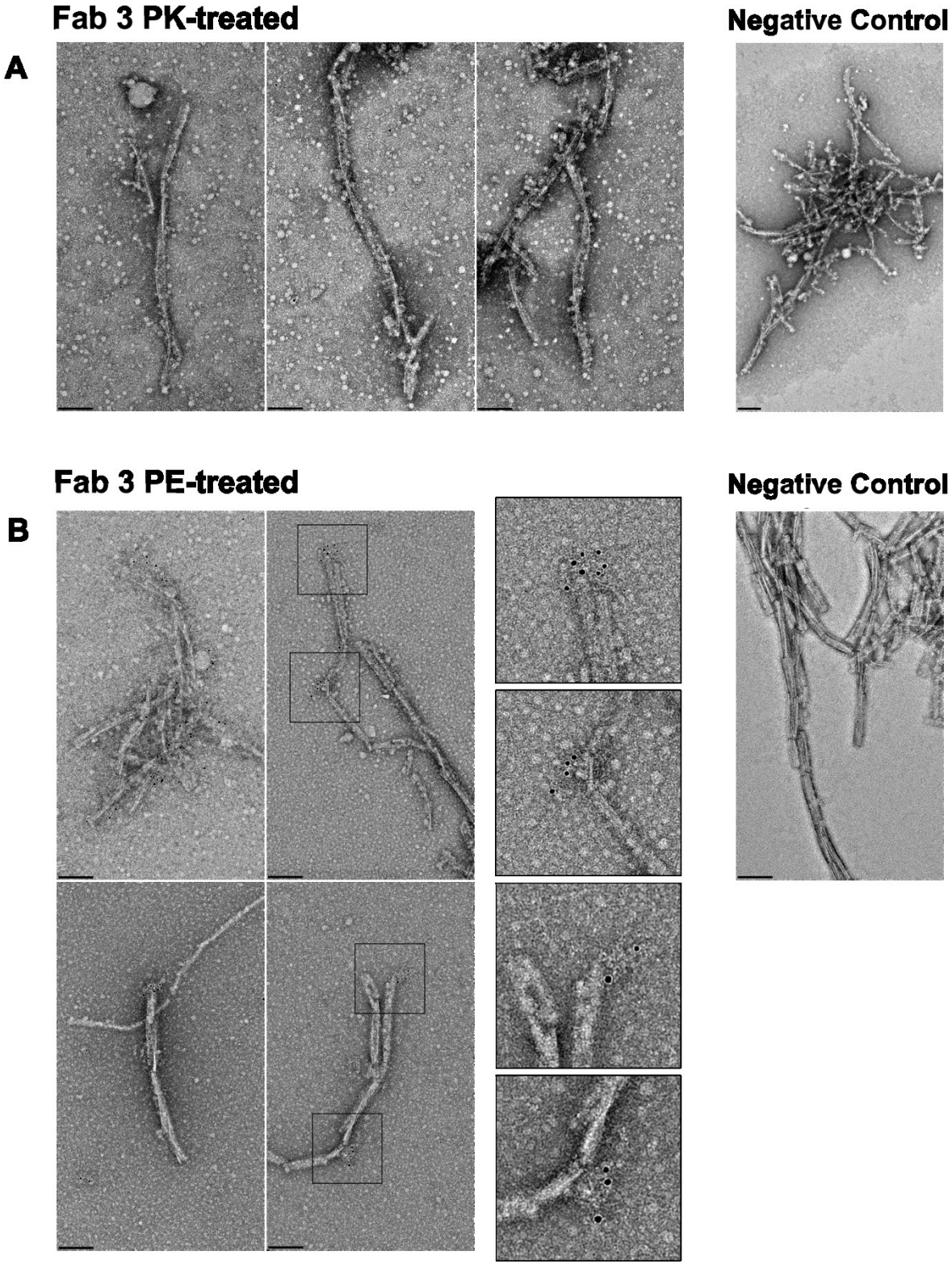
Fab 3 PK-treated
Negative Control
A
Fab 3 PE-treated
Negative Control
B

Figure 2-9. Immunogold electron microscopy of purified CWD fibrils with Fab 3. Anti-PrP Fab 3 recognizes an epitope between residues 26 and 37 of the N-terminal region of PrP. (**A**) Immunogold labelling of PK-treated samples with anti-PrP Fab 3. PK-treated samples lack the N-terminus hence very rare labelling is observed with Fab3. The far-right panel shows a negative control image that had very rare gold particles. (**B**) Immunogold labelling of PE-treated samples with anti-PrP Fab 3. PE-treated samples were labelled with Fab 3, indicating the presence of the N-terminus in these samples. Most of the fibrils had gold labelling on their ends. The areas where gold particles accumulate on the fibrils are highlighted by black boxes. These boxes have been enlarged to provide a clearer view of the 5nm gold particles. On the far-right panel, a negative control image with no specific labelling is displayed. Scale bar = 100 nm.

The recognition of PK-digested CWD fibrils by Fab 29, but not by Fab 3, confirms the absence of the N-terminal region (residues ~26 to ~93) and the presence of PrP 27-30 monomers in these fibrils. In contrast, fibrils from PE-treated samples were identified by both Fab 29 and Fab 3, indicating the presence of full-length PrP^{Sc} CWD monomers in these samples. This experiment shows that the only difference between PK- and PE-treated samples is the presence of the N-terminal region in the latter. Thus, the presence of the N-terminal region in the PE-treated sample may be responsible for the observed striations.

2.3.5 CWD prion purification from the brain of white-tailed deer

A series of purifications were conducted on a whole brain sample from a white-tailed deer, which was powdered in liquid nitrogen. The deer was from in a farm in North

Battlefield, Saskatchewan that tested positive for PrP^{Sc} in both brain and lymph nodes, despite not being in the clinical phase of CWD. These purifications aimed to investigate if the fibrils purified from the brains of CWD-positive tg33 mice are representative of the fibrils purified from the brain of CWD-positive white-tailed deer and whether the striations exist on the full-length CWD prions extracted from the latter.

In this experiment, CWD prion purification was carried out using PK without the use of EDTA. Unlike the previous purification, pellet 1 did not go through the sucrose step gradient, and instead, a second round of PTA purification was performed. This was done due to the lower number of fibrils seen in pellet 1 in WTD compared to the tg33 mice brain. The second round of PTA purification resulted in a higher yield of the CWD prion, as shown by a stronger Western blot signal for the final pellet compared to pellet 1 in Figure 2-10A. In Figure 2-10B, images of fibrils observed in both pellet 1 and the final pellet are shown, revealing several morphologies, including a ribbon-like conformation that is depicted in the first image of Figure 2-10B. Interestingly, 3D reconstruction of the ribbon-like conformation of the WTD prion fibril was similar to the CWD-positive tg33 mice brain fibrils, suggesting a similarity in the fibrils purified from the two different sources (supplementary Figure 2-2). Fast FT calculation did not detect any repeating units, such as striations in the purified fibrils (Figure 2-10C). The results suggest that the fibrils purified from CWD-positive tg33 mice brains do reflect some of the morphologies seen in the brain of white-tailed deer.

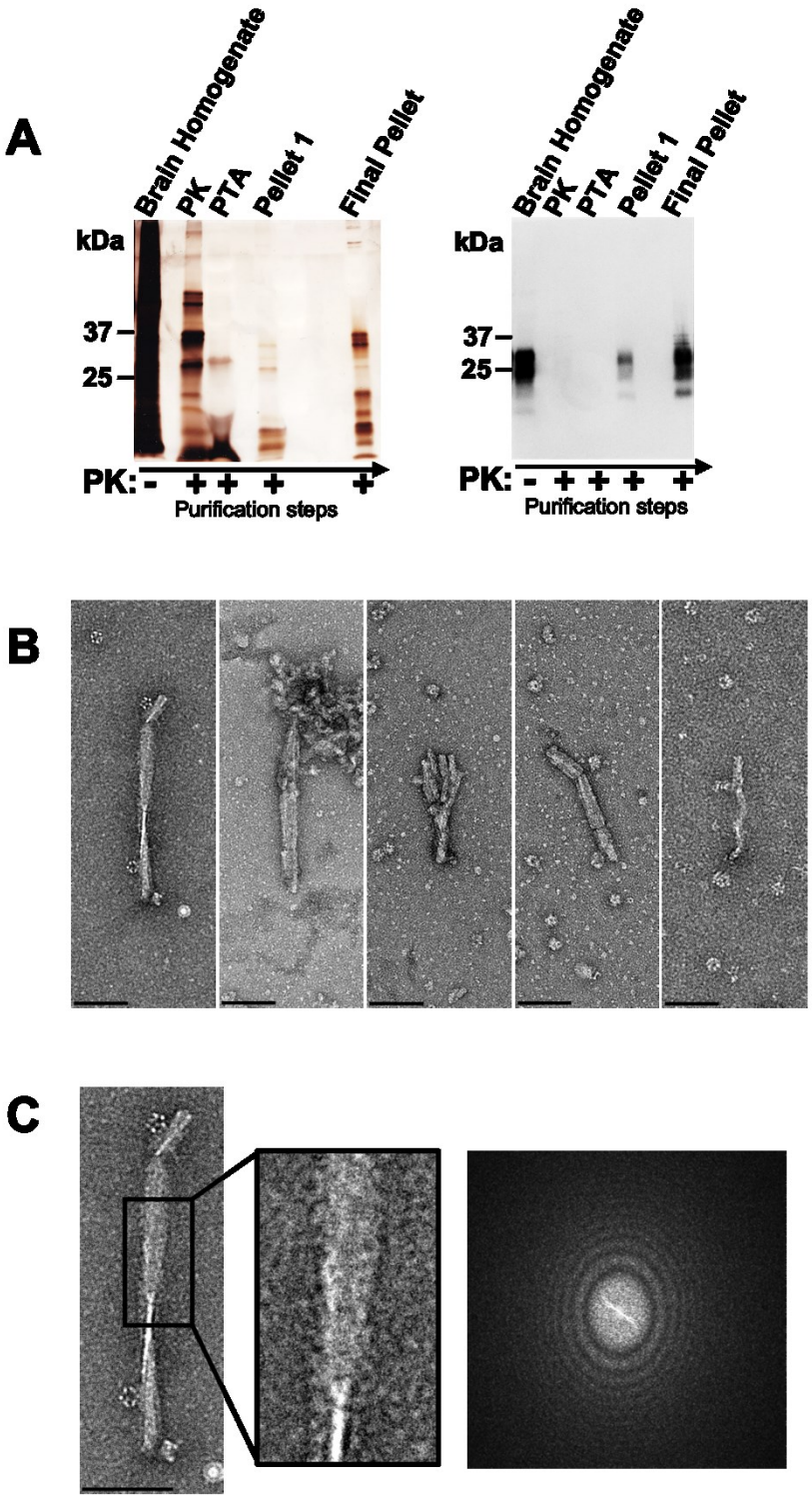

Figure 2-10. Purification of CWD prions from the brain of CWD-positive white-tailed deer using PK. (**A**) Silver stain SDS-PAGE and *W*estern blot of samples taken

from different steps of the purification. The Western blots were developed using the D15.15 anti-PrP monoclonal antibody. (**B**) Gallery of negatively stained electron micrographs of N-terminally truncated PK-treated CWD fibrils purified in the absence of EDTA. Scale bar = 100 nm. (**C**) A zoomed-in view of a negatively stained micrograph demonstrating no striation and no peaks on its diffraction pattern.

Another set of purification experiments using PE and EDTA was performed on the CWD-positive WTD brain samples. Figure 2-11A displays the silver stain and *W*estern blot for this purification. Contrary to the PK purification experiment, the CWD prion signal was not amplified by two rounds of PTA purification (Figure 2-11A). However, both pellet 1 and the final pellet had CWD fibrils (Figure 2-11B). Interestingly, fast FT calculations on CWD fibrils purified using PE revealed peaks on the diffraction pattern corresponding to striation with a spacing of 3.7 nm.

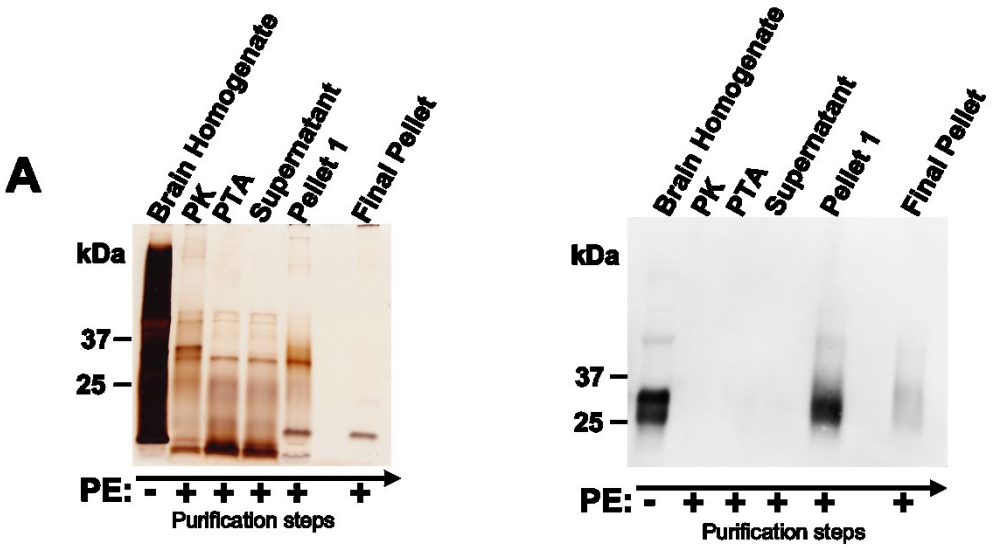
A
Brain Homogenate
PK
PTA
Supernatant
Pellet 1
Final Pellet
kDa
37
25
PE: - + + + + +
Purification steps
Brain Homogenate
PK
PTA
Supernatant
Pellet 1
Final Pellet
kDa
37
25
PE: - + + + + +
Purification steps

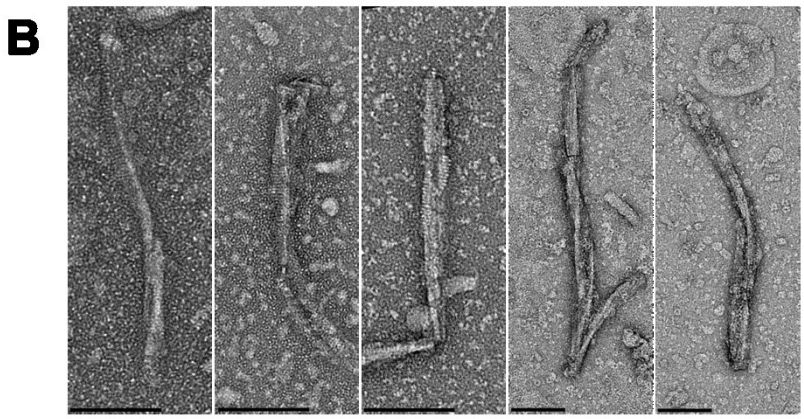
B

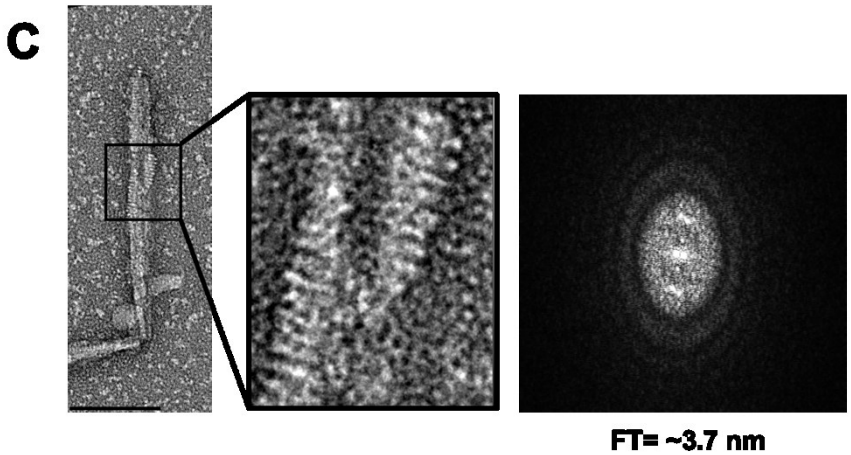
C
FT= ~3.7 nm

Figure 2-11. Purification of CWD prions from the brain of CWD-positive white-tailed deer using PE. (A) Silver stain SDS-PAGE and *W*estern blot of samples taken from different steps of the purification. The Western blots were developed using the D15.15 anti-PrP monoclonal antibody. (**B**) Gallery of negatively stained electron micrographs of full-length PE-treated CWD fibrils purified in the presence of EDTA. Scale bar = 100 nm. (**C**) A zoomed-in view of a negatively stained micrograph demonstrating striation and its representative diffraction pattern. The recurrence of the striations creates peaks on the diffraction pattern, which aids in determining the spacing of the striations, which is around 3.7 nm.

2.4 DISCUSSION

Despite numerous studies on the structure of recombinant and tissue-derived prion strains, knowledge about the structural properties of chronic wasting disease prions are limited, and data on the full-length, brain-derived infectious prion protein is unavailable. This study used electron microscopy to examine the full-length and N-terminally truncated structure of CWD prions purified from the brains of CWD-positive Tg33 mice and white-tailed deer. This was achieved by using either proteinase K to generate N-terminally truncated PrP or Pronase E to produce full-length PrP. Clinical prion disease symptoms were developed when the purified samples were intracerebrally injected into Tg33 mice, demonstrating that both the full-length and N-terminally truncated forms of CWD prions retain their infectious properties and can transform normal PrP into their aberrant disease-causing conformer.

Upon examination of the purified CWD prions through transmission electron microscopy, the fibrils were found to be morphologically heterogeneous (Figure 2-2). Unlike previously studied brain-derived scrapie (Kraus et al. 2021, Manka et al. 2022), and BSE prion fibrils (Kamali-Jamil et al. 2021) with a maximum width of 10 to 20 nm, the majority of CWD prion fibrils were thicker, with a diameter of approximately 35 nm (Figure 2-3). The study also revealed that infectious full-length CWD prions displayed striations with a spacing of 3.3 to 3.5 nm (in CWD positive tg33 mice) and 3.7 nm (in CWD positive white-tailed deer) that were absent in the N-terminally truncated form, indicating that these striations correspond to the N-terminal region of the prion protein (Figure 2-4 to 2-6). The presence of ordered striations on the full-length form of CWD prions was observed to be enhanced with the utilization of EDTA, a chelator, in the purification procedure, as depicted in Figure 2-4 and 2-5. Previous studies have indicated that copper ions have an interaction with the N-terminal region (octapeptide repeat region) of PrP and have an impact on the conformations of both PrP^{C} and PrP^{Sc}. Consequently, the removal of these cations by EDTA could result in changes to the structural conformation, influencing the appearance of the N-terminus (striations). No fibrils decorated with ordered striations were observed in the N-terminally truncated form of prions generated using proteinase K, whether EDTA was used or not, as demonstrated in Figure 2-6. The presence of the N-terminus in the samples treated with Pronase E was confirmed through immunogold labelling targeting the N-terminal region of the prion protein (Figure 2-9).

To date, two distinct structural models for protein aggregation have been proposed: the parallel in-register intermolecular β-sheet structure (Kraus et al. 2021, Hoyt et al. 2022, Hoyt et al. 2022, Manka et al. 2022, Manka et al. 2023) and the 4-rung beta solenoid model (Wille et al. 2009, Vázquez-Fernández et al. 2016, Spagnolli et al. 2019). The 4RβS model was initially established based on X-ray fibre diffraction analysis of PrP 27-30 amyloid fibrils (Wille et al. 2009) and further validated by low-resolution cryo electron microscopy studies of brain-derived and GPI anchorless mouse prion fibrils (Vázquez-Fernández et al. 2016), as well as negatively stained imaging of brain-derived BSE prion fibrils (Kamali-Jamil et al. 2021). These studies demonstrated repeating structural features along the fibril axis with a spacing of 19.2 Å and a spacing of 4.9 Å between β-sheet strands. On the other hand, the PIRIBS model was established through high-resolution cryo EM studies of the brain-derived infectious prion protein, which showed monomers stacking in-register with a height of 4.9 Å per prion molecule (Kraus et al. 2021, Hoyt et al. 2022, Hoyt et al. 2022, Manka et al. 2022, Manka et al. 2023). Both the 4RβS and PIRIBS models were proposed for N-terminally truncated PrP, lacking residues ~26 to ~93. As such, the interpretation of observations relating to the spacing of striations formed by the N-terminus may pose challenges. However, if the N-terminus is assumed to be present in these models, the head-to-head/tail-to-tail stacking of monomers in the 4RBS model results in a spacing of 3.8 nm for the N-terminus, which is in close agreement with the observed spacing of 3.3 to 3.7 nm of the striations in this study (as depicted in Figure 2-12A). The hypothetical spacing of the N-terminus in a PIRIBS structure is 4.9 Å, which differs significantly from the observed striation spacing of 3.3 to 3.7 nm

in this study. The observed spacing aligns with the spacing of every 8 monomers in a PIRIBS structure. (Figure 2-12B).

The observation of thinner and less abundant 23-25 nm CWD fibrils in PE-purified samples led to the assumption that they consist of a single protofilament. As a result, a comparison was made by superimposing their helical reconstruction onto the high-resolution PIRIBS structure of the 263K strain, which consists of a single protofilament with a width of 13 nm. Despite the presence of unstained and N-terminal-deficient one protofilament 263K fibrils, which could contribute to the discrepancy in width, the thin CWD fibril and the PIRIBS structure display topological similarity (supplementary Figure 2-3). The striations were not detected on full-length thin CWD prion fibrils. Instead, these striations were only visible on thicker fibrils measuring 35 nm. The complexity of the structure is increased due to the presence of multiple protofilaments and a diverse glycosylation pattern in these thicker fibrils, making it challenging to decipher the arrangement of the N-terminus.

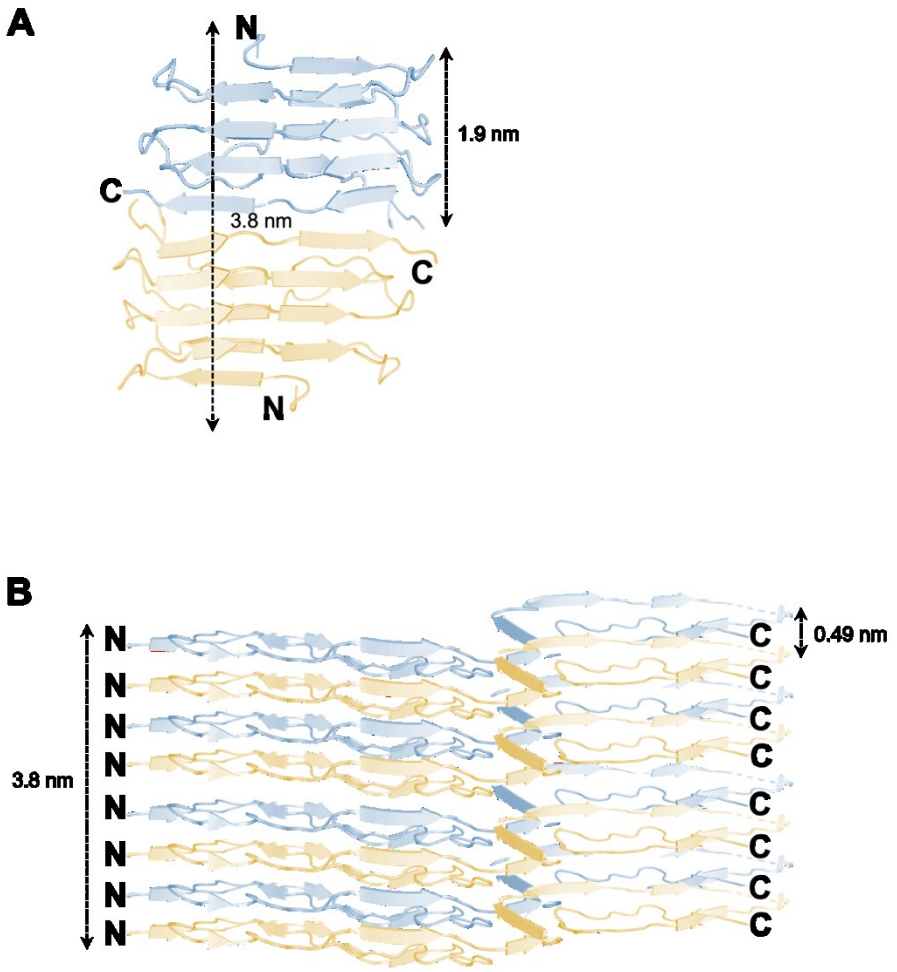

Figure 2-12. 4RβS model and PRIBS structure of infectious prion protein. (**A**) 4RβS model adapted from Spagnolli et al.(2019) illustrating the head-to-head / tail-to-tail stacking of PrP^{Sc}. The letters N and C denote the location of the N-terminal and C-terminal, respectively. In the 4RβS model, the height of each monomer is 19.2 Å. In this conformation, the distance between two N-terminus is 3.8 nm. (**B**) PIRIBS structure adapted from Kraus et al.(2021) for the N-terminally truncated 263K prions (PDB: 7lna). The N- and C- terminus locations are shown with the letters N and C. In the PIRIBS structure, the height of each monomer is 4.9 Å.

In conclusion, this study marks the first observation of brain-derived, infectious Chronic Wasting Disease prions. The findings offer new insights into the quaternary

structure of CWD amyloid fibrils and provide the initial report on the detection of the N-terminus structure of these infectious prions. Elucidating the structure of the N-terminal region could be significant in comprehending the pathogenic processes of prion diseases. Additionally, investigating the strain-specific features of CWD prions may improve our understanding of the species barrier and facilitate the development of prion vaccines in the event of a potential zoonotic outbreak of CWD.

2.5 SUPPLEMENTARY FIGURES

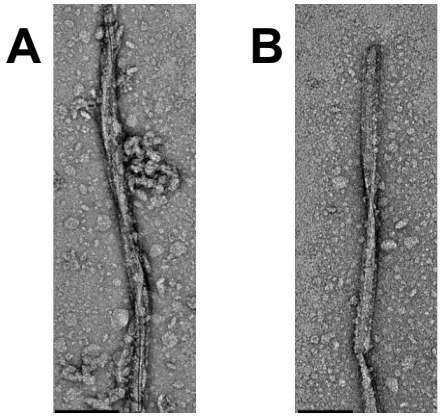

Supplementary Figure 2-1. Negatively stained micrographs of pellet 1 PE- and PK-purified samples. (**A**) Negatively stained micrographs of pellet1 fibrils purified using PE. The sample displays a very crowded background that requires future purification steps. (**B**) Negatively stained micrographs of pellet 1 fibrils purified using PK. The background appears clean and does not require further purification. However, to keep the purification steps consistent with PE-purified samples, a sucrose step gradient purification was also performed on these samples.

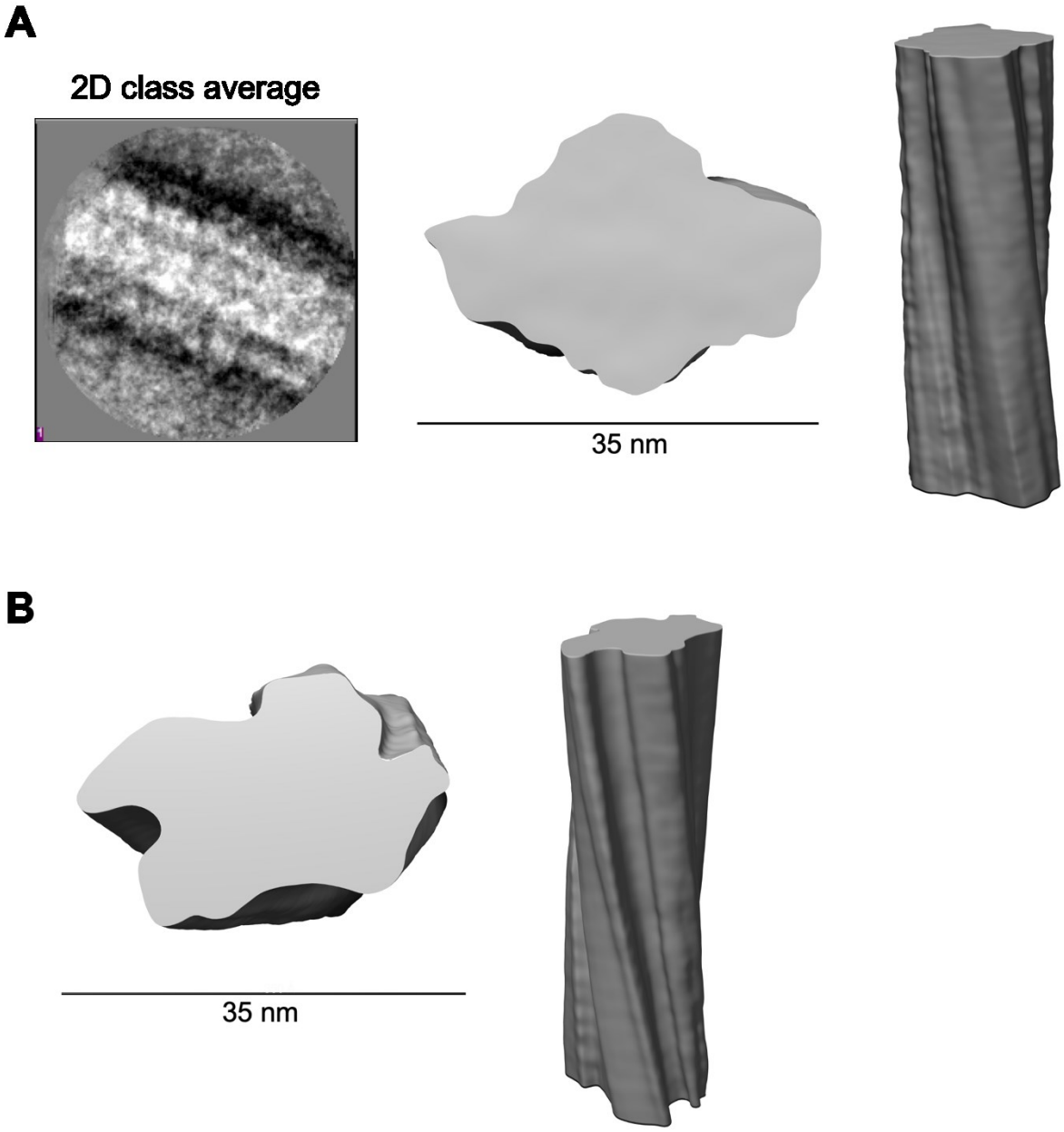

Supplementary Figure 2-2. The helical reconstruction of ribbon-like fibrils purified from CWD-positive tg33 and WTD brain. (**A**) An image of a 2D class average of ribbon-like fibrils, which were extracted from the brain tissue of CWD-positive tg33 mice using Pronase E, shows a hemispherical shape on the surface of the fibrils. The second image is a cross-sectional image of the helical reconstruction of the fibril, with a width of 35 nm, which also exhibits a hemispherical shape. The third image presents a side view of the 3D reconstruction. (**B**) The cross-section and

side view of the helical reconstruction of ribbon-like fibrils obtained from the brain of CWD-positive white-tailed deer using Pronase E display a similar hemispherical shape

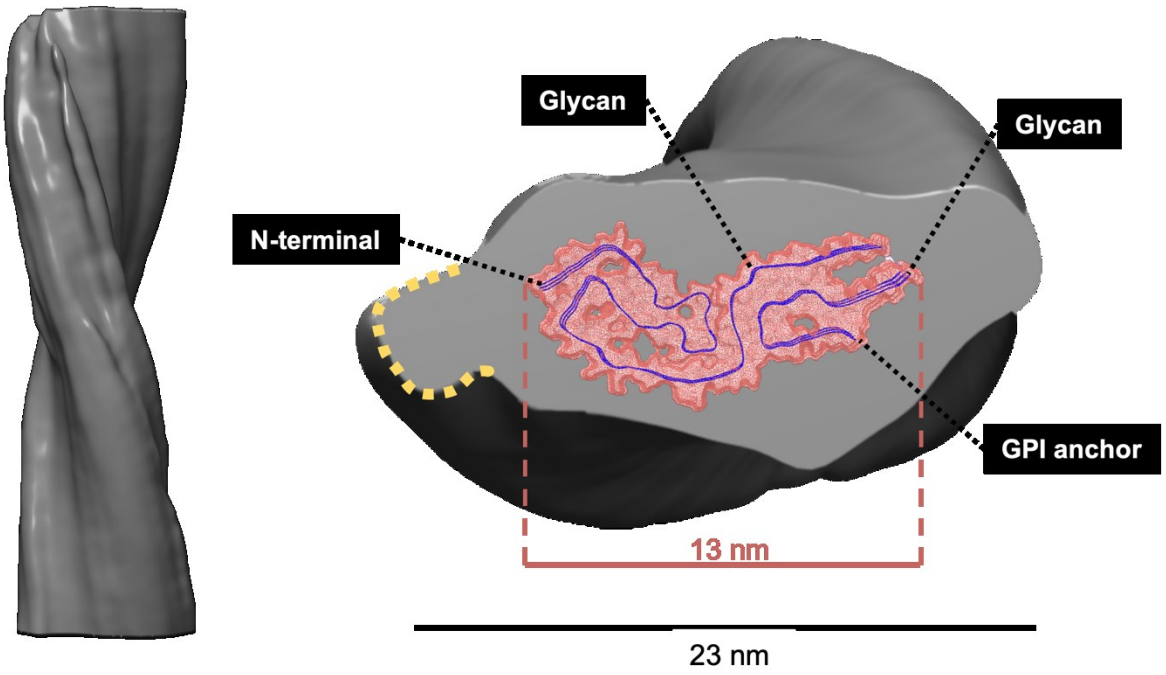

Supplementary Figure 2-3. Superimpose of the CWD fibrils and the PIRIBS structure. Side view and cross-section of the helical reconstruction of thinner fibrils, referred to as Morphology III, that were detected in the full-length PE-treated samples extracted from the brain tissue of CWD-positive tg33 mice. The PIRIBS structure of *ex-vivo* 263K scrapie fibrils (PDB: 7lna) (Kraus et al. 2021) is superimposed on the cross-sectional image of the CWD prion fibril. The PIRIBS structure is labelled to indicate the position of the N-terminus, glycans, and GPI anchor. The yellow dotted line highlights the location of the N-terminus on the CWD prion fibril's 3D reconstruction.

Chapter 3: Analyses of cervid prion protein variants 95H, 96S, and 116G to assess protein stability and susceptibility toward CWD

3.1 INTRODUCTION

The prion protein (PrP) is composed of approximately 210 residues in its mature form (Riek et al. 1996, Colby and Prusiner 2011). It is a glycosyl-phosphatidylinositol (GPI) anchored glycoprotein located on the cell surface, primarily expressed in neuronal cells (Aguzzi et al. 2008, Colby and Prusiner 2011). The N-terminal domain of the normal cellular form prion protein (PrP^C) is predominantly unstructured, while the C-terminal domain exhibits well-defined secondary and tertiary structures, comprising three α-helices and two β-strands (Riek et al. 1996) (Figure 3-1). A disulfide bond forms between Cys182 and Cys217 (all numbers are cervid numbering), and there are two N-linked glycosylation sites at residues Asn184 and Asn200. Although the physiological function of PrP^C is not fully understood (Aguzzi et al. 2008), its conversion from the normal cellular form to a misfolded, oligomeric isoform (PrP^{Sc}) leads to a group of diseases referred to as prion diseases or Transmissible Spongiform Encephalopathies (TSE). These neurodegenerative disorders, such as Creutzfeldt-Jakob disease in humans, Chronic Wasting Disease (CWD) in cervids, Scrapie in sheep, Bovine Spongiform Encephalopathy in cattle, and transmissible mink encephalopathy in mink, are prevalent and invariably fatal, lacking any known treatment (Colby and Prusiner 2011).

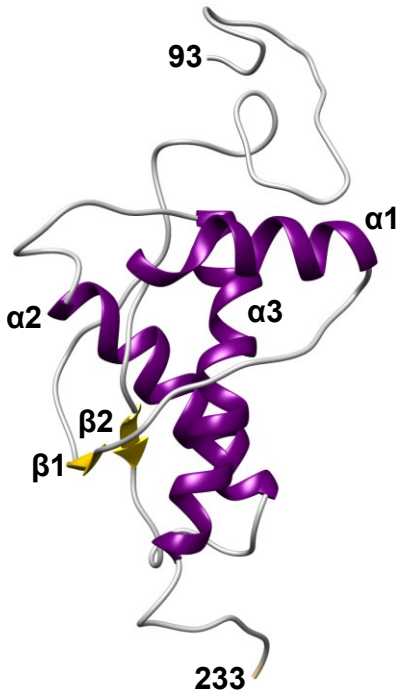

Figure 3-1. Ribbon diagram representation of white-tailed deer PrP (residues 93 to 233). α1, α2 and α3 stand for helix one, two, and three, respectively. β1 and β2 stand for β-strands one and two. The coordinates for residues 124 to 231 were obtained from the PDB ID: 4yxh (Baral et al. 2015).

Chronic wasting disease has now spread to wild mule deer, white-tailed deer (WTD), elk, reindeer, and moose in different regions of the world, including 4 Canadian provinces, 30 American states, South Korea, Norway, Finland, and Sweden (Arifin et al. 2021, Otero et al. 2021, Tranulis et al. 2021, Otero et al. 2023).

Although the prion protein gene (*Prnp*) is conserved among cervid species, numerous well-studied polymorphisms have been identified that influence susceptibility to prion

diseases (Johnson et al. 2003, O'Rourke et al. 2004, Johnson et al. 2006). Substitution of glutamine (Q) with histidine (H) at position 95 (Johnson et al. 2003, Haley et al. 2016), glycine (g) with serine (S) at position 96 (Johnson et al. 2003, O'Rourke et al. 2004, Johnson et al. 2011), and alanine (A) with glycine at position 116 (O'Rourke et al. 2004, Hannaoui et al. 2017, Haley et al. 2019) are three well-characterized white-tailed deer polymorphisms that are associated with reduced susceptibility to CWD and/or delay disease progression.

Genetic analyses of various cervid populations demonstrate that *Prnp* variability (polymorphisms) can affect disease progression and susceptibility (Johnson et al. 2006, Meade-White et al. 2007, Johnson et al. 2011, Race et al. 2011, Robinson et al. 2012, Arifin et al. 2021). However, due to the limited number of polymorphisms studied using *in-silico* and experimental methods, the question of how these genetic variations affect prion protein folding remains unanswered.

In this study, all-atom molecular dynamics simulations were employed to examine the protein structure of white-tailed deer PrP93-233 encompassing the wild type (WT) sequence and structural models incorporating three polymorphisms: 95H, 96S, and 116G. Various analytical tools were used to investigate specific structural and dynamical alterations associated with each polymorphism and compared the findings with those of the wild type protein. These tools allow the evaluation of atomic-level structural details that are difficult or impossible to study otherwise. A total of 600 ns of

molecular dynamics (MD) simulations were performed. Using real-time quaking-induced conversion (RT-QuIC) assay, we also evaluated the effect of these polymorphisms on the aggregation propensity of recombinant deer PrP.

3.2 MATERIAL AND METHODS

3.2.1 Building the molecular structures

The GPI anchor cleavage site is not experimentally identified in the Cervidae family. To computationally identify this site, the protein sequence of wild type WTD provided by Hannaoui et al. (Hannaoui et al. 2017) was used and employed in an online software tool named Big-PI Predictor (Eisenhaber et al. 1998, Eisenhaber et al. 1999, Eisenhaber et al. 2000), to identify the most probable GPI modification site. The result suggests that alanine at position 233 is most probably the cleavage site in the white-tailed deer sequence with a P-Value of 2.86e-05 (Supplementary Figure 3-1). Thus, the amino acid sequence used for running the simulations is from residue 93 to the GPI anchor cleavage site residue 233.

The initial three-dimensional (3D) model for white-tailed deer PrP sequence 124 to 231 was built using the SWISS-MODEL homology modelling server (Arnold et al. 2006) based on the 4yxh.pdb (Baral et al. 2015) template. SWISS-MODEL template search, based on the SWISS-MODEL template library (SMTL) derived from the Worldwide Protein Data Bank www.pdb.org structures, produced a total of 201 templates. The crystal structure of deer prion protein with PDB code: 4yxh (Baral et

al. 2015), model 1, chain A was chosen as the best template with a sequence identity of 99.01%, GMQE (Global Model Quality Estimation) score of 0.78, and a QMEAN4 score of -0.10 (Supplementary Figure 3-2).

Since the deer prion protein crystal structure 4yxh.pdb (Baral et al. 2015) lacks the N-terminal sequence "WG**HS**GTHSQWNKPSKPKTNMKHV**G**GAAAAGA", including the site of the 95H, 96S, and 116G polymorphisms (in bold), and two C-terminal residues "GA", the subsequent model built by SWISS-MODEL also lacked these residues. Thus Biovia Discovery Studio software (BIOVIA 2017) was used to build the missing residues and include the polymorphisms as needed.

3.2.2 Molecular dynamics simulations

Minimizations, equilibrations, and production MD simulations of all structures (WT, 95H, 96S, and 116G) were performed using the Gromacs version 4.6.7 (Berendsen et al. 1995, Hess et al. 2014). For the protein description, the OPLS (Optimized Potential for Liquid Simulation) forcefield (Jorgensen et al. 1996) was used. After the structure preparations, an energy minimization by steepest descent was used to minimize each system's energy. Protein structures were solvated with a simple point charge extended (SPC/E) rectangular periodic water box, and to ensure that the system is electro-neutralized, Cl^- or Na^+ ions were added as appropriate. Subsequently, energy minimizations with decreasing restraints on non-hydrogen protein atoms (K_{posre} = 1×10^5, 1×10^4, 1000, 100, 10, and 0 kJ mol^{-1} nm^{-2}) were made

to first adjust the solvent around the protein, then to adjust the protein in solution. Heating to 310K (Berendsen thermostat) and isotropic temperature coupling (NVT) equilibration to adjust the solvent density to 1 g/cm3 followed the minimizations. To ensure consistency and reproducibility of the results, three separate MD simulations of 50 ns were performed for all equilibrated systems.

3.2.3 Post-analysis tools

The MD trajectory files were analyzed using several different programs. The g_gyrate, g_rmsd, and g_rmsf scripts of GROMACS (Berendsen et al. 1995) were used to obtain the radius of gyration (Rgs), root-mean-square deviation (RMSDs), and root-mean-square fluctuation (RMSFs) for the Cα atoms. The RMSD values were only calculated for the structured area of the prion protein (residue 127 to 233). The two-dimensional (2D) contour map from the last 15 ns of the RMSD and Rg values was plotted using Plotly Chart Studio, an online graph maker (https://plotly.com/chart-studio/) and the PDB files that were extracted from the 2D contour map peaks were visualized using Chimera (Pettersen et al. 2004). Using scripts implemented in the Visual Molecular Dynamics software (VMD) (Humphrey et al. 1996), the total solvent accessible surface, hydrophobic, and hydrophilic surface areas were calculated. VMD was also used to assign the secondary structure elements. The g_hbond GROMACS script was used to calculate the hydrogen bonds for the last 15 ns of the simulations. Only hydrogen bonds with an angle of ≤ 30° and a donor-acceptor distance <3.5 Å were taken into account. Salt bridges (SB) were calculated using the salt bridges plugin of VMD with a cut-off distance of 3.2 Å between the center of mass of the

nitrogen atom in the basic side chain and the center of mass of the oxygen atom in the acidic side chain. Distance maps were generated using the g_mdmat program of GROMACS and using the xpm2ps program; the output files were processed to create the final plots. Difference maps were generated from the subtraction of WT PrP from the polymorphisms' distance maps. The cumulative final 15 ns trajectories (.xtc files) were calculated and used as input for the averaged salt bridge and distance map calculations. Initially, trajectories (.xtc files) were calculated for the final 15 ns of the simulation for all protein variants (WT, 95H, 96S, and 116G for rounds one, two, and three) using the tjrconv GROMACS program. Next, the trjcat GROMACS script was used to combine the trajectories for R1, R2, and R3 of the simulations of each protein variant. As a result, each protein variant was represented by trajectory (.xtc file) - the combination of the final 15 ns of its R1, R2, and R3 simulation.

3.2.4 Real-time quaking-induced conversion assay

Recombinant deer PrP was expressed and purified as previously described (Cortez et al. 2013). Lyophilized recombinant PrP was dissolved in 6M guanidine hydrochloride at a protein concentration of 5 mg/ml and stored at -80 ºC. Recombinant deer PrP protein in 6M guanidine hydrochloride was diluted in RT-QuIC buffer (20 mM sodium phosphate pH 7.4; 130 mM NaCl; 10 mM EDTA; 0.002% SDS) to a final protein concentration of 0.2 mg/mL, and residual 0.2 M guanidine hydrochloride. The aggregation reactions were carried out in 96-well plates (white plate, clear bottom; Costar 3610) sealed with thermal adhesive film (08-408-240; Fisherbrand). The samples were incubated in the presence of 10 mM thioflavin T at 42°C with cycles of 1 min shaking (700 rpm double orbital) and 1 min rest. Thioflavin

T fluorescence measurements (450+/210 nm excitation and 480+/210 nm emission; bottom read) were collected every 60 minutes.

3.3 RESULTS

The time-dependent positions and velocities of atoms obtained from molecular dynamics trajectories can provide valuable insights. However, understanding the structural impact of each construct requires post-simulation data processing and interpretation. A multitude of parameters can be extracted from these trajectories, including investigations into the structure's stability and compactness, exploration of residue flexibility and fluctuations, assessment of surface accessibility, probing of intermolecular interactions, and analysis of secondary structure elements. Below, we will examine a range of parameters for each construct and compare them to the wild type. This will allow us to better understands how the constructs carrying the polymorphisms influence the structure of the prion protein.

To calculate the structural deviations of the ordered C-terminal domain of PrP, the Cα root mean square deviation of residues 127-233 was measured for all simulations (Figure 3-2A). The Cα RMSD presents the backbone structural deviation from the white-tailed deer PrP structure that was used as the starting point for the MD simulations. The RMSD values of all simulations attained a stable state within approximately 35 ns of simulation time, facilitating the examination of the steady-state structures during the final 15 ns of each simulation (red box, Figure 3-2A). The mean RMSD value for the last 15 ns of the wild type PrP simulation is 0.22 nm, with a

standard deviation of 0.04 nm, indicating minimal deviations from the starting structure. 95H, 96S, and 116G polymorphism simulations reached higher Cα RMSDs of 0.32 nm, 0.30 nm, and 0.31 nm, respectively. Elevated RMSD values observed in the polymorphisms indicate that the amino acid substitutions have induced greater structural changes compared to the WT PrP structure.

Figure 3-2B illustrates the radius of gyration, which serves as a measure of the structural compactness during a 50 ns simulation. The Rg values for WT PrP, 96S, and 116G are highly comparable while being lower for 95H. This suggests that the 95H polymorphism has altered the structure of PrP to become more compact. To gain a deeper understanding of the dynamic relationship between RMSD and Rg, as well as the various conformations present in the MD simulations, a 2D contour map incorporating both parameters was generated and depicted in Figure 3-2C. Within each plot of Figure 3-2C, there are a total of 150,000 data points, corresponding to the averaged Rg versus RMSD values obtained from three rounds of simulations conducted for both the polymorphisms and WT PrP. Notably, the data points corresponding to each system were found to cluster within distinct regions in the 2D plot. This observation suggests the presence of unique subgroups of conformations in 95H, 96S, and 116G, which are distinct from one another and the WT PrP. The arrows in Figure 3-2C indicate the peaks corresponding to the Rg and RMSD values, which represent the most dominant and stable conformations for each protein variant.

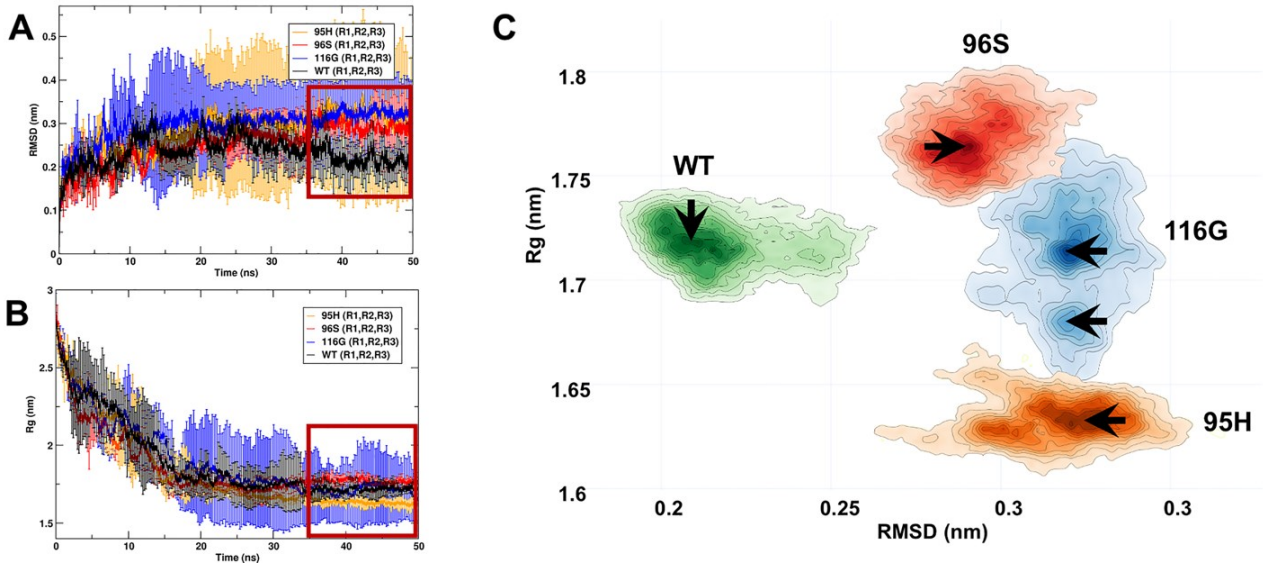

Figure 3-2. RMSD and Rg, and a 2D contour map for WT PrP and the 95H, 96S, and 116G polymorphisms. (**A**) RMSD plot for the folded domains (residue 127-233) of 95H (orange), 96S (red), 116G (blue), as well as WT PrP (black) as a function of simulation time. All graphs show the average of three rounds of simulation (R1, R2, R3). The final 15 ns of simulation representing the steady state are indicated by a red box. (**B**) The radius of gyration values for 95H (orange), 96S (red), 116G (blue) and WT (black) as a function of simulation time. All graphs are the average of three rounds of simulation (R1, R2, R3). The final 15 ns of simulation are indicated by a red box. (**C**) A two-dimensional contour map representing the Rg versus RMSD values. The plot for each protein variant (95H in orange, 96S in red, 116G in blue, and WT in green) contains 150,000 data points, again representing the average of three rounds of simulation (R1, R2, R3). The arrows pointing at the peaks of each data cloud represent the most dominant conformation for each protein variant.

To identify the specific conformations associated with these peaks, we extracted the precise nanoseconds during the simulations where the Rg and RMSD values corresponded to the X and Y coordinates of the respective peaks. c (Pettersen et al. 2004) (Figure 3-3). The dotted ovals in Figure 3-3 indicate the specific regions where

notable distinctions were observed among the 95H, 96S, 116G, and WT PrP polymorphisms. Comparing these structural snapshots facilitates the comprehension and visualization of the distinct conformational impacts imposed by each polymorphism on the PrP structure. Specifically, the 95H polymorphism exhibits a more tightly ordered structure compared to WT PrP, whereas the 96S and 116G polymorphisms demonstrate comparatively lower levels of structural order and compactness (highlighted within the dotted ovals in Figure 3-3).

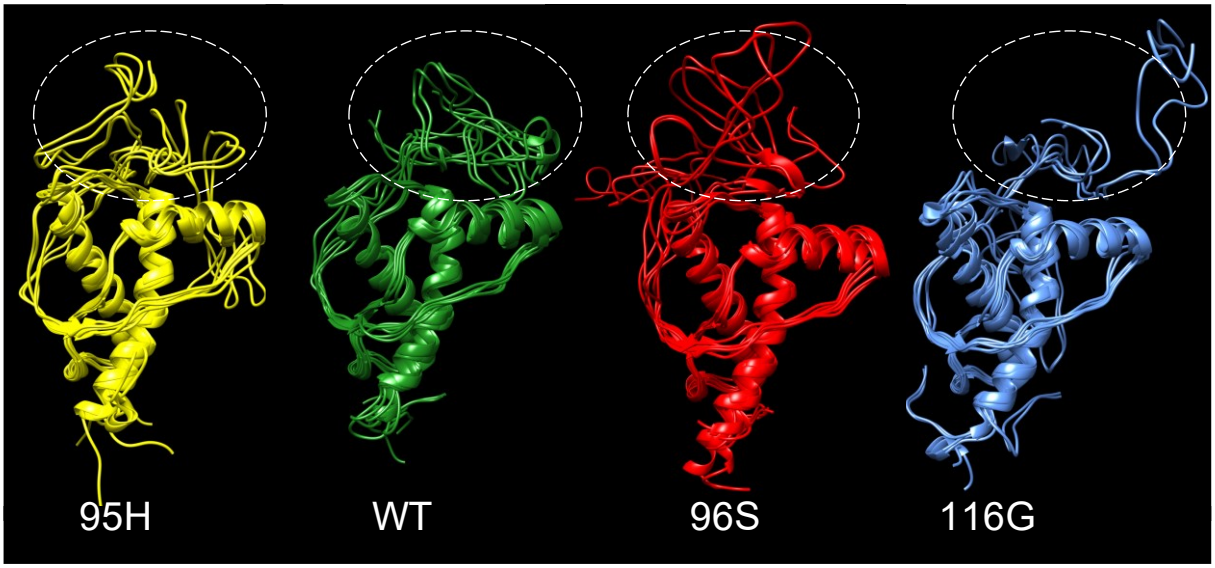

Figure 3-3. Snapshots of frequently observed conformations for WT PrP and the polymorphic variants. The snapshots were drawn from each round of simulation (R1, R2, R3), indicating highly populated conformations (see black arrows in Figure *3*-2C), superimposed, and visualized using the Chimera software. Snapshots for 95H are shown in yellow, 96S in red, 116G in blue, and WT in green. Dotted ovals highlight where the most significant differences were seen amongst 95H, 96S, 116G, and WT PrP.

To analyze the backbone standard deviation for each residue, the Cα root means square fluctuations were plotted (Figure 3-4). Each RMSF graph is the average of three rounds of simulations (R1, R2, and R3) and is calculated for the final 15 ns of the simulations. The secondary structure elements, denoted as **β**1, **α**1, **β**2, **α**2, and **α**3 (where β represents β-strands and α represents α-helices), exhibit lower RMSF values in comparison to the more flexible loop regions. Both the 96S and 116G polymorphisms exhibit elevated RMSF values in comparison to WT PrP (as shown in Figure 3-4, represented by the red and blue graphs, respectively). These increased fluctuations observed in 96S and 116G lead to less ordered structures, as shown in Figure 3-3 by the red and blue structures. In contrast, the 95H polymorphism induces a reduction in the flexibility of the PrP structure, as evidenced by decreased fluctuations in nearly every residue (represented by the orange graph in Figure 3-4), resulting in a well-organized conformation (yellow structure in Figure 3-3).

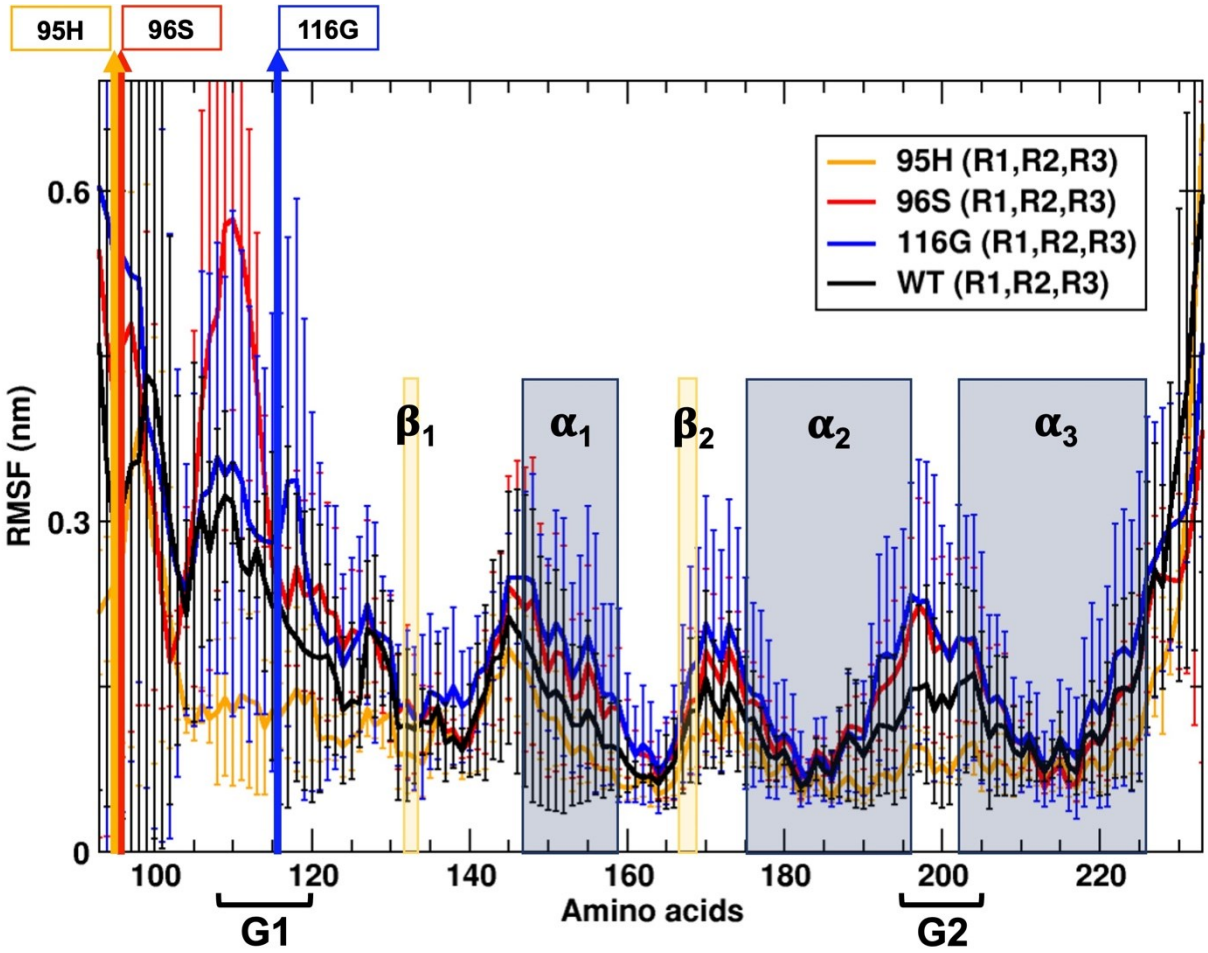

Figure 3-4. RMSF plot comparing WT PrP (black) versus the 95H (orange), 96S (red), and 116G (blue) polymorphisms. The location of the polymorphisms at residues 95, 96, and 116 are shown with orange, red, and blue lines, and labels, respectively. The yellow and grey bars highlight the location of individual β-strands and the α-helices, respectively. Each graph shows the average of three rounds of simulation (R1, R2, R3) and is calculated for the final 15 ns of the simulations. Two groups of residues labelled with G1 (residues Lys107 -Ala120) and G2 (Thr194 to Thr204) show two regions with significant fluctuation differences amongst the polymorphic variants.

To investigate the impact of amino acid substitutions in the polymorphisms on the structural correlation between residues in the protein, distance maps were constructed (Supplementary Figure 3-3). These distance maps, also known as correlation maps, depict the distances between pairs of residues in their tertiary structure as a function of time. Differences seen between the correlation maps of 95H, 96S, and 116G versus WT PrP demonstrate that the polymorphisms greatly alter the distances between the many residues within the respective protein (black arrowheads in Supplementary Figure 3-3).

The flexibility of the main chain (RMSF, Figure 3-4) is strongly correlated with the pairwise residue interactions. When residues are distant from each other, the bonds and interactions between them are weakened, leading to increased flexibility and fluctuations in the main chain. Conversely, when residues are nearby, the main-chain flexibility around both residues decreases.

To visualize the differences, Figure3- 5 was generated by subtracting the distance maps of the polymorphisms from the WT PrP distance map. In this representation, the red colour indicates the contacts that are lost in the polymorphism (resulting in the increased distance), while the blue colour represents the interactions that were created in the polymorphisms (resulting in the decreased distance) but were absent in WT PrP. Significant differences between WT PrP and the polymorphisms are indicated by black arrowheads in Figure 3-5. Regions where the residues of the

polymorphisms gain bonds (distance decreased) are shown with black arrowheads and Arabic numerals, and regions where the polymorphisms have lost bonds (distance increased) are shown with black arrowheads and Roman numerals.

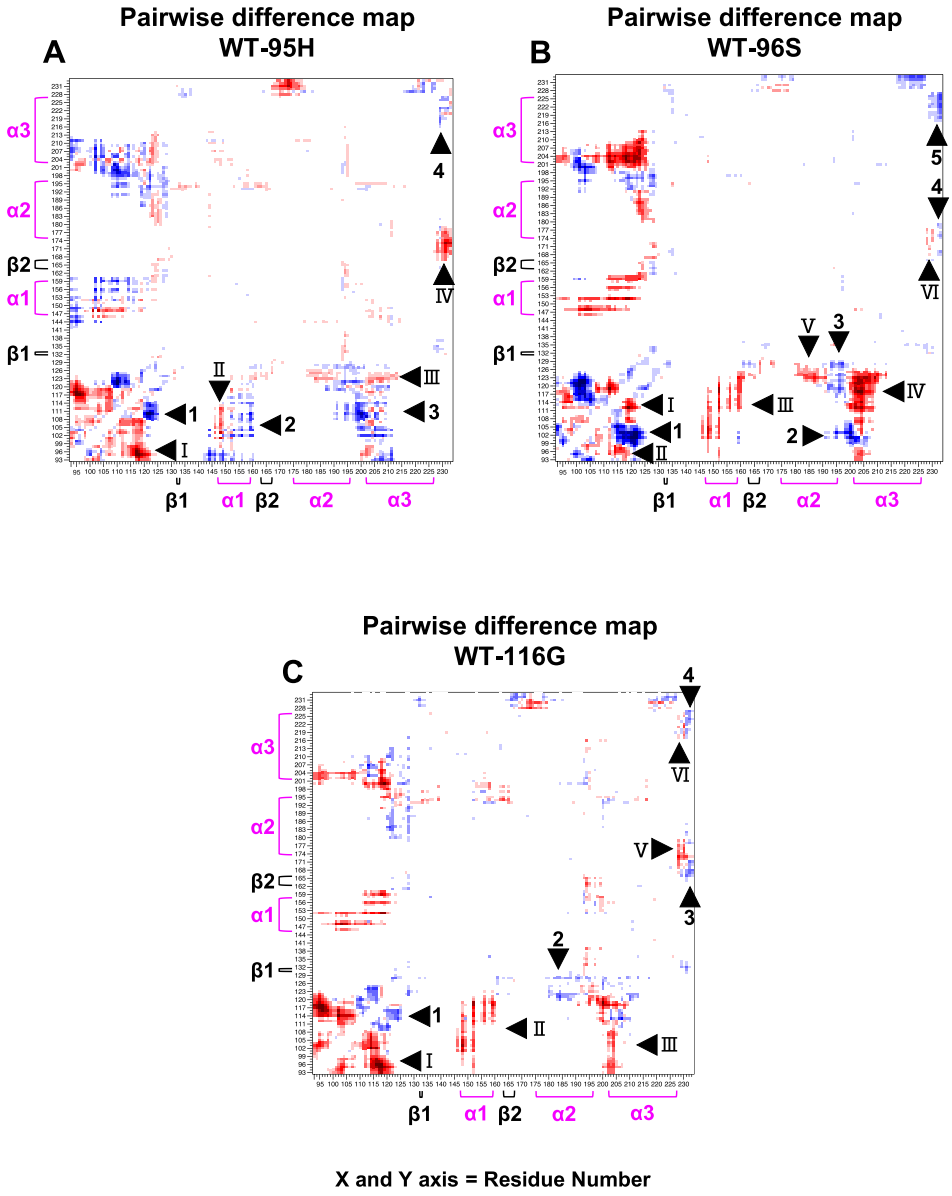

Figure 3-5. The pairwise difference maps generated by subtracting the distance maps of the polymorphism from the equivalent distance map of the WT protein. The X and Y-axis depict the residue numbers and the location of the known secondary structural elements based on the crystal structure of deer prion protein

(PDB ID: 4yxh (Baral et al. 2015)). The red and blue colours, respectively, represent increased and decreased pairwise distances in the polymorphisms versus the WT structure. Noticeable differences are marked with black arrowheads. Areas where the residues of the polymorphisms gain bonds (distance decreased) are shown with black arrowheads and Arabic numerals, and regions where the polymorphisms have lost bonds (distance increased) are shown with black arrowheads and Roman numerals. (**A**) Pairwise difference map between 95H and the WT. (**B**) Pairwise difference map between 96S and the WT. (**C**) Pairwise difference map between 116G and the WT.

Five regions stand out in the difference maps that encapsulate the major differences observed between WT PrP and the polymorphic systems. Region one: Involves the interactions within the N-terminus (residues 93-131). Region two: Corresponds to the interactions between α1 (147-159) and the N-terminus (93-131). Region three: Encompasses interactions between α2 (175-196), loop Lα2α3 (197-202), and α3 (203-227) with the N-terminus (93-131). Region four: Involves the interaction between loop Lα2β2 (165-178) and the C-terminus (228-231). Region five: Represents the interaction between α3 (203-227) and the C-terminus (228-231).

In Figure 3-5A, the discrepancies between WT PrP and the 95H polymorphism are emphasized. An increased distance (indicated by black arrowhead I) between residues 105-124 of the 95H polymorphism and residues 93-106 suggests the loss of bonds between these regions in the N-terminus. Conversely, reduced distances (black arrowhead 1) between residues 120-126 and 108-114 of the N-terminus imply a gain of bonds. Given the intrinsic flexibility of the N-terminus and the presence of

the 95H polymorphism in this region, it is expected to observe a distinct pattern of interactions in the N-terminus between WT PrP and the 95H polymorphism. Furthermore, in the case of the 95H polymorphism, both loss and gain of bonds are observed between α1 and the N-terminus. However, as depicted in Figure 3-5A, the blue region indicated by black arrowhead 2 appears more prominent than black arrowhead II, suggesting that the gain of bonds outweighs the loss of bonds. This implies that α1 exhibits greater stability in the 95H polymorphism compared to WT PrP. Additionally, an increase in interactions is observed between α2, loop Lα2α3, and α3 with the N-terminus, as indicated by black arrowhead 3. The black arrowhead III indicates a loss of bonds between the mentioned regions. However, a notable increase in the interactions between loop Lα2α3 and the N-terminus contributes to the enhanced stability of this region in the 95H polymorphism compared to WT PrP. Additionally, the interactions between the C-terminal residues and α3 (black arrowhead 4) further stabilize the third helix. On the other hand, the loop Lβ2α2 and the C-terminus exhibit a loss of interaction relative to WT PrP, potentially resulting in reduced stability of this loop (black arrowhead IV).

Figure 3-5B presents the disparities between the 96S polymorphism and WT PrP. In the N-terminus of 96S, both loss and gain of interactions are observed, denoted by black arrowheads I, II, and 1, respectively. Similar to the 95H polymorphism, the variable interaction patterns within the N-terminus of 96S can be attributed to the location of the polymorphism and the intrinsic flexibility of this region. Interestingly, in contrast to the 95H polymorphism, helix α1 in 96S exhibits a loss of interactions with

the N-terminus (indicated by black arrowhead III). This leads to a less stable α1 structure in 96S compared to WT PrP. Moreover, the region encompassing α2, loop Lα2α3, and α3 exhibits both losses and gains of bonds when compared to WT PrP. However, upon comparing the black arrowheads 2 and 3 (indicating increased distances and loss of interactions) with IV and V (indicating decreased distances and gain of interactions), it becomes apparent that the loss of interactions outweighs the gains. The significant increase in distance between the N-terminus and α2 as well as α3 results in fewer interactions and reduced stability of α2 and α3 in the 96S polymorphism. Despite the spatial separation between the initial residues of α3 and the N-terminus, it is noteworthy that the terminal residues of α3 exhibit an increased interaction with the C-terminus (indicated by black arrowhead 5), leading to enhanced stability of this region. Black arrowheads 4 and VI highlight residues within the rigid loop that demonstrate both loss and gain of interaction with the C-terminus. The rigid loop refers to the loop existing between β-sheet 2 and α-helix 2, which has been shown to be rigid in cervid PrP (Gossert et al. 2005). Conversely, in the majority of other mammalian species this loop is characterized as flexible and disordered (Lopez Garcia et al. 2000, Zahn et al. 2000, Lysek et al. 2005). Notably, it has been demonstrated that the rigid loop plays a significant role in cross-species prion susceptibility (Sigurdson et al. 2009, Soto 2009, Sigurdson et al. 2010, Kurt et al. 2014, Kurt et al. 2015).

Figure 3-5C illustrates the disparities between the 116G polymorphism and WT PrP. The N-terminus of 116G exhibits both losses and gains of interactions, indicated by

black arrowheads I and 1, respectively. Notably, the loss of interaction within the N-terminus is more pronounced in 116G compared to both 96S and 95H. This renders the N-terminal region of 116G the most flexible among the analyzed systems, as also depicted in the dotted region of Figure 3-3D. It is interesting to note that the increased distance observed between α1 and the N-terminus is similar in both 116G and 96S (indicated by black arrowheads II in Figure 3-5B and C), contrasting with the pattern observed in 95H (black arrowhead 2 in Figure 3-5A). Furthermore, a loss of interaction is observed between the N-terminus of 116G and its loop Lα2α3, which is consistent with the findings in 96S and differs from the behavior seen in 95H. Black arrowheads 4 and VI indicate the interactions involving the terminal residues of α3 with the C-terminus, which predominantly show gained bonds while partially losing interactions. Notably, the interactions of the rigid loop in 116G differ from WT PrP and predominantly display lost bonds with the C-terminus (indicated by black arrowhead V).

To gain a deeper understanding of the observed differences among the protein variants, the bonds and interactions between residues were explored by calculating parameters such as hydrogen bonds, salt bridges, and solvent-accessible surface area.

The hydrogen bonds (h-bonds) within each construct were computed for the final 15 ns of R1, R2, and R3 simulations. The obtained data were averaged and plotted in

Figure 3-6. Surprisingly, no substantial differences were observed between the systems, suggesting that the polymorphisms have minimal impact on the hydrogen bonds within the protein structures.

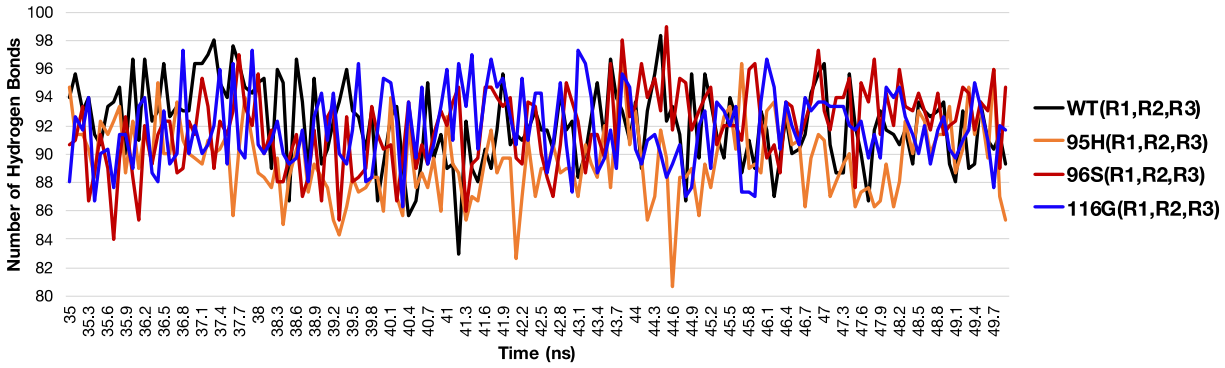

Figure 3-6. Number of hydrogen bonds for the polymorphisms 95H (orange), 96S (red), 116G (blue), and the WT PrP structure (black). Each graph represents the average number of hydrogen bonds calculated for the final 15 ns of the simulation (R1, R2, R3).

To gain deeper insights into the hydrogen bonds, further calculations were conducted for two distinct groups of residues, namely Group1 (G1) and Group2 (G2), as labelled in Figure 3-4. Residues within these two regions exhibit significant differences in fluctuation patterns (as shown in Figure 3-4) and display distinct pairwise distances when comparing the different protein constructs (as observed in Figure 3-5). Group1 (G1) encompasses residues Lys107 to Ala120, which are in the N-terminal region. Group2 (G2) includes residues Thr194 to Thr204, representing the loop Lα2α3. The results of these calculations are depicted in Supplementary Figure 3-4. Our findings show that the polymorphism induces alterations in the hydrogen bonding patterns of

residues within the G1 and G2 regions when compared to the WT (Supplementary Figure 3-4). However, we did not observe any significant or meaningful differences in the hydrogen bonding profiles between the polymorphisms and the WT that could explain the observed reductions in fluctuations and enhancements in pairwise interactions seen in 95H, as well as the increased fluctuations and decreased pairwise interactions observed in 96S and 116G (Figure 3-4 and Figure 3-5).

Salt bridge calculations were performed, and the results are summarized in Table 3-1. The final 15 ns trajectories from three simulation rounds (R1, R2, R3) were computed and averaged to serve as inputs for the salt bridge plugin of VMD.

Table 3-1. Salt bridge interactions for the WT PrP and the polymorphisms. The salt bridges were calculated using the final 15 ns of the trajectories from R1, R2, and R3 simulations, and the average values were utilized to assess the presence or absence of potential salt bridges.

Location on the 3D structure	Residues involved		WT	95H	96S	116G
	GLU203	LYS207	✓	✓	✓	✓
α3-Nterminal	GLU203	LYS107	✓	x	x	✓
*α3-Nterminal	ASP205	LYS113	✓	✓	x	x
	ASP150	ARG154	✓	✓	✓	✓
	ASP147	ARG154	✓	✓	✓	✓
α3-α3	GLU224	ARG223	✓	x	x	✓
	GLU214	ARG211	✓	✓	✓	✓
	GLU210	LYS207	✓	✓	✓	✓
	GLU210	ARG211	✓	✓	✓	✓
α1-α1	GLU155	ARG151	✓	x	x	✓
	ASP181	ARG167	✓	✓	✓	✓
	ASP170	ARG231	✓	✓	✓	✓
α1-Nteminal	ASP150	HIS143	✓	x	✓	✓
	ASP147	ARG151	✓	✓	✓	✓
α3-α1	ASP205	ARG159	x	✓	✓	✓
α1-α3	GLU149	ARG211	x	✓	✓	✓
α1-Nteminal	GLU149	LYS113	x	✓	x	✓
α1-α3	GLU149	LYS207	x	✓	✓	✓
α1-Nteminal	GLU155	LYS107	x	✓	✓	x
Loopα2α3-α1	GLU199	ARG159	x	✓	✓	✓
Loopα2α3-Nterminal	GLU199	LYS113	x	✓	x	x
Loopα2α3-Loopα2α3	GLU199	LYS197	x	✓	x	✓
α3-Nterminal	GLU214	HIS99	x	✓	x	x
α3-Cterminal	GLU224	ARG231	x	✓	x	✓
α3-Nterminal	GLU203	HIS99	x	x	✓	x
α1-Nterminal	ASP147	LYS107	x	x	x	✓
α3-Nterminal	ASP205	HIS99	x	x	x	✓
α1-α1	GLU155	ARG154	x	x	x	✓
α1-Nterminal	GLU155	LYS109	x	x	x	✓
α3-Nterminal	GLU203	LYS113	x	x	x	✓
α3-Nterminal	GLU210	LYS107	x	x	x	✓
α3-Nterminal	GLU214	LYS107	x	x	x	✓

Among the salt bridges listed in Table 3-1, the first 14 represent bonds that are present in the WT and partially lost in the polymorphisms, while the following eighteen SBs are bonds that are absent in the WT but were detected in either 95H, 96S, or

116G. Notably, polymorphism 95H exhibits a total of 20 SBs, including 10 SBs that are similar to those in the WT and 10 new SBs. This implies that four SBs present in the WT are lost in the 95H polymorphism. These SBs are between GLU203 (α3) & LYS107 (N-terminus), GLU224 (α3) & ARG223 (α3), GLU155 (α1) & ARG151 (α1), and ASP150 (α1) & HIS143 (loop Lβ1α1). On the other hand, 96S exhibits 16 SBs, with 10 common bonds shared with the WT and 6 new bonds. The four SBs that are present in WT and absent in 96S are GLU203 (α3) & LYS107 (N-terminus), GLU224 (α3) & ARG223 (α3), GLU155 (α1) & ARG151 (α1), and ASP205 (α3) & LYS113 (N-terminus). Three of these four bonds are also absent in 95H. Construct 116G displays a total of 27 SBs, with 13 common bonds shared with the WT and has only lost ASP205 (α3) & LYS113 (N-terminus). However, 14 new SBs are formed in 116G that are not present in the WT.

Based on the results of the salt bridge calculation, it can be inferred that the presence or absence of the salt bridge between D205 and K113 (formed between helix α3 and the N-terminus) in WT and 95H, compared to its absence in 96S and 116G polymorphisms, may play a role in PrP stability. This particular salt bridge could potentially contribute to the reduced stability observed in 96S and 116G compared to the WT. Notably, the formation of this salt bridge between ASP205 and LYS113 occurs within the G1 and G2 regions (as depicted in Figure 3-4), where significant differences in structural deviations are observed among the constructs, particularly higher fluctuations in 96S and 116G.

Figure 3-7 presents the calculation and comparison of the Solvent Accessible Surface Area (SASA) of the protein among the different constructs. The total SASA, which encompasses both the hydrophobic and hydrophilic surface areas, was computed for the final 15 ns of simulations from rounds one, two, and three. The average values are plotted in Figure 3-7A.

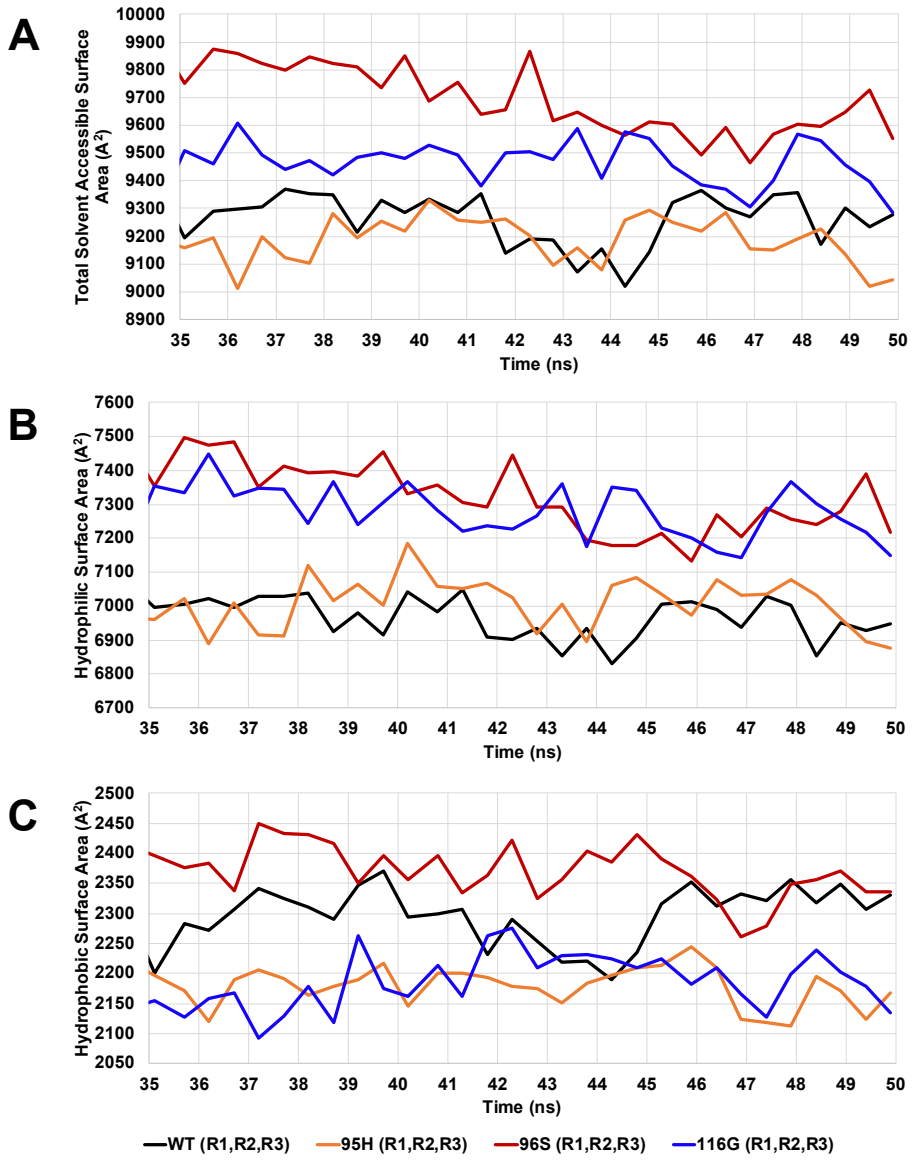

Figure 3-7. The total solvent accessible surface area for the 95H (orange), 96S (red), and 116G (blue) polymorphisms, as well as WT PrP (black). (**A**) The total SASA (hydrophobic plus hydrophilic surface area) for the polymorphisms and the WT PrP. (**B**) Hydrophilic surface area for the polymorphisms and the WT. (**C**) Hydrophobic surface area for the polymorphisms and the WT. All graphs are the average of three rounds of simulation (R1, R2, R3) and calculated only for the final 15ns of simulation.

The total SASA values for WT, 95H, 96S, and 116G are represented by black, orange, red, and blue graphs, respectively, in Figure 3-7. Among these constructs, 96S exhibits significantly higher total SASA values compared to WT. By examining Figures 3-7B and 7C, which display the averaged hydrophilic and hydrophobic surface areas, respectively, it is evident that the increased total SASA in 96S is primarily attributed to an expansion of its hydrophilic surface area. 116G demonstrates a decrease in its hydrophobic surface area (Figure 3-7C) along with a notable increase in its hydrophilic surface area (Figure 3-7B), resulting in a slightly higher total SASA compared to WT (Figure 3-7A). In contrast, 95H exhibits decreased solvent exposure (Figure 3-7A, orange graph) relative to WT, which can be attributed to a reduction in its hydrophobic surface area (Figure 3-7C, orange graph).

In contrast to the h-bonds and salt bridges, the differences in solvent-accessible surface area among the constructs are substantial. This suggests that hydrophobic interactions may play a more significant role in the altered dynamic properties observed between the constructs. The decreased pairwise distances in 95H, leading to increased stability and lower backbone fluctuations, are likely attributed to the increased hydrophobic interactions. This is evident from the notable difference in hydrophobic surface area between 95H and WT (Figure 3-7C). On the other hand, the increased pairwise distances and fluctuations in the structure of 96S and 116G may be influenced by the significant differences in their hydrophilic surface areas compared to WT.

The impact of amino acid substitutions in 96S, 95H, and 116G on the secondary structure elements was assessed using the secondary structure (SS) plugin of the VMD analysis package (Frishman & Argos, 1995). The secondary structure was calculated for the final 15 ns of simulations (R1, R2, and R3) for each system, and the average was employed to determine the prevalent secondary structure elements, such as α-helices, β-strands, and β-bridges, for each residue (Figure 3-8).

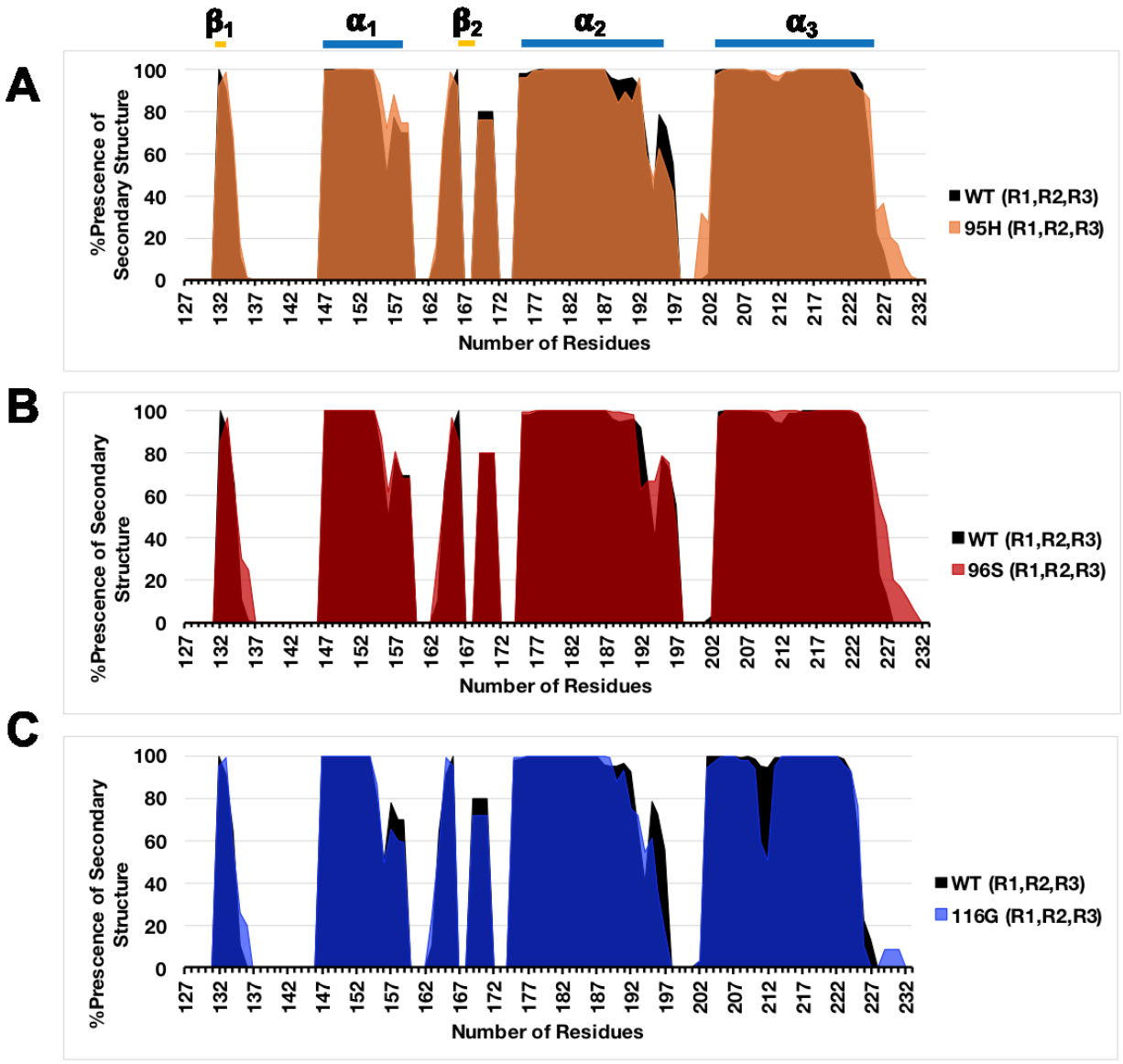

Figure 3-8. Per-residue percentage of dominant secondary structure for the last 15 ns of simulation. The black graph represents WT PrP, and the orange (**A**), red (**B**), and blue (**C**) graphs represent 95H, 96S, and 116G polymorphisms, respectively. The location of known secondary structure elements, determined based on the crystal structure of deer prion protein (PDB ID: 4yxh (Baral et al. 2015)), is depicted using yellow and blue bars at the top of the figure.

Figure 3-8 reveals distinct structural variations in the secondary structure elements of the analyzed protein variants. Notably, β1 exhibits a slight elongation in 96S (red) and 116G (blue) compared to WT (black) and 95H (orange), while β2 remains largely conserved across all four constructs. Assessment of helical structures highlights notable disruptions in the helices of 116G, particularly in α3 (Figure 3-8C). Residues 210 and 211 within α3 of 116G exhibit a transition from helical conformation to turns for more than ~50% of the simulation time in two out of three simulation rounds (Supplementary Figure 3-5). Conversely, both 95H and 96S display an extension of α3 relative to WT. Like 116G, 95H shows signs of helical disruption in α2 when compared to WT. New secondary structure elements are observed in all constructs involving residues 169 to 171, predominantly featuring 3-pi helices (Supplementary Figure 3-5). Interestingly, the 95H polymorphism exhibits an additional new secondary structure element in its Loopα2α3 region (residues 201 and 202), adopting a beta bridge conformation for more than 30% of the simulation time (Supplementary Figure 3-5).

An overall assessment of the secondary structure reveals that the 116G polymorphism displays the greatest degree of structural disruption compared to WT. The observed fluctuations (Figure 3-4, blue graph) and increased pair residue distances (Figure 3-5C) associated with the 116G variant may contribute to its SS element disruptions. However, the 96S polymorphism, which exhibits similar dynamic behavior to 116G (Figure 3-4 and 3-5B), shows slight elongation of its β1 and α3 elements. Lastly, the 95H construct exhibits disruptions in α2 and elongation of α3,

accompanied by the appearance of new beta bridge elements in its loop Lα2α3 region. These newly formed beta bridges in 95H could potentially account for its increased stability compared to WT and the other polymorphisms.

Finally, to evaluate the effect of these polymorphisms on the aggregation propensity of deer PrP, we compared the aggregation kinetics of recombinant PrP with the wild type, 95H and 96S sequences. Using RT-QuIC assay, we followed Thioflavin T fluorescence as a measurement of amyloid fibril formation (Figure 3-9). Under our experimental conditions, it took approximately 37 hours for the wild type PrP to start forming amyloid fibrils. Interestingly, 95H and 96S polymorphisms have an opposite effect on the aggregation propensity of PrP when compared with wild type. Whereas 95H makes PrP more prone to aggregate, with a lag phase of approximately 12 hours, the polymorphism 96S substantially delays the aggregation of PrP to approximately 80 hours.

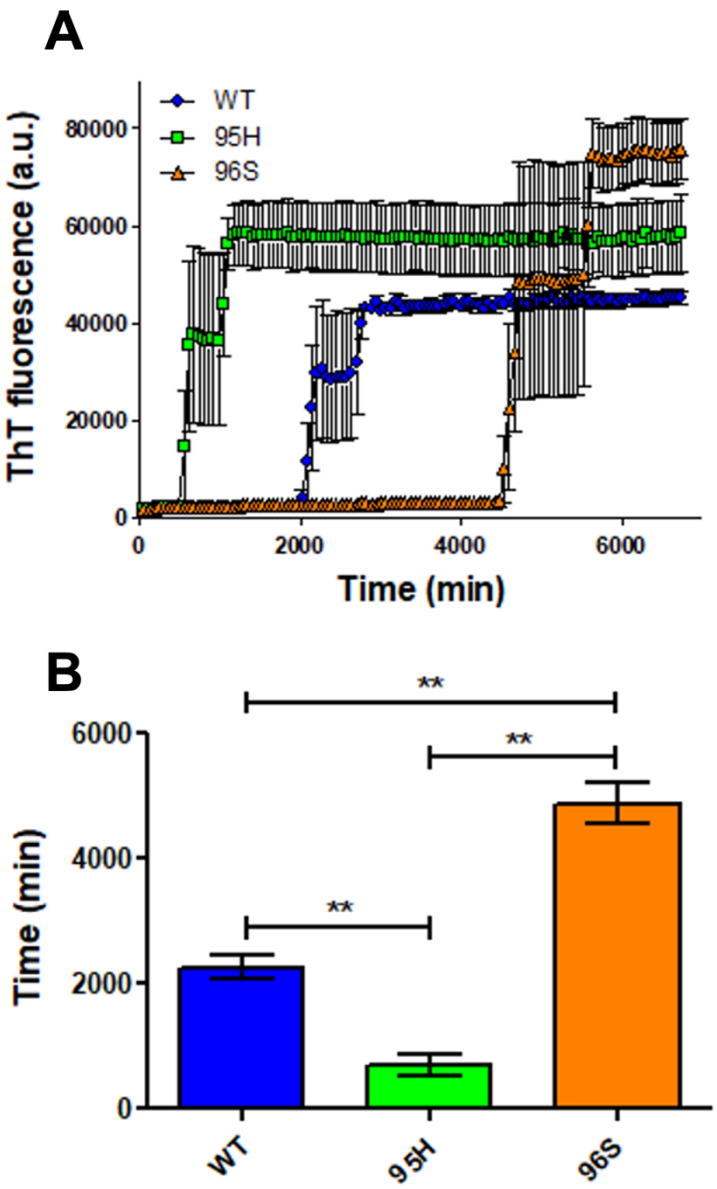

Figure 3-9. Effects of 95H and 96S polymorphisms on the *in vitro* aggregation of deer PrP. (**A**) Kinetics of aggregation of wild type (blue), 95H (green), and 96S (orange) deer PrP. (**B**) Lag phases calculated from the kinetics depicted in (A). Data represent an average of 3 replicates, and error bars represent SE.

3.4 DISCUSSION

The structural models for WT, 95H, 96S, and 116G spanning residues 93 to 233 were generated based on the crystal structure of the deer prion protein template (PDB code: 4yxh (Baral et al. 2015)). However, the crystal structure and, therefore, the initial models lacked the flexible N-terminal residues 93 to 123 and C-terminal residues 232 to 233. Hence, these missing residues were manually added following the procedures described in the methods section. Molecular dynamics simulations were performed for the white-tailed deer wild type prion protein and polymorphisms 95H, 96S, and 116G under neutral pH conditions. To ensure the reproducibility and consistency of the results, the simulations were conducted with three different starting atom velocities, labelled R1, R2, and R3. The simulations were carried out for a duration of 50 ns. The findings reveal substantial differences between the models harboring the polymorphisms and the WT protein. It is intriguing to observe these distinctions, considering the significant impact these polymorphisms have on the behavior of prion-infected individuals, such as increased incubation time and partial resistance to chronic wasting disease. The results demonstrate that the conformations adopted by 95H, 96S, and 116G are unique and distinguishable from one another and the WT protein (Figure 3-2).

Overall, 95H polymorphism has a better-ordered structure compared to WT and is making the PrP^C structure steadier by reducing the fluctuations of almost every residue. On the other hand, the 96S and 116G polymorphisms exhibit the opposite

effect, resulting in increased dynamics and less stability. The polymorphisms are possibly dictating their dynamic changes by altering the hydrophobic interactions since their effect on the solvent-accessible surface area (Figure 3-7) is much more substantial than the hydrogen bonds (Figure 3-6) and salt bridges (Table 3-1). Furthermore, analysis of distance maps reveals substantial changes in inter-residue distances upon the introduction of the polymorphisms (Figure 3-5). The introduction of the 95H polymorphism in PrP^{C} leads to reduced distances between its residues compared to WT, resulting in decreased main-chain flexibility and enhanced stability, particularly in helix, helix2, helix3, and loop Lα2α3. Conversely, the 96S and 116G polymorphisms display the opposite effect, as these regions experience increased distances and diminished interactions, leading to decreased stability. Additionally, the rigid loop (loop Lβ2α2) in the polymorphisms exhibits an altered correlation pattern compared to WT. Interestingly, there is experimental evidence showing that the distal region of helix3 interacts with the rigid loop and forms a protein surface that is part of a hypothetical “protein X” epitope that affects PrP^{C} conversion and strain propagation (Gossert et al. 2005, Perez et al. 2010, Angers et al. 2014). Figure 3-5A black arrowhead IV, 5B black arrowheads 4 &VI, and 5C black arrowheads 3 &V demonstrate that the interaction between the rigid loop and the C-terminal region (adjacent to the distal residues of helix 3) differs among the four systems. These differences in the protein surface epitope interaction may contribute to the altered conversion of PrP^{C} to PrP^{Sc} and potentially play a role in the prolonged disease incubation period observed in cervids carrying these polymorphisms. Studies also show sequence variation of the rigid loop amongst species affects the flexibility of this

loop that plays an important role in controlling species barrier (Sigurdson et al. 2009, Soto 2009, Sigurdson et al. 2010, Kurt et al. 2014, Kurt et al. 2015). In this study, we demonstrate that the introduction of polymorphisms to the protein structure, despite being distant from the location of the rigid loop, impacts its dynamics, interactions, and, subsequently, its flexibility. These alterations in the rigid loop can potentially contribute to the increased incubation time observed in deer populations carrying these polymorphisms. Additionally, the assessment of secondary structure elements revealed that the 116G polymorphism exhibits signs of structural disruption compared to WT, while the 96S polymorphism, which shares similar dynamic behavior with 116G, only shows a slight elongation of its β1 and α3 regions. However, the 95H construct displays disruption in α2 and elongation in α3, along with the emergence of new beta bridge elements in its loop Lα2α3 region.

Further exploration through MD simulation studies on disease-associated polymorphisms can significantly enhance our understanding of the relationship between amino acid substitutions and their observed effects in animals. This knowledge can be leveraged to design polymorphisms that confer resistance to the disease, thus offering valuable insights for disease prevention and management. Breeding programs targeting animals with specific polymorphisms, such as the 96SS variant linked to reduced susceptibility to chronic wasting disease, have been implemented by farmers in Canada. However, careful consideration is needed to weigh the potential drawbacks and unintended consequences of such strategies. It is important to note that animals carrying the 96SS polymorphism exhibit an extended

incubation time, which may increase the risk of prion shedding and contribute to the spread of the disease within and between populations. By integrating computational studies with experimental validation, we can unlock the potential to design and propagate resistant polymorphisms, thereby safeguarding animal populations.

3.5 SUPPLEMENTARY FIGURES

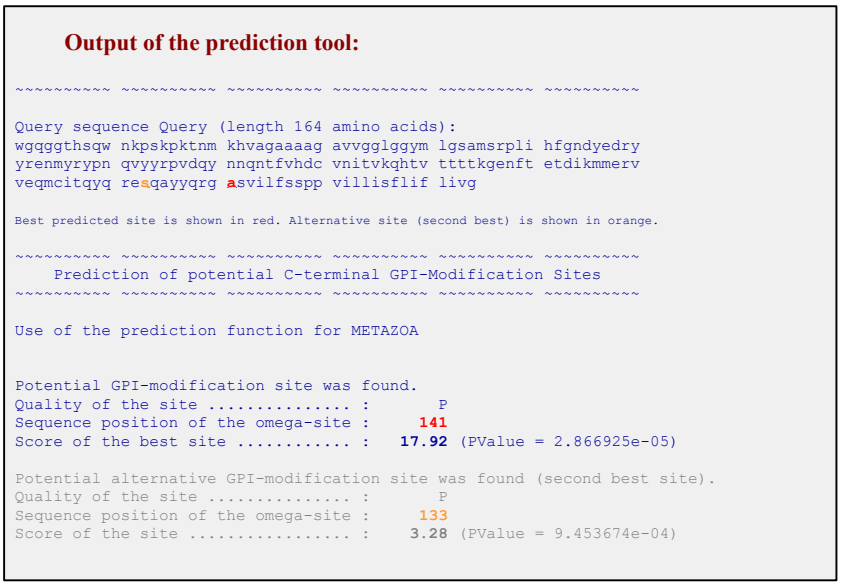

Output of the prediction tool:

~~~~~~~~~~ ~~~~~~~~~~ ~~~~~~~~~~ ~~~~~~~~~~ ~~~~~~~~~~ ~~~~~~~~~~

Query sequence Query (length 164 amino acids):
wgqggthsqw nkpskpktnm khvagaaaag avvgglggym lgsamsrpli hfgndyedry
yrenmyrypn qvyyrpvdqy nnqntfvhdc vnitvkqhtv ttttkgenft etdikmmerv
veqmcitqyq reaqayyqrg asvilfsspp villisflif livg

Best predicted site is shown in red. Alternative site (second best) is shown in orange.

~~~~~~~~~~ ~~~~~~~~~~ ~~~~~~~~~~ ~~~~~~~~~~ ~~~~~~~~~~ ~~~~~~~~~~
Prediction of potential C-terminal GPI-Modification Sites
~~~~~~~~~~ ~~~~~~~~~~ ~~~~~~~~~~ ~~~~~~~~~~ ~~~~~~~~~~ ~~~~~~~~~~

Use of the prediction function for METAZOA

Potential GPI-modification site was found.
Quality of the site ..... : P
Sequence position of the omega-site : 141
Score of the best site ..... : 17.92 (PValue = 2.866925e-05)

Potential alternative GPI-modification site was found (second best site).
Quality of the site ..... : P
Sequence position of the omega-site : 133
Score of the site ..... : 3.28 (PValue = 9.453674e-04)

Supplementary Figure 3-1. Prediction of the GPI modification site. Big-PI Predictor (Eisenhaber et al. 1998, Eisenhaber et al. 1999, Eisenhaber et al. 2000) is an online software to identify the most probable GPI modification site. The result suggests that alanine at position 233 is probably the cleavage site in the white-tailed deer sequence with a PValue of 2.86e-05.
~~~~~~~~~~

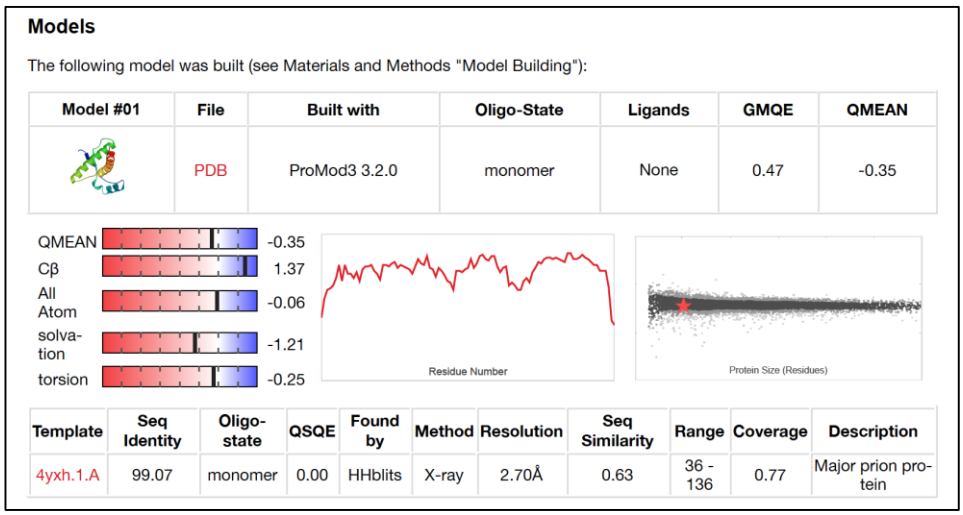

Models

The following model was built (see Materials and Methods "Model Building"):

Model #01	File	Built with	Oligo-State	Ligands	GMQE	QMEAN
	PDB	ProMod3 3.2.0	monomer	None	0.47	-0.35

Template	Seq Identity	Oligo-state	QSQE	Found by	Method	Resolution	Seq Similarity	Range	Coverage	Description
4yxh.1.A	99.07	monomer	0.00	HHblits	X-ray	2.70Å	0.63	36 - 136	0.77	Major prion protein

Supplementary Figure 3-2. The initial 3D model for white-tailed deer PrP residues 124 to 231 built using the SWISS-MODEL homology modelling server (Arnold et al. 2006). The crystal structure of deer prion protein with PDB code: 4yxh (Baral et al. 2015), model 1, chain A was chosen as the best template with a sequence identity of 99.01%, GMQE (Global Model Quality Estimation) score of 0.78 and a QMEAN4 score of -0.10.

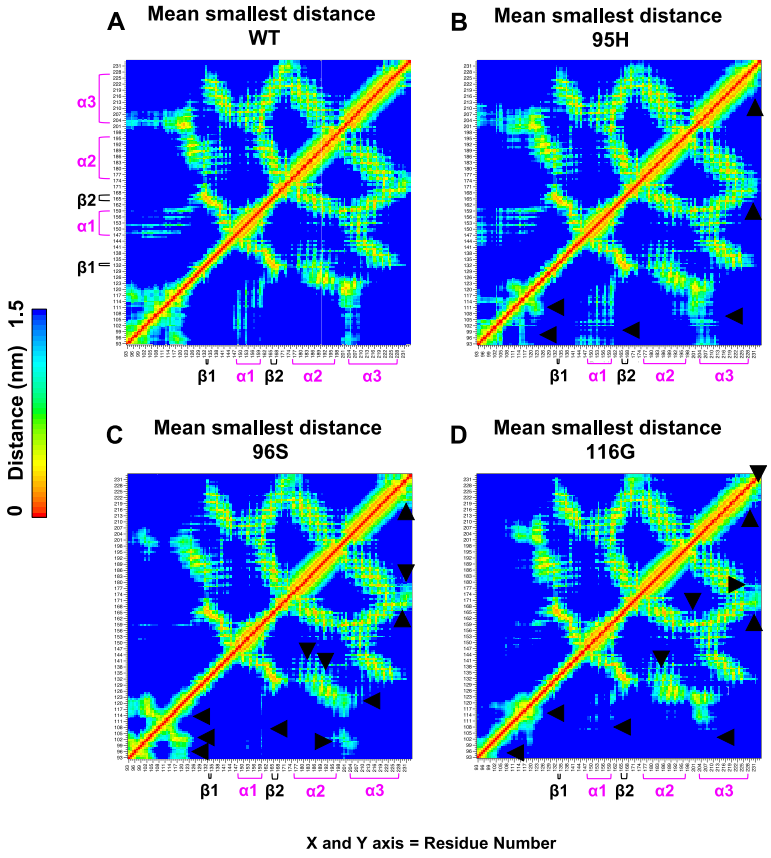

Supplementary Figure 3-3. Distance maps for WT PrP and the 95H, 96S, and 116G polymorphisms, respectively. The last 15 ns trajectories for rounds one, two, and three of the simulation were averaged and used to calculate the distances between residue pairs in their tertiary structure as a function of time for WT PrP (**A**), as well as the 95H (**B**), 96S (**C**), and 116G polymorphism (**D**). Shorter distances are shown in red and orange colours, whereas light green and blue correspond to longer distances between the residues. Regions with visible differences between the polymorphisms and WT PrP are shown with black arrowheads. The location of the known secondary structure elements based on the crystal structure of deer prion protein (PDB ID: 4yxh (Baral et al. 2015)) are shown on the x and y axes.

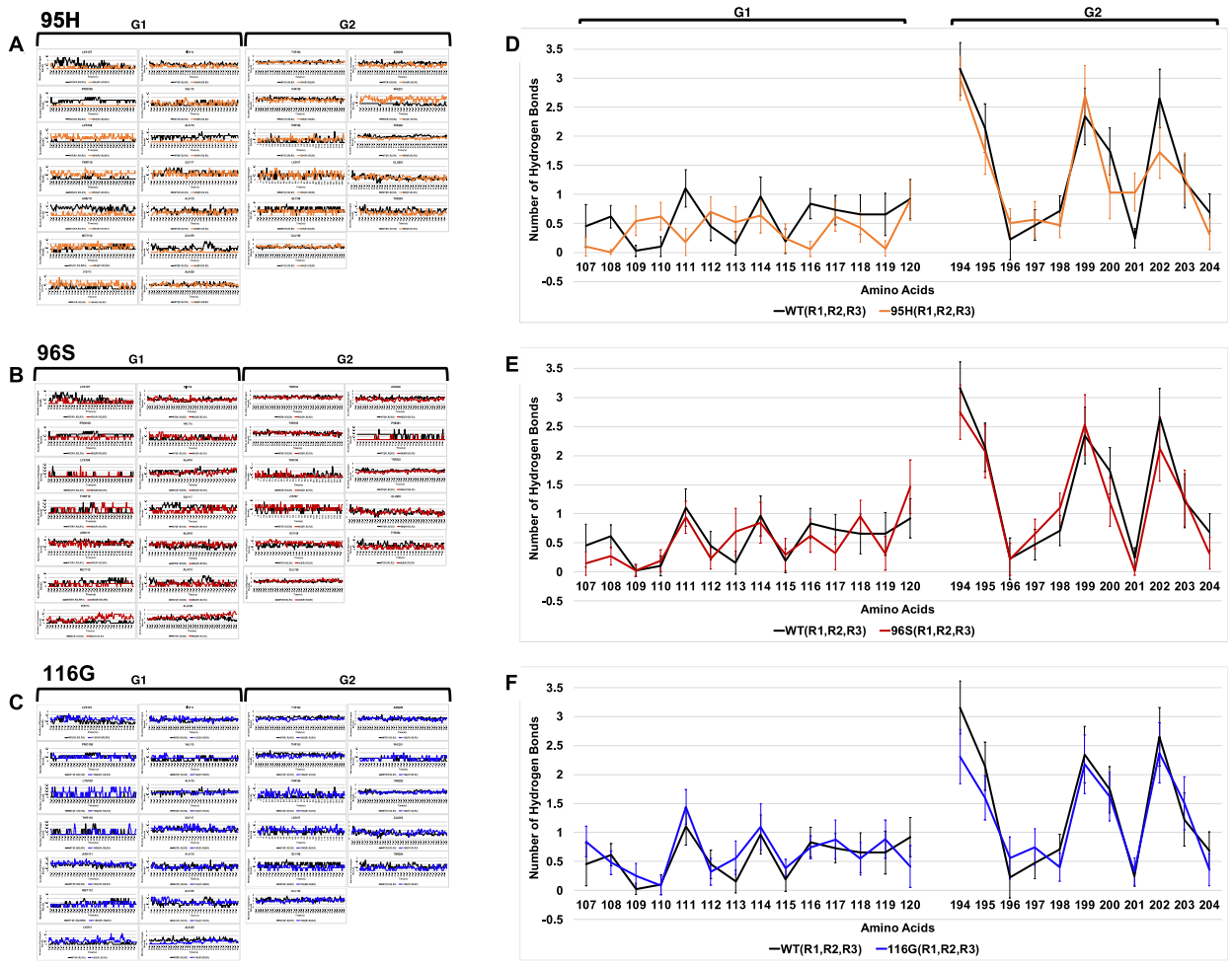

Supplementary Figure 3-4. The h-bonds for every residue in G1 and G2 regions that showed the biggest difference in the per-residue structural fluctuations (Figure 3-4). G1 contains residues Lys107 -Ala120 and is in the N-terminal region. G2 covers Thr194 to Thr204, embodying the loop Lα2α3. The h-bonds for every residue in the G1 and G2 region were calculated for R1, R2 and R3 of the final 15 ns of simulation and plotted. (**A**) 95H is shown in orange versus WT PrP, shown in black. (**B**) 96S is shown in red versus WT PrP. (**C**) 116G is shown in blue versus WT PrP. For better visualization of the effect of the polymorphism on the hydrogen bonds, graphs **D**, **E**, and **F** were generated, and the number of hydrogen bonds for every amino acid is represented by a dot, which is the average of its h-bonds throughout the final 15ns of simulation. (**D**) For polymorphism 95H, amino acids Lys109, Thr110, Met112, Lys113, Thr196, Lys197, Glu199, and Phe201 show an increased number of h-bonds compared to WT. The underlined residues show an increase in their number

of hydrogen bonds compared to WT and may play a role in the decreased fluctuations of G1 and G2 regions (Figure *3*-4). (**E**) Amino acids Lys107, Pro108, ASN111, Met112, His114, Ala116, Gly117, Ala119, Thr194, Asn200, Phe201, Thr202, and Thr204 show fewer h-bonds in 96S compared to WT. The underlined residues show a significant decrease in their number of h-bonds compared to WT and may play a role in the increased fluctuations of 96S in the G1 and G2 regions seen in the RMSF graph (Figure *3*-4). (**E**) Residues Pro108, Met112, Gly116, Ala118, Ala120, Thr194, Thr195, Gly198, Glu199, Asn200, Thr202, and Thr204 show decreased number of h-bonds in the structure of 116G polymorphism. The underlined residues have a significantly higher number of h-bonds compared to WT, which may play a role in the increased fluctuation of G1 and G2 regions (Figure *3*-4).

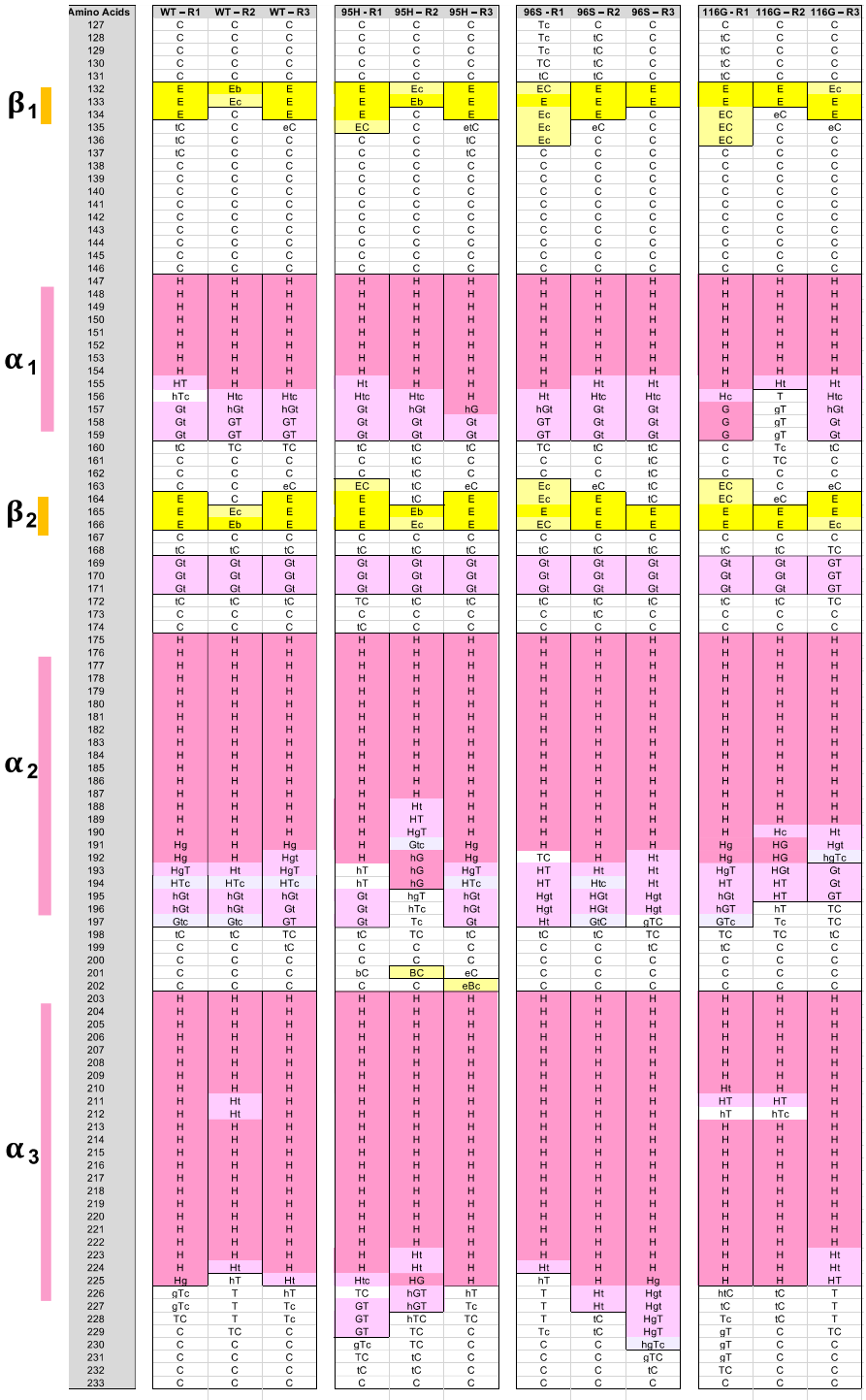

Supplementary Figure 3-5. The dominant secondary structure elements calculated for the last 15ns of the simulation for every residue in each round of MD simulations (R1, R2, and R3). H/h stands for alpha helix, G/g for 3-pi helix, E/e for extended beta-sheet, B/b for beta bridge, T/t for turn, and C/c for random coil.

The presence of the secondary structure elements that are less than %10 are ignored, 10-30% are shown in small letters, and 30-100% are in large letters. The averages from the three simulations were used to generate the curve in Figure *3*-8.

Chapter 4: Conclusion and Future Directions

Prion diseases are a group of neurological disorders characterized by the abnormal folding of the prion protein, resulting in an infectious form called PrP^{Sc}. Chronic wasting disease is a prion disease that affects cervids such as deer, elk, moose, and reindeer. CWD is particularly concerning due to its impact on wild animals, efficient spread, peripheral excretion of the infectious agent, long incubation period, and ongoing uncertainty regarding its zoonotic potential.

The emergence of variant Creutzfeldt-Jakob Disease, which resulted from the transmission of BSE (prion disease in cattle commonly known as mad cow disease) to humans in the UK, prompted global efforts to understand the barriers to prion species transmission. These efforts aimed to protect human and animal health and minimize the economic consequences. The discovery of BSE in Canada led to import bans on ruminants and ruminant products from Canada by 34 countries. This had a significant economic impact, particularly on Alberta's beef industry, causing substantial financial losses of billions of dollars (Petigara et al. 2011).

Regarding chronic wasting disease, although no instances of transmission to humans have been reported thus far, the disease continues to impose a substantial economic burden on the cervid farming industry in North America, primarily due to regulatory costs. According to Arnot et al., increased biosecurity and biosafety interventions on Canadian farms can result in annual value risks of up to $12 million (Arnot et al. 2009, Makau et al. 2020). Furthermore, the consistent impact of CWD infections poses a

substantial threat to the Canadian agriculture industries and their national economic contribution. In the United States, federal government agencies allocated over $284 million between 2000 and 2021 for CWD-related efforts (Chiavacci 2022). In addition, the impact of CWD on Indigenous communities is significant, given the crucial role cervid species play as food sources and cultural symbols. Many Indigenous groups in Canada worry about rising disease rates and wildlife contamination, which directly jeopardize their traditional practices involving moose, elk, and deer consumption (Parlee et al. 2021).

Gaining insight into the current social and economic implications of CWD and considering the possible zoonotic transmission of CWD to humans enhances our understanding of the wide-ranging societal effects that could potentially emerge and underscores the importance of investing in CWD-related research.

The species barrier phenomenon in prion diseases is believed to be influenced by two key factors (Gajdusek et al. 1965, Prusiner et al. 1998); the differences in the amino acid sequence of the prion protein across species and the presence of distinct types of PrP^{Sc} (prion strains) with varying amyloid forms that possess different transmission properties. Therefore, researching both the cellular prion protein and how alterations in its primary structure can impact susceptibility to prion diseases, as well as studying the infectious prions in different hosts, can significantly enhance our understanding of the factors influencing the species barrier. This knowledge will

better equip us to anticipate and manage the potential spillover of prion diseases across different species.

In my dissertation project, I have studied the structure of infectious CWD prions and examined the influence of cervid polymorphisms on the cellular prion protein's structure.

4.1 ELECTRON MICROSCOPY STUDY OF INFECTIOUS CWD PRION

Recently high-resolution cryo EM structures of the mouse and hamster-adapted scrapie and GSS prions were published (Kraus et al. 2021, Hoyt et al. 2022, Hoyt et al. 2022, Manka et al. 2022, Manka et al. 2023). They provide valuable structural information that could be used to design effective structure-based therapeutics.

To date, no structural information is available on the brain-derived CWD prions, and no structural information is available on any of the infectious prion protein's N-terminal region. This study, for the first time, offers insights into the structural architecture of full-length and truncated brain-derived CWD prions (Figure 4-1). For this purpose, CWD prions were purified from the brains of CWD-positive Tg33 mice and white-tailed deer. This was achieved by using either proteinase K to generate N-terminally truncated PrP or Pronase E to produce full-length PrP. Clinical prion disease symptoms were developed when the purified samples were intracerebrally

injected into Tg33 mice, demonstrating that both the full-length and N-terminally truncated forms of CWD prions retain their infectious properties and can transform normal PrP into their aberrant disease-causing conformer.

Upon examination of the purified CWD prions through transmission electron microscopy, the fibrils were found to be morphologically heterogeneous. Unlike previously studied brain-derived scrapie (Kraus et al. 2021, Manka et al. 2023) and BSE prion fibrils (Kamali-Jamil et al. 2021) with a maximum width of 10 to 20 nm, the majority of CWD prion fibrils were thicker, with a diameter of approximately 35 nm. The study also revealed that infectious full-length CWD prions displayed striations with a spacing of 3.3 to 3.5 nm (in CWD-positive tg33 mice) and 3.7 nm (in CWD-positive white-tailed deer) that were absent in the N-terminally truncated form, indicating that these striations correspond to the N-terminal region of the prion protein. The presence of ordered striations on the full-length form of CWD prions was observed to be enhanced with the utilization of EDTA, a chelator. Previous studies have shown that copper ions interact with the N-terminal region (OR region) of PrP and have an impact on the conformations of both PrP^{C} and PrP^{Sc} (Wadsworth et al. 1999, Salzano et al. 2019). Consequently, the removal of these cations using EDTA could result in changes to the structural conformation, influencing the appearance of the N-terminus (striations). The presence of the N-terminal region (residues ~23 to 90) in the primary structure of full-length CWD prions was confirmed through Western blot analysis by utilizing the anti-PrP antibody Fab3, which specifically binds to residues 26 to 37. Furthermore, the presence of the N-terminus on the quaternary

structure of the full-length CWD prions was confirmed using negative stain electron microscopy, which revealed the presence of the N-terminal region (as indicated by striations) only on the full-length CWD prion.

These findings offer new insights into the quaternary structure of CWD amyloid fibrils and provide the initial report on the detection of the N-terminus structure of these infectious prions. Elucidating the structure of the N-terminal region could be significant in comprehending the pathogenic processes of prion diseases. Additionally, investigating the strain-specific features of CWD prions may improve our understanding of the species barrier and facilitate the development of prion vaccines in the event of a potential zoonotic outbreak of CWD.

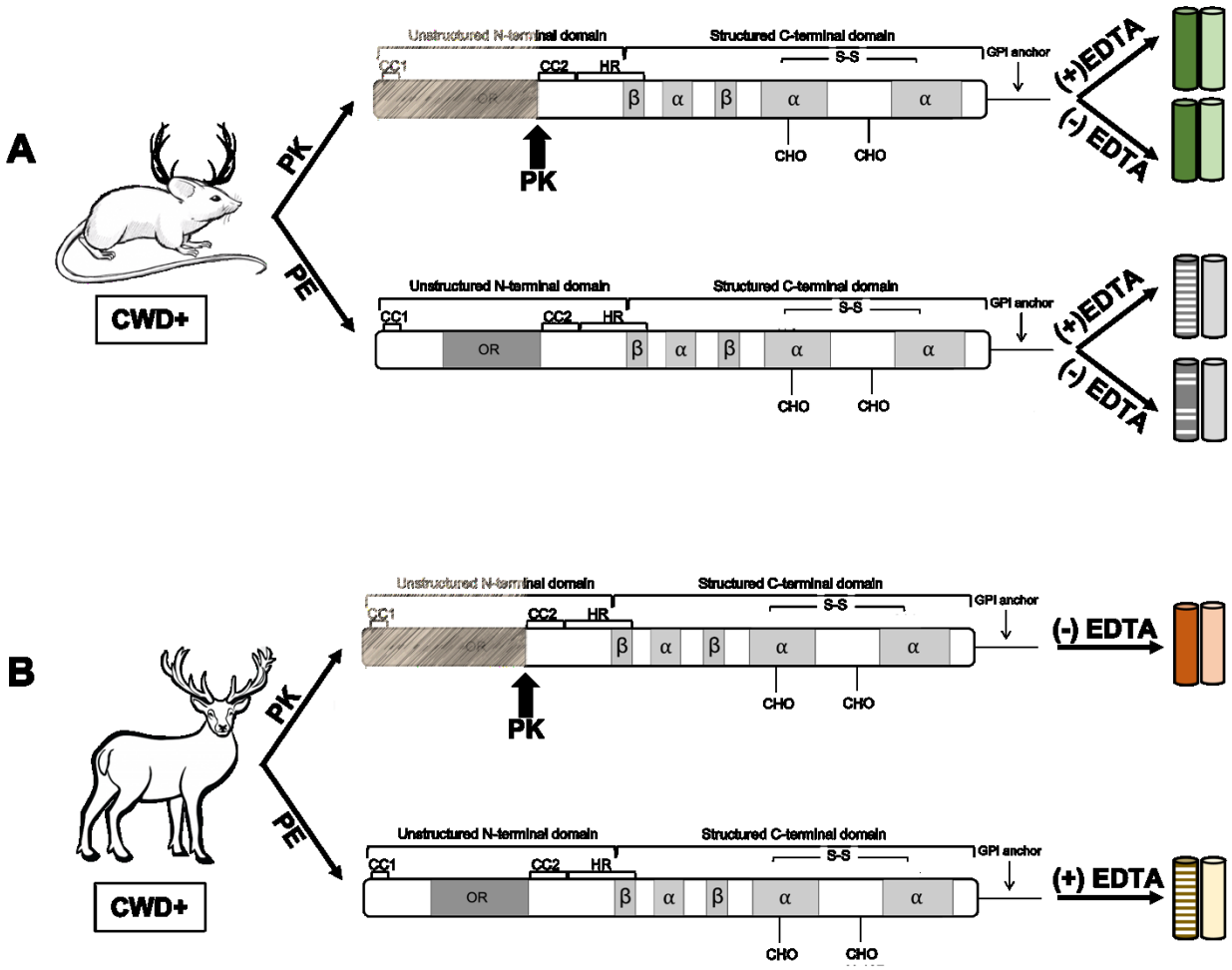

Figure 4-1. A summary illustration of the experimental study. Electron microscopy was used to examine the full-length and N-terminally truncated (PrP 27-30) structure of CWD prions purified from the brains of CWD-positive tg33 mice and white-tailed deer. CWD prions were found to be morphologically heterogeneous, with full-length prions displaying striations spaced approximately 3.5 nm apart. These striations were absent in the N-terminally truncated form, indicating their association with the N-terminal region of the prions. Treatment with EDTA improved the visualization of ordered striations in full-length CWD prions.

4.1.1 N-terminus of infectious prion: structured or unstructured?

The mature human PrP^C protein is composed of two domains: an unstructured N-terminal domain (residues 23-120, human numbering) and a structured C-terminal

domain (residues 121-231, human numbering) (Riek et al. 1996). High-resolution cryo EM structures of infectious prions have revealed that residues approximately 90 to 120 within the disordered N-terminal domain of PrP^C adopt a beta-strand conformation in the infectious form that is inaccessible to protease digestion (Caughey et al. 2023), including proteinase K and Pronase E. Meaning a previously unstructured sequence in PrP^C transforms into ordered and structured beta strands, exhibiting resistance to enzymatic digestion. The same reasoning can be extended to the remaining portion of the N-terminal domain, spanning residues approximately 23 to 90. Although high-resolution structural studies on full-length prions have not detected the presence of secondary structures such as beta strands in this region, investigations conducted by D'Castro and us demonstrate that Pronase E fails to digest residues ~ 23 to 90 (D'Castro et al. 2010). These findings suggest the existence of an ordered structure within this region, preventing the enzyme from interacting with and digesting it. In addition, our experimental findings reveal that the observed striations on the full-length CWD prions, likely corresponding to the N-terminal region, become discernible only after treating the samples with a chelating agent such as EDTA. Including EDTA during prion, purification may prevent the N-terminal region from interacting with copper ions, leading to potential conformational changes. This prevention of copper ion interactions allows the N-terminal region to interact with other segments of the prion structure, promoting stability and resulting in the manifestation of visible striations along the fibril. Consequently, to facilitate high-resolution studies on the N-terminal region, it is imperative to find a means of stabilizing the region prior to analysis.

4.1.2 Correlation of 3.8 nm striation spacing with the 4RβS and PIRIBS Models

To date, two distinct structural models for infectious prions have been proposed: the parallel in-register intermolecular β-sheet structure (Kraus et al. 2021, Hallinan et al. 2022, Hoyt et al. 2022, Hoyt et al. 2022, Manka et al. 2022, Manka et al. 2023) and the 4-rung beta solenoid model (Wille et al. 2002, Wille et al. 2009, Vázquez-Fernández et al. 2016, Spagnolli et al. 2019, Kamali-Jamil et al. 2021). The 4RβS model suggests a height of 19.2 Å per prion molecule, while the PIRIBS model showed monomers stacking in-register with a height of 4.9 Å per prion molecule. Both models were proposed for N-terminally truncated PrP. Thus, interpreting observations related to the spacing of striations potentially formed by the N-terminus may pose challenges due to this truncation.

However, assuming the presence of the N-terminus in these models, the head-to-head/tail-to-tail stacking of monomers in the 4RβS model would result in a spacing of 3.8 nm for the N-terminus, which closely aligns with the observed spacing of 3.3 to 3.7 nm of the striations in this study. In contrast, the hypothetical spacing of the N-terminus in a PIRIBS structure is 4.9 Å, which significantly differs from the observed striation spacing of 3.3 to 3.7 nm in this study. The observed spacing matches the spacing of every 8 monomers in a PIRIBS structure. Interestingly, thinner and less abundant 23-25 nm CWD fibrils, obtained through PE purification, were assumed to consist of a single protofilament. These fibrils did not exhibit striations, unlike the

thicker fibrils measuring 35 nm, where the striations were visible. The presence of multiple protofilaments and a diverse glycosylation pattern in these thicker fibrils adds complexity to their structure, making it challenging to decipher the arrangement of the N-terminus.

4.1.3 The importance of investigating the structure of infectious prions

Recently, high-resolution cryo EM structural studies have shed light on the adoption of the PIRIBS structure by some infectious prion structures, sharing several crucial structural motifs (Hoyt et al. 2022, Manka et al. 2023). However, even with identical amino acid sequences, the conformational details of these motifs vary among strains (Hoyt et al. 2022, Manka et al. 2023).

While the structures of many mammalian prion strains still await determination, elucidating their distinct structural properties holds great promise. Such knowledge will serve as a foundation for the development of innovative pharmacological strategies, including structural-based vaccine designs tailored to specific PrP^{Sc} conformations. Moreover, identifying key common confirmations among various PrP^{Sc} strains may even pave the way for the design of a universal vaccine.

In this regard, Dr. Andrew Fang, a member of our lab, has successfully designed a structural-based prion vaccine (Fang et al. 2022). Based on the proposed four-rung β-solenoid structure of PrP^{Sc}, the innocuous fungal prion HET-s was engineered to

mimic a surface epitope of PrP^{Sc}. Immunization of TgP101L transgenic mice, which overexpress mutant PrP carrying the murine equivalent of the P102L mutation and develop GSS disease symptoms at around 177 days of age, with the prion vaccine led to a significant delay in symptom onset. Compared to unimmunized TgP101L mice, the vaccinated group exhibited an increase in health span of approximately 260%, underscoring the remarkable protective effect of this model-based prion vaccine (Fang et al. 2022).

These findings provide evidence for the critical role of structural information concerning PrP^{Sc} and highlight the importance of such knowledge in the development of effective therapeutic interventions and preventive measures.

4.2 MOLECULAR DYNAMICS SIMULATIONS STUDY OF CERVID POLYMORPHISMS

The presence of cervid prion protein gene polymorphisms can influence the susceptibility of animals to chronic wasting disease (Arifin et al. 2021). Understanding how these polymorphisms affect the prion protein's structure is of great importance since these genetic variations can affect the behavior of the disease and possibly facilitate its spread from one species to another. Molecular dynamics simulation is a powerful technique that can provide insights into this process at the atomic level. Due to the limited number of polymorphisms studied using in silico and experimental

methods, the question of how these genetic variations affect prion protein folding remains unanswered.

In the second part of my Ph.D. project, I focused on exploring the impact of white-tailed deer prion protein polymorphisms on the structure and stability of PrP (Figure 4-2). Specifically, I conducted molecular dynamics simulations to investigate three cervid polymorphisms: 95H, 96S, and 116G. These three well-characterized white-tailed deer polymorphisms are associated with reduced susceptibility to CWD and/or delayed disease progression (Johnson et al. 2006, Hannaoui et al. 2017, Haley et al. 2019).

In summary, the 95H polymorphism exhibits a more ordered structure compared to the wild type form of the protein, leading to increased stability by reducing fluctuations in nearly all residues. Conversely, the 96S and 116G polymorphisms have the opposite effect. The polymorphisms are likely dictating their dynamic changes by altering hydrophobic interactions since their impact was more significant on the solvent-accessible surface area compared to hydrogen bonds and salt bridges. Moreover, analysis of distance maps reveals that the presence of these polymorphisms greatly affects the distances between residues in the protein structure. Specifically, the distances between residues associated with the 95H polymorphism are decreased compared to the WT, resulting in reduced flexibility in the main chain and increased stability, particularly in helix, helix2, helix3, and loop

Lα2α3. In contrast, these regions experience decreased stability and lost interactions in the case of 96S and 116G. Notably, the rigid loop (loop Lβ2α2) in the polymorphisms exhibits an altered correlation pattern compared to the WT. The assessment of the secondary structure revealed that the 116G polymorphism displays signs of structural disruption compared to the wild type construct. The 96S polymorphism only displays a slight elongation of its β1 and α3 regions, and the 95H construct demonstrates signs of α2 disruption and α3 elongation, along with the emergence of new beta bridge elements in its loop Lα2α3 region.

In conclusion, according to our MD simulation findings, the 95H polymorphism enhances the structural stability of the prion protein. Conversely, the 96S and 116G polymorphisms exhibit the opposite effect. The increased or decreased stability induced by these polymorphisms can potentially influence critical regions involved in the docking process with PrP^{Sc}, thereby impacting the efficiency of the misfolding process. These findings underscore the complex relationship between amino acid substitutions and their profound effects on disease susceptibility.

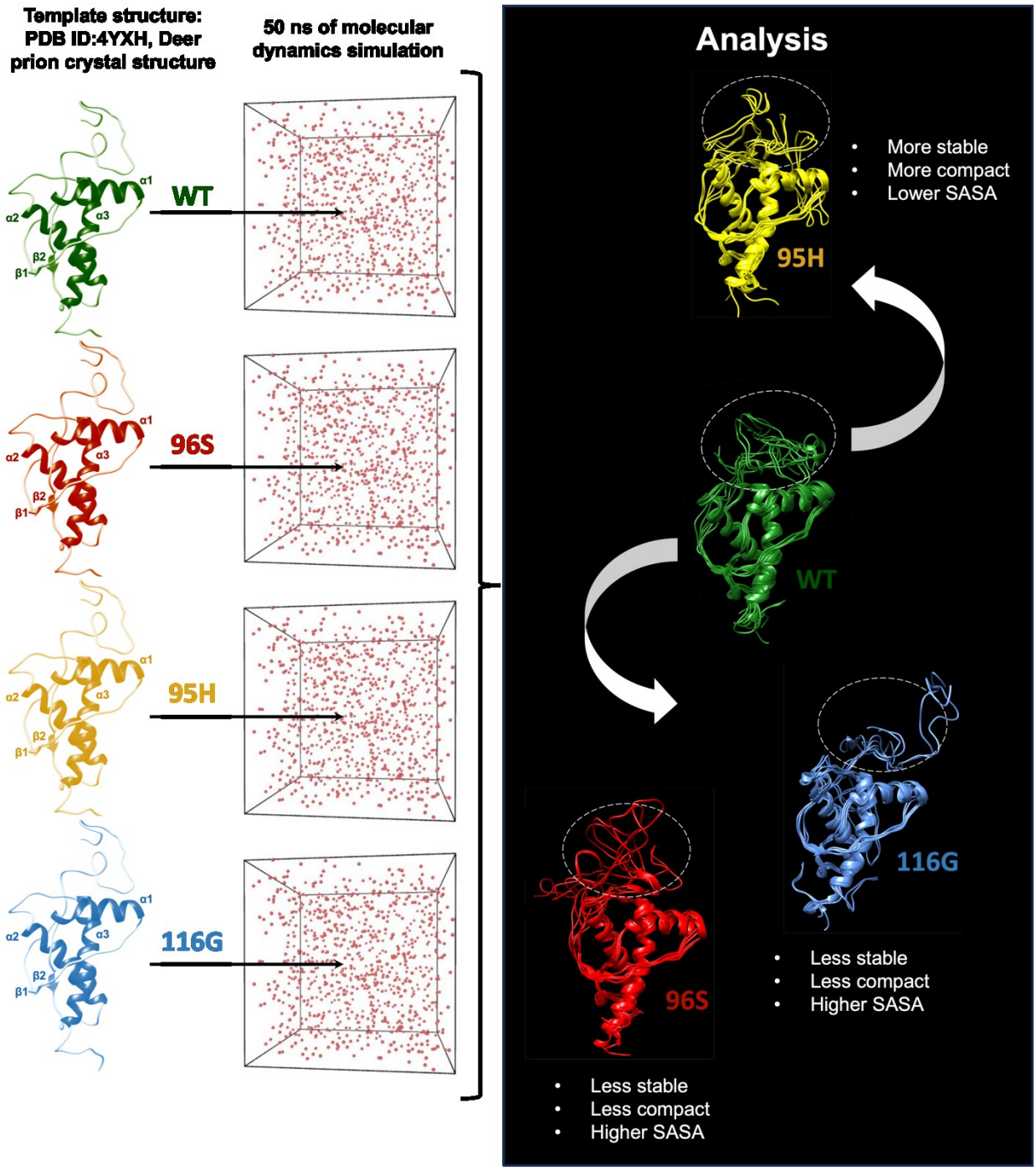

Figure 4-2. A summary illustration of the molecular dynamics simulations study. All-atom molecular dynamics simulations were performed to investigate the structure and stability of white-tailed deer PrP for wild type and three polymorphisms: 95H, 96S, and 116G. Analyzes demonstrated that proteins carrying polymorphisms display significant differences when compared to wild type construct.

4.2.1 The importance of decoding polymorphisms

Conducting more MD simulation studies on polymorphisms that influence disease susceptibility can greatly enhance our understanding of the correlation between amino acid substitutions and their observed effects in animals. By harnessing the knowledge gained from these studies, researchers can potentially design polymorphisms that confer resistance to the disease. Such efforts hold the potential to make significant contributions to disease prevention and management, including the design of breeding strategies to propagate resistant genotypes.

Farmers in Canada have proactively implemented breeding programs targeting animals with the 96SS polymorphism, which is linked to reduced susceptibility to chronic wasting disease. However, it is crucial to carefully consider the potential drawbacks and unintended consequences of this strategy. Notably, animals carrying the 96SS polymorphism exhibit an extended incubation time, increasing the risk of shedding infectious prions and potentially contributing to the spread of CWD within and between populations.

Thus, by joining the power of computational studies, and experimental validation, we can unlock the potential to design and propagate resistant polymorphisms, thereby safeguarding animal populations.

4.3 FUTURE DIRECTIONS

4.3.1 Future directions for studying the structure of CWD prions

The first part of my thesis research involved the structural investigation of full-length and N-terminally truncated (PrP 27-30) brain-derived, infectious chronic wasting disease prions. The results of my research provide evidence for distinct morphological variations in CWD prions, with a majority of the fibrils exhibiting larger fibril widths when compared to previously characterized prions. As a future direction of my thesis research, further investigations can be conducted using cryo electron microscopy to achieve higher-resolution information on the structural characteristics of brain-derived CWD prions. This approach would allow for a more detailed comparison of different prion strains, aiding in the understanding of species barriers. Furthermore, my research revealed that the N-terminal region (residues ~23 to 90) of CWD prions exhibits striations with a spacing of approximately 3.5 nm along the fibrils. By employing chelators like EDTA, it is possible to improve the ordering and visualization of the N-terminus, which is advantageous for structural studies. Therefore, a future direction involves exploring the effects of other chelators to optimize the quality of N-terminus ordering. Ultimately, the goal is to utilize cryo electron microscopy to obtain high-resolution information on the N-terminal region and enable a comparative analysis with truncated (PrP 27-30) structures. The comprehensive characterization of these morphological differences will contribute to a deeper understanding of CWD pathogenesis and aid in the development of targeted therapeutic strategies.

4.3.2 Future directions for MD simulation study

The second part of my thesis research focused on employing molecular dynamics simulations to investigate the impact of cervid polymorphisms on the structure of the prion protein. Specifically, I examined the well-studied polymorphisms 95H, 96S, and 116G, comparing them to the wild type construct. Through our simulations, we observed significant differences in the dynamic and conformational properties of the proteins carrying these polymorphisms when compared to the WT protein. Notably, the 95H polymorphism enhanced the structural stability of the prion protein, while the 96S and 116G polymorphisms exhibited the opposite effect. These findings highlight the complex relationship between amino acid substitutions and disease susceptibility, emphasizing the importance of understanding the structural implications of polymorphisms in prion diseases.

In future studies, it is essential to expand the scope of MD simulations to include a wider array of polymorphisms found in cervid PrP and other species, with a focus on understanding their effects on the disease phenotype. By elucidating the specific amino acid substitutions that govern disease outcomes, we can pave the way for the design of resistant polymorphisms that can be effectively utilized in breeding programs for animals.

REFERENCES

Adrian, M., J. Dubochet, J. Lepault and A. W. McDowall (1984). "Cryo-electron microscopy of viruses." Nature **308**(5954): 32-36.

Aguzzi, A., F. Baumann and J. Bremer (2008). "The prion's elusive reason for being." Annu Rev Neurosci **31**(1): 439-477.

Aguzzi, A., F. Montrasio and P. S. Kaeser (2001). "Prions: health scare and biological challenge." Nat Rev Mol Cell Biol **2**(2): 118-126.

Aguzzi, A., C. Sigurdson and M. Heikenwaelder (2008). "Molecular mechanisms of prion pathogenesis." Annu Rev Pathol **3**(1): 11-40.

Alper, T., W. A. Cramp, D. A. Haig and M. C. Clarke (1967). "Does the agent of scrapie replicate without nucleic acid?" Nature **214**(5090): 764-766.

Angers, R., J. Christiansen, A. V. Nalls, H. E. Kang, N. Hunter, E. Hoover, C. K. Mathiason, M. Sheetz and G. C. Telling (2014). "Structural effects of PrP polymorphisms on intra- and interspecies prion transmission." Proc Natl Acad Sci U S A **111**(30): 11169-11174.

Angers, R. C., S. R. Browning, T. S. Seward, C. J. Sigurdson, M. W. Miller, E. A. Hoover and G. C. Telling (2006). "Prions in skeletal muscles of deer with chronic wasting disease." Science **311**(5764): 1117.

Angers, R. C., H. E. Kang, D. Napier, S. Browning, T. Seward, C. Mathiason, A. Balachandran, D. McKenzie, J. Castilla, C. Soto, J. Jewell, C. Graham, E. A. Hoover and G. C. Telling (2010). "Prion strain mutation determined by prion protein conformational compatibility and primary structure." Science **328**(5982): 1154-1158.

Angers, R. C., T. S. Seward, D. Napier, M. Green, E. Hoover, T. Spraker, K. O'Rourke, A. Balachandran and G. C. Telling (2009). "Chronic wasting disease prions in elk antler velvet." Emerg Infect Dis **15**(5): 696-703.

Arifin, M. I., S. Hannaoui, S. C. Chang, S. Thapa, H. M. Schatzl and S. Gilch (2021). "Cervid Prion Protein Polymorphisms: Role in Chronic Wasting Disease Pathogenesis." Int J Mol Sci **22**(5): 2271.

Arnold, K., L. Bordoli, J. Kopp and T. Schwede (2006). "The SWISS-MODEL workspace: a web-based environment for protein structure homology modelling." Bioinformatics **22**(2): 195-201.

Arnot, C., E. Laate, J. Unterschultz and W. Adamowicz (2009). "Chronic wasting disease (CWD) potential economic impact on cervid farming in Alberta." J Toxicol Environ Health A **72**(17-18): 1014-1017.

Asante, E. A., M. Smidak, A. Grimshaw, R. Houghton, A. Tomlinson, A. Jeelani, T. Jakubcova, S. Hamdan, A. Richard-Londt, J. M. Linehan, S. Brandner, M. Alpers, J. Whitfield, S. Mead, J. D. Wadsworth and J. Collinge (2015). "A naturally occurring variant of the human prion protein completely prevents prion disease." Nature **522**(7557): 478-481.

Balbirnie, M., R. Grothe and D. S. Eisenberg (2001). "An amyloid-forming peptide from the yeast prion Sup35 reveals a dehydrated beta-sheet structure for amyloid." Proc Natl Acad Sci U S A **98**(5): 2375-2380.

Baral, P. K., M. Swayampakula, A. Aguzzi and M. N. James (2015). "X-ray structural and molecular dynamical studies of the globular domains of cow, deer, elk and Syrian hamster prion proteins." J Struct Biol **192**(1): 37-47.

Baron, T., A. Bencsik, A. G. Biacabe, E. Morignat and R. A. Bessen (2007). "Phenotypic similarity of transmissible mink encephalopathy in cattle and L-type bovine spongiform encephalopathy in a mouse model." Emerg Infect Dis **13**(12): 1887-1894.

Barria, M. A., G. C. Telling, P. Gambetti, J. A. Mastrianni and C. Soto (2011). "Generation of a new form of human PrP(Sc) in vitro by interspecies transmission from cervid prions." J Biol Chem **286**(9): 7490-7495.

Behmard, E., P. Abdolmaleki and E. B. Asadabadi (2012). "Mutation in a valine residue induces drastic changes in 3D structure of human prion protein." Frontiers in Life Science **6**(1-2): 47-51.

Benestad, S. L., J. N. Arsac, W. Goldmann and M. Noremark (2008). "Atypical/Nor98 scrapie: properties of the agent, genetics, and epidemiology." Vet Res **39**(4): 19.

Benestad, S. L., G. Mitchell, M. Simmons, B. Ytrehus and T. Vikoren (2016). "First case of chronic wasting disease in Europe in a Norwegian free-ranging reindeer." Vet Res **47**(1): 88.

Benestad, S. L., P. Sarradin, B. Thu, J. Schonheit, M. A. Tranulis and B. Bratberg (2003). "Cases of scrapie with unusual features in Norway and designation of a new type, Nor98." Vet Rec **153**(7): 202-208.

Benestad, S. L. and G. C. Telling (2018). Chronic wasting disease: an evolving prion disease of cervids. Handbook of Clinical Neurology, Elsevier. **153:** 135-151.

Berendsen, H. J. C., D. Vanderspoel and R. Vandrunen (1995). "Gromacs - a Message-Passing Parallel Molecular-Dynamics Implementation." Computer Physics Communications **91**(1-3): 43-56.

Bessen, R. A. and R. F. Marsh (1992). "Biochemical and physical properties of the prion protein from two strains of the transmissible mink encephalopathy agent." J Virol **66**(4): 2096-2101.

Bessen, R. A. and R. F. Marsh (1992). "Identification of two biologically distinct strains of transmissible mink encephalopathy in hamsters." J Gen Virol **73 (Pt 2)**: 329-334.

Biacabe, A. G., J. L. Laplanche, S. Ryder and T. Baron (2004). "Distinct molecular phenotypes in bovine prion diseases." EMBO Rep **5**(1): 110-115.

Biacabe, A. G., E. Morignat, J. Vulin, D. Calavas and T. G. Baron (2008). "Atypical bovine spongiform encephalopathies, France, 2001-2007." Emerg Infect Dis **14**(2): 298-300.

BIOVIA, D. S., Discovery Studio Modeling Enviroment, San Diego: Dassault Systèmes. (2017). from https://3ds.com/products-services/biovia/products.

Bocharova, O. V., L. Breydo, V. V. Salnikov and I. V. Baskakov (2005). "Copper(II) inhibits in vitro conversion of prion protein into amyloid fibrils." Biochemistry **44**(18): 6776-6787.

Bolton, D. C., M. P. McKinley and S. B. Prusiner (1982). "Identification of a protein that purifies with the scrapie prion." Science **218**(4579): 1309-1311.

Bounhar, Y., Y. Zhang, C. G. Goodyer and A. LeBlanc (2001). "Prion protein protects human neurons against Bax-mediated apoptosis." J Biol Chem **276**(42): 39145-39149.

Brandel, J. P., M. B. Vlaicu, A. Culeux, M. Belondrade, D. Bougard, K. Grznarova, A. Denouel, I. Plu, E. Bouaziz-Amar, D. Seilhean, M. Levasseur and S. Haik (2020). "Variant Creutzfeldt-Jakob Disease Diagnosed 7.5 Years after Occupational Exposure." N Engl J Med **383**(1): 83-85.

Bravard, A., F. Auvre, D. Fantini, J. Bernardino-Sgherri, L. Sissoeff, M. Daynac, Z. Xu, O. Etienne, C. Dehen, E. Comoy, F. D. Boussin, G. Tell, J. P. Deslys and J. P. Radicella (2015). "The prion protein is critical for DNA repair and cell survival after genotoxic stress." Nucleic Acids Res **43**(2): 904-916.

Bravo-Risi, F., P. Soto, T. Eckland, R. Dittmar, S. Ramirez, C. S. G. Catumbela, C. Soto, M. Lockwood, T. Nichols and R. Morales (2021). "Detection of CWD prions in naturally infected white-tailed deer fetuses and gestational tissues by PMCA." Sci Rep **11**(1): 18385.

Brayton, K. A., K. I. O'Rourke, A. K. Lyda, M. W. Miller and D. P. Knowles (2004). "A processed pseudogene contributes to apparent mule deer prion gene heterogeneity." Gene **326**: 167-173.

Bremer, J., F. Baumann, C. Tiberi, C. Wessig, H. Fischer, P. Schwarz, A. D. Steele, K. V. Toyka, K. A. Nave, J. Weis and A. Aguzzi (2010). "Axonal prion protein is required for peripheral myelin maintenance." Nat Neurosci **13**(3): 310-318.

Brown, D. R., W. J. Schulz-Schaeffer, B. Schmidt and H. A. Kretzschmar (1997). "Prion protein-deficient cells show altered response to oxidative stress due to decreased SOD-1 activity." Exp Neurol **146**(1): 104-112.

Brown, D. R., B. S. Wong, F. Hafiz, C. Clive, S. J. Haswell and I. M. Jones (1999). "Normal prion protein has an activity like that of superoxide dismutase." Biochemical Journal **344**(Pt 1): 1-5.

Brown, L. R. and D. A. Harris (2003). "Copper and zinc cause delivery of the prion protein from the plasma membrane to a subset of early endosomes and the Golgi." J Neurochem **87**(2): 353-363.

Brown, P. and R. Bradley (1998). "1755 and all that: a historical primer of transmissible spongiform encephalopathy." BMJ **317**(7174): 1688-1692.

Brown, P., J. P. Brandel, T. Sato, Y. Nakamura, J. MacKenzie, R. G. Will, A. Ladogana, M. Pocchiari, E. W. Leschek and L. B. Schonberger (2012). "Iatrogenic Creutzfeldt-Jakob disease, final assessment." Emerg Infect Dis **18**(6): 901-907.

Brown, P., R. G. Will, R. Bradley, D. M. Asher and L. Detwiler (2001). "Bovine spongiform encephalopathy and variant Creutzfeldt-Jakob disease: background, evolution, and current concerns." Emerg Infect Dis **7**(1): 6-16.

Bruce, M. E., R. G. Will, J. W. Ironside, I. McConnell, D. Drummond, A. Suttie, L. McCardle, A. Chree, J. Hope, C. Birkett, S. Cousens, H. Fraser and C. J. Bostock (1997). "Transmissions to mice indicate that 'new variant' CJD is caused by the BSE agent." Nature **389**(6650): 498-501.

Callaway, E. (2015). "The revolution will not be crystallized: a new method sweeps through structural biology." Nature **525**(7568): 172-174.

Carta, M. and A. Aguzzi (2022). "Molecular foundations of prion strain diversity." Curr Opin Neurobiol **72**: 22-31.

Casalone, C., G. Zanusso, P. Acutis, S. Ferrari, L. Capucci, F. Tagliavini, S. Monaco and M. Caramelli (2004). "Identification of a second bovine amyloidotic spongiform encephalopathy: molecular similarities with sporadic Creutzfeldt-Jakob disease." Proc Natl Acad Sci U S A **101**(9): 3065-3070.

Cassard, H., J. M. Torres, C. Lacroux, J. Y. Douet, S. L. Benestad, F. Lantier, S. Lugan, I. Lantier, P. Costes, N. Aron, F. Reine, L. Herzog, J. C. Espinosa, V. Beringue and O. Andreoletti (2014). "Evidence for zoonotic potential of ovine scrapie prions." Nat Commun **5**: 5821.

Cassmann, E. D. and J. J. Greenlee (2020). "Pathogenesis, detection, and control of scrapie in sheep." Am J Vet Res **81**(7): 600-614.

Caughey, B., E. Artikis and A. Kraus (2023). PrP Prion Structures. Prions and Diseases. W.-Q. Zou and P. Gambetti. Cham, Springer International Publishing**:** 45-62.

Caughey, B. W., A. Dong, K. S. Bhat, D. Ernst, S. F. Hayes and W. S. Caughey (1991). "Secondary structure analysis of the scrapie-associated protein PrP 27-30 in water by infrared spectroscopy." Biochemistry **30**(31): 7672-7680.

Chandrasekaran, P. and R. Rajasekaran (2016). "Detailed computational analysis revealed mutation V210I on PrP induced conformational conversion on beta2-alpha2 loop and alpha2-alpha3." Mol Biosyst **12**(10): 3223-3233.

Chebaro, Y. and P. Derreumaux (2009). "The conversion of helix H2 to beta-sheet is accelerated in the monomer and dimer of the prion protein upon T183A mutation." J Phys Chem B **113**(19): 6942-6948.

Chiavacci, S. J. (2022). "The economic costs of chronic wasting disease in the United States." PLoS One **17**(12): e0278366.

Chida, J., H. Hara, M. Yano, K. Uchiyama, N. R. Das, E. Takahashi, H. Miyata, Y. Tomioka, T. Ito, H. Kido and S. Sakaguchi (2018). "Prion protein protects mice from lethal infection with influenza A viruses." PLoS Pathog **14**(5): e1007049.

Cobb, N. J., F. D. Sonnichsen, H. McHaourab and W. K. Surewicz (2007). "Molecular architecture of human prion protein amyloid: a parallel, in-register beta-structure." Proc Natl Acad Sci U S A **104**(48): 18946-18951.

Cohen, F. E., K. M. Pan, Z. Huang, M. Baldwin, R. J. Fletterick and S. B. Prusiner (1994). "Structural clues to prion replication." Science **264**(5158): 530-531.

Colby, D. W. and S. B. Prusiner (2011). "Prions." Cold Spring Harb Perspect Biol **3**(1): a006833.

Colby, D. W., R. Wain, I. V. Baskakov, G. Legname, C. G. Palmer, H. O. Nguyen, A. Lemus, F. E. Cohen, S. J. DeArmond and S. B. Prusiner (2010). "Protease-sensitive synthetic prions." PLoS Pathog **6**(1): e1000736.

Collinge, J., M. S. Palmer and A. J. Dryden (1991). "Genetic predisposition to iatrogenic Creutzfeldt-Jakob disease." Lancet **337**(8755): 1441-1442.

Collinge, J., K. C. Sidle, J. Meads, J. Ironside and A. F. Hill (1996). "Molecular analysis of prion strain variation and the aetiology of 'new variant' CJD." Nature **383**(6602): 685-690.

Collinge, J., J. Whitfield, E. McKintosh, J. Beck, S. Mead, D. J. Thomas and M. P. Alpers (2006). "Kuru in the 21st century--an acquired human prion disease with very long incubation periods." Lancet **367**(9528): 2068-2074.

Come, J. H., P. E. Fraser and P. T. Lansbury, Jr. (1993). "A kinetic model for amyloid formation in the prion diseases: importance of seeding." Proc Natl Acad Sci U S A **90**(13): 5959-5963.

Comoy, E. E., J. Mikol, S. Luccantoni-Freire, E. Correia, N. Lescoutra-Etchegaray, V. Durand, C. Dehen, O. Andreoletti, C. Casalone, J. A. Richt, J. J. Greenlee, T. Baron, S. L. Benestad, P. Brown and J. P. Deslys (2015). "Transmission of scrapie prions to primate after an extended silent incubation period." Sci Rep **5**(1): 11573.

Cong, X., N. Casiraghi, G. Rossetti, S. Mohanty, G. Giachin, G. Legname and P. Carloni (2013). "Role of Prion Disease-Linked Mutations in the Intrinsically Disordered N-Terminal Domain of the Prion Protein." J Chem Theory Comput **9**(11): 5158-5167.

Cortez, L. M., J. Kumar, L. Renault, H. S. Young and V. L. Sim (2013). "Mouse Prion Protein Polymorphism Phe-108/Val-189 Affects the Kinetics of Fibril Formation and the Response to Seeding." Journal of Biological Chemistry **288**(7): 4772-4781.

Creutzfeldt, H. G. (1920). "Über eine eigenartige herdförmige erkrankung des zentralnervensystems (Vorläufige mitteilung)." Zeitschrift für die gesamte Neurologie und Psychiatrie **57**(1): 1-18.

D'Castro, L., A. Wenborn, N. Gros, S. Joiner, S. Cronier, J. Collinge and J. D. Wadsworth (2010). "Isolation of proteinase K-sensitive prions using pronase E and phosphotungstic acid." PLoS One **5**(12): e15679.

Das, N. R., H. Miyata, H. Hara, J. Chida, K. Uchiyama, K. Masujin, H. Watanabe, G. Kondoh and S. Sakaguchi (2020). "The N-Terminal Polybasic Region of Prion Protein Is Crucial in Prion Pathogenesis Independently of the Octapeptide Repeat Region." Mol Neurobiol **57**(2): 1203-1216.

De Carlo, S. and J. R. Harris (2011). "Negative staining and cryo-negative staining of macromolecules and viruses for TEM." Micron **42**(2): 117-131.

Dill, K. A. and J. L. MacCallum (2012). "The protein-folding problem, 50 years on." Science **338**(6110): 1042-1046.

Doss, C. G., B. Rajith, R. Rajasekaran, J. Srajan, N. Nagasundaram and C. Debajyoti (2013). "In silico analysis of prion protein mutants: a comparative study by molecular dynamics approach." Cell Biochem Biophys **67**(3): 1307-1318.

Dubochet, J., J. Lepault, R. Freeman, J. A. Berriman and J. C. Homo (1982). "Electron-Microscopy of Frozen Water and Aqueous-Solutions." Journal of Microscopy **128**(Dec): 219-237.

Duffy, P., J. Wolf, G. Collins, A. G. DeVoe, B. Streeten and D. Cowen (1974). "Letter: Possible person-to-person transmission of Creutzfeldt-Jakob disease." N Engl J Med **290**(12): 692-693.

Duque Velasquez, C., C. Kim, T. Haldiman, C. Kim, A. Herbst, J. Aiken, J. G. Safar and D. McKenzie (2020). "Chronic wasting disease (CWD) prion strains evolve via adaptive diversification of conformers in hosts expressing prion protein polymorphisms." J Biol Chem **295**(15): 4985-5001.

Duque Velasquez, C., C. Kim, A. Herbst, N. Daude, M. C. Garza, H. Wille, J. Aiken and D. McKenzie (2015). "Deer Prion Proteins Modulate the Emergence and Adaptation of Chronic Wasting Disease Strains." J Virol **89**(24): 12362-12373.

Ebeling, W., N. Hennrich, M. Klockow, H. Metz, H. D. Orth and H. Lang (1974). "Proteinase K from Tritirachium album Limber." Eur J Biochem **47**(1): 91-97.

Eisenberg, D. S. and M. R. Sawaya (2017). "Structural Studies of Amyloid Proteins at the Molecular Level." Annu Rev Biochem **86**(1): 69-95.

Eisenhaber, B., P. Bork and F. Eisenhaber (1998). "Sequence properties of GPI-anchored proteins near the omega-site: constraints for the polypeptide binding site of the putative transamidase." Protein Eng **11**(12): 1155-1161.

Eisenhaber, B., P. Bork and F. Eisenhaber (1999). "Prediction of potential GPI-modification sites in proprotein sequences." J Mol Biol **292**(3): 741-758.

Eisenhaber, B., P. Bork, Y. Yuan, G. Loffler and F. Eisenhaber (2000). "Automated annotation of GPI anchor sites: case study C. elegans." Trends Biochem Sci **25**(7): 340-341.

Eklund, C. M., R. C. Kennedy and W. J. Hadlow (1967). "Pathogenesis of scrapie virus infection in the mouse." J Infect Dis **117**(1): 15-22.

Evans, E. G., M. J. Pushie, K. A. Markham, H. W. Lee and G. L. Millhauser (2016). "Interaction between Prion Protein's Copper-Bound Octarepeat Domain and a Charged C-Terminal Pocket Suggests a Mechanism for N-Terminal Regulation." Structure **24**(7): 1057-1067.

Fang, A., M. Fleming, B. Tancowny, X. L. Tang and H. Wille (2022). "A structure-based prion vaccine protects a transgenic mouse model of Gerstmann-Straussler-Scheinker disease from neurodegeneration." Biophysical Journal **121**(3): 154a-154a.

Fitzpatrick, A. W., G. T. Debelouchina, M. J. Bayro, D. K. Clare, M. A. Caporini, V. S. Bajaj, C. P. Jaroniec, L. Wang, V. Ladizhansky, S. A. Muller, C. E. MacPhee, C. A. Waudby, H. R. Mott, A. De Simone, T. P. Knowles, H. R. Saibil, M. Vendruscolo, E. V. Orlova, R. G. Griffin and C. M. Dobson (2013). "Atomic structure and hierarchical assembly of a cross-beta amyloid fibril." Proc Natl Acad Sci U S A **110**(14): 5468-5473.

Flechsig, E., D. Shmerling, I. Hegyi, A. J. Raeber, M. Fischer, A. Cozzio, C. von Mering, A. Aguzzi and C. Weissmann (2000). "Prion protein devoid of the octapeptide repeat region restores susceptibility to scrapie in PrP knockout mice." Neuron **27**(2): 399-408.

Flores-Fernández, J. M., V. Rathod and H. Wille (2018). "Comparing the Folds of Prions and Other Pathogenic Amyloids." Pathogens **7**(2): 50.

Fox, K. A., J. E. Jewell, E. S. Williams and M. W. Miller (2006). "Patterns of PrPCWD accumulation during the course of chronic wasting disease infection in orally inoculated mule deer (Odocoileus hemionus)." J Gen Virol **87**(Pt 11): 3451-3461.

Frank, J., M. Radermacher, P. Penczek, J. Zhu, Y. Li, M. Ladjadj and A. Leith (1996). "SPIDER and WEB: processing and visualization of images in 3D electron microscopy and related fields." J Struct Biol **116**(1): 190-199.

Gajdusek, D. C., C. J. Gibbs and M. Alpers (1965). "Slow, latent and temperate virus infections." Slow, latent and temperate virus infections.

Gambetti, P., P. Parchi, R. B. Petersen, S. G. Chen and E. Lugaresi (1995). "Fatal familial insomnia and familial Creutzfeldt-Jakob disease: clinical, pathological and molecular features." Brain Pathol **5**(1): 43-51.

Gerstmann, J., E. Sträussler and I. Scheinker (1935). "Über eine eigenartige hereditär- familiäre Erkrankung des Zentralnervensystems." Zeitschrift für die gesamte Neurologie und Psychiatrie **154**(1): 736-762.

Gibbs, C. J., Jr., D. M. Asher, A. Kobrine, H. L. Amyx, M. P. Sulima and D. C. Gajdusek (1994). "Transmission of Creutzfeldt-Jakob disease to a chimpanzee by electrodes contaminated during neurosurgery." J Neurol Neurosurg Psychiatry **57**(6): 757-758.

Gibbs, C. J., Jr. and D. C. Gajdusek (1973). "Experimental subacute spongiform virus encephalopathies in primates and other laboratory animals." Science **182**(4107): 67-68.

Gibbs, C. J., Jr., D. C. Gajdusek and R. Latarjet (1978). "Unusual resistance to ionizing radiation of the viruses of kuru, Creutzfeldt-Jakob disease, and scrapie." Proc Natl Acad Sci U S A **75**(12): 6268-6270.

Gill, O. N., Y. Spencer, A. Richard-Loendt, C. Kelly, D. Brown, K. Sinka, N. Andrews, R. Dabaghian, M. Simmons, P. Edwards, P. Bellerby, D. J. Everest, M. McCall, L. M. McCardle, J. Linehan, S. Mead, D. A. Hilton, J. W. Ironside and S. Brandner (2020). "Prevalence in Britain of abnormal prion protein in human appendices before and after exposure to the cattle BSE epizootic." Acta Neuropathol **139**(6): 965-976.

Goldfarb, L. G., A. D. Korczyn, P. Brown, J. Chapman and D. C. Gajdusek (1990). "Mutation in codon 200 of scrapie amyloid precursor gene linked to Creutzfeldt-Jakob

disease in Sephardic Jews of Libyan and non-Libyan origin." Lancet **336**(8715): 637-638.

Goldfarb, L. G., R. B. Petersen, M. Tabaton, P. Brown, A. C. LeBlanc, P. Montagna, P. Cortelli, J. Julien, C. Vital, W. W. Pendelbury and et al. (1992). "Fatal familial insomnia and familial Creutzfeldt-Jakob disease: disease phenotype determined by a DNA polymorphism." Science **258**(5083): 806-808.

Goldgaber, D., L. G. Goldfarb, P. Brown, D. M. Asher, W. T. Brown, S. Lin, J. W. Teener, S. M. Feinstone, R. Rubenstein, R. J. Kascsak and et al. (1989). "Mutations in familial Creutzfeldt-Jakob disease and Gerstmann-Straussler-Scheinker's syndrome." Exp Neurol **106**(2): 204-206.

Goldmann, W., N. Hunter, G. Smith, J. Foster and J. Hope (1994). "PrP genotype and agent effects in scrapie: change in allelic interaction with different isolates of agent in sheep, a natural host of scrapie." J Gen Virol **75 (Pt 5)**: 989-995.

Gossert, A. D., S. Bonjour, D. A. Lysek, F. Fiorito and K. Wuthrich (2005). "Prion protein NMR structures of elk and of mouse/elk hybrids." Proc Natl Acad Sci U S A **102**(3): 646-650.

Govaerts, C., H. Wille, S. B. Prusiner and F. E. Cohen (2004). "Evidence for assembly of prions with left-handed beta-helices into trimers." Proc Natl Acad Sci U S A **101**(22): 8342-8347.

Greenlee, J. J. and M. H. Greenlee (2015). "The transmissible spongiform encephalopathies of livestock." ILAR J **56**(1): 7-25.

Guo, J., L. Ning, H. Ren, H. Liu and X. Yao (2012). "Influence of the pathogenic mutations T188K/R/A on the structural stability and misfolding of human prion protein: insight from molecular dynamics simulations." Biochim Biophys Acta **1820**(2): 116-123.

Habenstein, B. and A. Loquet (2016). "Solid-state NMR: An emerging technique in structural biology of self-assemblies." Biophys Chem **210**: 14-26.

Hadlow, W. J. (1959). "Scrapie and Kuru." Lancet **2**(Sep5): 289-290.

Haigh, C. L., S. C. Drew, M. P. Boland, C. L. Masters, K. J. Barnham, V. A. Lawson and S. J. Collins (2009). "Dominant roles of the polybasic proline motif and copper in the PrP23-89-mediated stress protection response." J Cell Sci **122**(Pt 10): 1518-1528.

Haley, N. J., C. K. Mathiason, M. D. Zabel, G. C. Telling and E. A. Hoover (2009). "Detection of sub-clinical CWD infection in conventional test-negative deer long after oral exposure to urine and feces from CWD+ deer." PLoS One **4**(11): e7990.

Haley, N. J., K. Merrett, A. Buros Stein, D. Simpson, A. Carlson, G. Mitchell, A. Staskevicius, T. Nichols, A. D. Lehmkuhl and B. V. Thomsen (2019). "Estimating relative CWD susceptibility and disease progression in farmed white-tailed deer with rare PRNP alleles." PLoS One **14**(12): e0224342.

Haley, N. J., C. Siepker, W. D. Walter, B. V. Thomsen, J. J. Greenlee, A. D. Lehmkuhl and J. A. Richt (2016). "Antemortem Detection of Chronic Wasting Disease Prions in Nasal Brush Collections and Rectal Biopsy Specimens from White-Tailed Deer by Real-Time Quaking-Induced Conversion." J Clin Microbiol **54**(4): 1108-1116.

Hallinan, G. I., K. A. Ozcan, M. R. Hoq, L. Cracco, F. S. Vago, S. R. Bharath, D. Li, M. Jacobsen, E. H. Doud, A. L. Mosley, A. Fernandez, H. J. Garringer, W. Jiang, B. Ghetti and R. Vidal (2022). "Cryo-EM structures of prion protein filaments from Gerstmann-Straussler-Scheinker disease." Acta Neuropathol **144**(3): 509-520.

Hannaoui, S., S. Amidian, Y. C. Cheng, C. Duque Velasquez, L. Dorosh, S. Law, G. Telling, M. Stepanova, D. McKenzie, H. Wille and S. Gilch (2017). "Destabilizing polymorphism in cervid prion protein hydrophobic core determines prion conformation and conversion efficiency." PLoS Pathog **13**(8): e1006553.

Hannaoui, S., E. Triscott, C. Duque Velasquez, S. C. Chang, M. I. Arifin, I. Zemlyankina, X. Tang, T. Bollinger, H. Wille, D. McKenzie and S. Gilch (2021). "New and distinct chronic wasting disease strains associated with cervid polymorphism at codon 116 of the Prnp gene." PLoS Pathog **17**(7): e1009795.

Hannaoui, S., I. Zemlyankina, S. C. Chang, M. I. Arifin, V. Beringue, D. McKenzie, H. M. Schatzl and S. Gilch (2022). "Transmission of cervid prions to humanized mice demonstrates the zoonotic potential of CWD." Acta Neuropathol **144**(4): 767-784.

Hara, H. and S. Sakaguchi (2020). "N-Terminal Regions of Prion Protein: Functions and Roles in Prion Diseases." Int J Mol Sci **21**(17): 6233.

Hartsough, G. R. and D. Burger (1965). "Encephalopathy of mink. I. Epizootiologic and clinical observations." J Infect Dis **115**(4): 387-392.

Heaton, M. P., K. A. Leymaster, B. A. Freking, D. A. Hawk, T. P. Smith, J. W. Keele, W. M. Snelling, J. M. Fox, C. G. Chitko-McKown and W. W. Laegreid (2003). "Prion gene sequence variation within diverse groups of U.S. sheep, beef cattle, and deer." Mamm Genome **14**(11): 765-777.

Hess, B., D. van der Spoel, E. Lindahl and a. t. G. d. team (2014). GROMACS User Manual version 4.6.7.

Hijazi, N., Y. Shaked, H. Rosenmann, T. Ben-Hur and R. Gabizon (2003). "Copper binding to PrPC may inhibit prion disease propagation." Brain Res **993**(1-2): 192-200.

Hill, A. F., M. Desbruslais, S. Joiner, K. C. Sidle, I. Gowland, J. Collinge, L. J. Doey and P. Lantos (1997). "The same prion strain causes vCJD and BSE." Nature **389**(6650): 448-450, 526.

Hornshaw, M. P., J. R. McDermott, J. M. Candy and J. H. Lakey (1995). "Copper binding to the N-terminal tandem repeat region of mammalian and avian prion protein: structural studies using synthetic peptides." Biochem Biophys Res Commun **214**(3): 993-999.

Hoyt, F., P. Alam, E. Artikis, C. L. Schwartz, A. G. Hughson, B. Race, C. Baune, G. J. Raymond, G. S. Baron, A. Kraus and B. Caughey (2022). "Cryo-EM of prion strains from the same genotype of host identifies conformational determinants." PLoS Pathog **18**(11): e1010947.

Hoyt, F., H. G. Standke, E. Artikis, C. L. Schwartz, B. Hansen, K. Li, A. G. Hughson, M. Manca, O. R. Thomas, G. J. Raymond, B. Race, G. S. Baron, B. Caughey and A. Kraus (2022). "Cryo-EM structure of anchorless RML prion reveals variations in shared motifs between distinct strains." Nat Commun **13**(1): 4005.

Hsiao, K., H. F. Baker, T. J. Crow, M. Poulter, F. Owen, J. D. Terwilliger, D. Westaway, J. Ott and S. B. Prusiner (1989). "Linkage of a prion protein missense variant to Gerstmann-Straussler syndrome." Nature **338**(6213): 342-345.

Hubbard, S. J. (1998). "The structural aspects of limited proteolysis of native proteins." Biochim Biophys Acta **1382**(2): 191-206.

Humphrey, W., A. Dalke and K. Schulten (1996). "VMD: visual molecular dynamics." J Mol Graph **14**(1): 33-38, 27-38.

Hunter, N., J. D. Foster, W. Goldmann, M. J. Stear, J. Hope and C. Bostock (1996). "Natural scrapie in a closed flock of Cheviot sheep occurs only in specific PrP genotypes." Arch Virol **141**(5): 809-824.

Huson, H. J. and G. M. Happ (2006). "Polymorphisms of the prion protein gene (PRNP) in Alaskan moose (Alces alces gigas)." Anim Genet **37**(4): 425-426.

Iadanza, M. G., M. P. Jackson, E. W. Hewitt, N. A. Ranson and S. E. Radford (2018). "A new era for understanding amyloid structures and disease." Nat Rev Mol Cell Biol **19**(12): 755-773.

Jahandideh, S., M. Jamalan and M. Faridounnia (2015). "Molecular dynamics study of the dominant-negative E219K polymorphism in human prion protein." J Biomol Struct Dyn **33**(6): 1315-1325.

Jakob, A. (1921). "Über eigenartige erkrankungen des zentralnervensystems mit bemerkenswertem anatomischen befunde." Zeitschrift für die gesamte Neurologie und Psychiatrie **64**(1): 147-228.

Jarrett, J. T. and P. T. Lansbury, Jr. (1993). "Seeding "one-dimensional crystallization" of amyloid: a pathogenic mechanism in Alzheimer's disease and scrapie?" Cell **73**(6): 1055-1058.

Jewell, J. E., J. Brown, T. Kreeger and E. S. Williams (2006). "Prion protein in cardiac muscle of elk (Cervus elaphus nelsoni) and white-tailed deer (Odocoileus virginianus) infected with chronic wasting disease." J Gen Virol **87**(Pt 11): 3443-3450.

Jewell, J. E., M. M. Conner, L. L. Wolfe, M. W. Miller and E. S. Williams (2005). "Low frequency of PrP genotype 225SF among free-ranging mule deer (Odocoileus hemionus) with chronic wasting disease." J Gen Virol **86**(Pt 8): 2127-2134.

Johnson, C., J. Johnson, M. Clayton, D. McKenzie and J. Aiken (2003). "Prion protein gene heterogeneity in free-ranging white-tailed deer within the chronic wasting disease affected region of Wisconsin." J Wildl Dis **39**(3): 576-581.

Johnson, C., J. Johnson, J. P. Vanderloo, D. Keane, J. M. Aiken and D. McKenzie (2006). "Prion protein polymorphisms in white-tailed deer influence susceptibility to chronic wasting disease." J Gen Virol **87**(Pt 7): 2109-2114.

Johnson, C. J., A. Herbst, C. Duque-Velasquez, J. P. Vanderloo, P. Bochsler, R. Chappell and D. McKenzie (2011). "Prion protein polymorphisms affect chronic wasting disease progression." PLoS One **6**(3): e17450.

Johnson, C. J., J. A. Pedersen, R. J. Chappell, D. McKenzie and J. M. Aiken (2007). "Oral transmissibility of prion disease is enhanced by binding to soil particles." PLoS Pathog **3**(7): e93.

Jones, C. E., S. R. Abdelraheim, D. R. Brown and J. H. Viles (2004). "Preferential Cu2+ coordination by His96 and His111 induces beta-sheet formation in the unstructured amyloidogenic region of the prion protein." J Biol Chem **279**(31): 32018-32027.

Jones, S., M. Batchelor, D. Bhelt, A. R. Clarke, J. Collinge and G. S. Jackson (2005). "Recombinant prion protein does not possess SOD-1 activity." Biochem J **392**(Pt 2): 309-312.

Jorgensen, W. L., D. S. Maxwell and J. TiradoRives (1996). "Development and testing of the OPLS all-atom force field on conformational energetics and properties of organic liquids." Journal of the American Chemical Society **118**(45): 11225-11236.

Kahn, S., C. Dube, L. Bates and A. Balachandran (2004). "Chronic wasting disease in Canada: Part 1." Can Vet J **45**(5): 397-404.

Kamali-Jamil, R., E. Vazquez-Fernandez, B. Tancowny, V. Rathod, S. Amidian, X. Wang, X. Tang, A. Fang, A. Senatore, S. Hornemann, S. Dudas, A. Aguzzi, H. S. Young and H. Wille (2021). "The ultrastructure of infectious L-type bovine spongiform encephalopathy prions constrains molecular models." PLoS Pathog **17**(6): e1009628.

Kanaani, J., S. B. Prusiner, J. Diacovo, S. Baekkeskov and G. Legname (2005). "Recombinant prion protein induces rapid polarization and development of synapses in embryonic rat hippocampal neurons in vitro." J Neurochem **95**(5): 1373-1386.

Keane, D. P., D. J. Barr, P. N. Bochsler, S. M. Hall, T. Gidlewski, K. I. O'Rourke, T. R. Spraker and M. D. Samuel (2008). "Chronic wasting disease in a Wisconsin white-tailed deer farm." J Vet Diagn Invest **20**(5): 698-703.

Klamt, F., F. Dal-Pizzol, M. L. Conte da Frota, Jr., R. Walz, M. E. Andrades, E. G. da Silva, R. R. Brentani, I. Izquierdo and J. C. Fonseca Moreira (2001). "Imbalance of antioxidant defense in mice lacking cellular prion protein." Free Radic Biol Med **30**(10): 1137-1144.

Klatzo, I., D. C. Gajdusek and V. Zigas (1959). "Pathology of Kuru." Lab Invest **8**(4): 799-847.

Kong, Q., S. Huang, W. Zou, D. Vanegas, M. Wang, D. Wu, J. Yuan, M. Zheng, H. Bai, H. Deng, K. Chen, A. L. Jenny, K. O'Rourke, E. D. Belay, L. B. Schonberger, R. B. Petersen, M. S. Sy, S. G. Chen and P. Gambetti (2005). "Chronic wasting disease of elk: transmissibility to humans examined by transgenic mouse models." J Neurosci **25**(35): 7944-7949.

Kovač, V. and V. Čurin Šerbec (2022). "Prion Protein: The Molecule of Many Forms and Faces." Int J Mol Sci **23**(3): 1232.

Kovačs, G. G., M. Puopolo, A. Ladogana, M. Pocchiari, H. Budka, C. van Duijn, S. J. Collins, A. Boyd, A. Giulivi, M. Coulthart, N. Delasnerie-Laupretre, J. P. Brandel, I. Zerr, H. A. Kretzschmar, J. de Pedro-Cuesta, M. Calero-Lara, M. Glatzel, A. Aguzzi, M. Bishop, R. Knight, G. Belay, R. Will, E. Mitrova and Eurocjd (2005). "Genetic prion disease: the EUROCJD experience." Hum Genet **118**(2): 166-174.

Kraus, A., F. Hoyt, C. L. Schwartz, B. Hansen, E. Artikis, A. G. Hughson, G. J. Raymond, B. Race, G. S. Baron and B. Caughey (2021). "High-resolution structure and strain comparison of infectious mammalian prions." Mol Cell **81**(21): 4540-4551 e4546.

Kurt, T. D., C. Bett, N. Fernandez-Borges, S. Joshi-Barr, S. Hornemann, T. Rulicke, J. Castilla, K. Wuthrich, A. Aguzzi and C. J. Sigurdson (2014). "Prion transmission prevented by modifying the beta2-alpha2 loop structure of host PrPC." J Neurosci **34**(3): 1022-1027.

Kurt, T. D., L. Jiang, N. Fernandez-Borges, C. Bett, J. Liu, T. Yang, T. R. Spraker, J. Castilla, D. Eisenberg, Q. Kong and C. J. Sigurdson (2015). "Human prion protein sequence elements impede cross-species chronic wasting disease transmission." J Clin Invest **125**(4): 1485-1496.

Kuznetsova, A., D. McKenzie, P. Banser, T. Siddique and J. M. Aiken (2014). "Potential role of soil properties in the spread of CWD in western Canada." Prion **8**(1): 92-99.

Kuznetsova, A., D. McKenzie, C. Cullingham and J. M. Aiken (2020). "Long-Term Incubation PrP(CWD) with Soils Affects Prion Recovery but Not Infectivity." Pathogens **9**(4): 311.

Ladogana, A., M. Puopolo, E. A. Croes, H. Budka, C. Jarius, S. Collins, G. M. Klug, T. Sutcliffe, A. Giulivi, A. Alperovitch, N. Delasnerie-Laupretre, J. P. Brandel, S. Poser, H. Kretzschmar, I. Rietveld, E. Mitrova, P. Cuesta Jde, P. Martinez-Martin, M. Glatzel, A. Aguzzi, R. Knight, H. Ward, M. Pocchiari, C. M. van Duijn, R. G. Will and I. Zerr (2005). "Mortality from Creutzfeldt-Jakob disease and related disorders in Europe, Australia, and Canada." Neurology **64**(9): 1586-1591.

Lasmézas, C. I., J. P. Deslys, O. Robain, A. Jaegly, V. Beringue, J. M. Peyrin, J. G. Fournier, J. J. Hauw, J. Rossier and D. Dormont (1997). "Transmission of the BSE agent to mice in the absence of detectable abnormal prion protein." Science **275**(5298): 402-405.

Lee, I. S., J. R. Long, S. B. Prusiner and J. G. Safar (2005). "Selective Precipitation of Prions by Polyoxometalate Complexes." Journal of the American Chemical Society **127**(40): 13802-13803.

Leffers, K. W., H. Wille, J. Stohr, E. Junger, S. B. Prusiner and D. Riesner (2005). "Assembly of natural and recombinant prion protein into fibrils." Biol Chem **386**(6): 569-580.

Legname, G., I. V. Baskakov, H. O. Nguyen, D. Riesner, F. E. Cohen, S. J. DeArmond and S. B. Prusiner (2004). "Synthetic mammalian prions." Science **305**(5684): 673-676.

Levine, D. J., J. Stöhr, L. E. Falese, J. Ollesch, H. Wille, S. B. Prusiner and J. R. Long (2015). "Mechanism of Scrapie Prion Precipitation with Phosphotungstate Anions." ACS Chemical Biology **10**(5): 1269-1277.

Liemann, S. and R. Glockshuber (1999). "Influence of amino acid substitutions related to inherited human prion diseases on the thermodynamic stability of the cellular prion protein." Biochemistry **38**(11): 3258-3267.

Lopez Garcia, F., R. Zahn, R. Riek and K. Wuthrich (2000). "NMR structure of the bovine prion protein." Proc Natl Acad Sci U S A **97**(15): 8334-8339.

Loquet, A., N. El Mammeri, J. Stanek, M. Berbon, B. Bardiaux, G. Pintacuda and B. Habenstein (2018). "3D structure determination of amyloid fibrils using solid-state NMR spectroscopy." Methods **138-139**: 26-38.

Ludtke, S. J., P. R. Baldwin and W. Chiu (1999). "EMAN: semiautomated software for high-resolution single-particle reconstructions." J Struct Biol **128**(1): 82-97.

Lugaresi, E., R. Medori, P. Montagna, A. Baruzzi, P. Cortelli, A. Lugaresi, P. Tinuper, M. Zucconi and P. Gambetti (1986). "Fatal familial insomnia and dysautonomia with selective degeneration of thalamic nuclei." N Engl J Med **315**(16): 997-1003.

Lysek, D. A., C. Schorn, L. G. Nivon, V. Esteve-Moya, B. Christen, L. Calzolai, C. von Schroetter, F. Fiorito, T. Herrmann, P. Guntert and K. Wuthrich (2005). "Prion protein NMR structures of cats, dogs, pigs, and sheep." Proc Natl Acad Sci U S A **102**(3): 640-645.

Mackerell, A. D., Jr. (2004). "Empirical force fields for biological macromolecules: overview and issues." J Comput Chem **25**(13): 1584-1604.

Makau, D. N., K. VanderWaal, J. Kincheloe and S. J. Wells (2020). "Implications of farmed-cervid movements on the transmission of chronic wasting disease." Prev Vet Med **182**: 105088.

Manka, S. W., A. Wenborn, J. Betts, S. Joiner, H. R. Saibil, J. Collinge and J. D. F. Wadsworth (2023). "A structural basis for prion strain diversity." Nat Chem Biol **19**(5): 607-613.

Manka, S. W., A. Wenborn, J. Collinge and J. D. F. Wadsworth (2023). "Prion strains viewed through the lens of cryo-EM." Cell Tissue Res **392**(1): 167-178.

Manka, S. W., W. Zhang, A. Wenborn, J. Betts, S. Joiner, H. R. Saibil, J. Collinge and J. D. F. Wadsworth (2022). "2.7 A cryo-EM structure of ex vivo RML prion fibrils." Nat Commun **13**(1): 4004.

Marsh, R. F., R. A. Bessen, S. Lehmann and G. R. Hartsough (1991). "Epidemiological and experimental studies on a new incident of transmissible mink encephalopathy." J Gen Virol **72 (Pt 3)**: 589-594.

Marsh, R. F., D. Burger, R. Eckroade, G. M. Zu Rhein and R. P. Hanson (1969). "A preliminary report on the experimental host range of the transmissible mink encephalopathy agent." J Infect Dis **120**(6): 713-719.

Masters, C. L., J. O. Harris, D. C. Gajdusek, C. J. Gibbs, Jr., C. Bernoulli and D. M. Asher (1979). "Creutzfeldt-Jakob disease: patterns of worldwide occurrence and the significance of familial and sporadic clustering." Ann Neurol **5**(2): 177-188.

Mathiason, C. K., J. G. Powers, S. J. Dahmes, D. A. Osborn, K. V. Miller, R. J. Warren, G. L. Mason, S. A. Hays, J. Hayes-Klug, D. M. Seelig, M. A. Wild, L. L. Wolfe, T. R. Spraker, M. W. Miller, C. J. Sigurdson, G. C. Telling and E. A. Hoover (2006). "Infectious prions in the saliva and blood of deer with chronic wasting disease." Science **314**(5796): 133-136.

McDonald, A. J., D. R. Leon, K. A. Markham, B. Wu, C. F. Heckendorf, K. Schilling, H. D. Showalter, P. C. Andrews, M. E. McComb, M. J. Pushie, C. E. Costello, G. L. Millhauser and D. A. Harris (2019). "Altered Domain Structure of the Prion Protein Caused by Cu(2+) Binding and Functionally Relevant Mutations: Analysis by Cross-Linking, MS/MS, and NMR." Structure **27**(6): 907-922 e905.

Mead, S., J. Whitfield, M. Poulter, P. Shah, J. Uphill, T. Campbell, H. Al-Dujaily, H. Hummerich, J. Beck, C. A. Mein, C. Verzilli, J. Whittaker, M. P. Alpers and J. Collinge (2009). "A novel protective prion protein variant that colocalizes with kuru exposure." N Engl J Med **361**(21): 2056-2065.

Meade-White, K., B. Race, M. Trifilo, A. Bossers, C. Favara, R. Lacasse, M. Miller, E. Williams, M. Oldstone, R. Race and B. Chesebro (2007). "Resistance to chronic wasting disease in transgenic mice expressing a naturally occurring allelic variant of deer prion protein." J Virol **81**(9): 4533-4539.

Medori, R., H. J. Tritschler, A. LeBlanc, F. Villare, V. Manetto, H. Y. Chen, R. Xue, S. Leal, P. Montagna, P. Cortelli and et al. (1992). "Fatal familial insomnia, a prion disease with a mutation at codon 178 of the prion protein gene." N Engl J Med **326**(7): 444-449.

Meli, M., M. Gasset and G. Colombo (2011). "Dynamic diagnosis of familial prion diseases supports the beta2-alpha2 loop as a universal interference target." PLoS One **6**(4): e19093.

Merz, P. A., R. A. Somerville, H. M. Wisniewski and K. Iqbal (1981). "Abnormal fibrils from scrapie-infected brain." Acta Neuropathol **54**(1): 63-74.

Miller, M. W. and E. S. Williams (2003). "Prion disease: horizontal prion transmission in mule deer." Nature **425**(6953): 35-36.

Miller, M. W. and E. S. Williams (2004). "Chronic wasting disease of cervids." Curr Top Microbiol Immunol **284**: 193-214.

Miller, M. W., E. S. Williams, N. T. Hobbs and L. L. Wolfe (2004). "Environmental sources of prion transmission in mule deer." Emerg Infect Dis **10**(6): 1003-1006.

Miller, M. W., E. S. Williams, C. W. McCarty, T. R. Spraker, T. J. Kreeger, C. T. Larsen and E. T. Thorne (2000). "Epizootiology of chronic wasting disease in free-ranging cervids in Colorado and Wyoming." J Wildl Dis **36**(4): 676-690.

Millhauser, G. L. (2023). The Rich Chemistry of the Copper and Zinc Sites in PrPC. Prions and Diseases. W.-Q. Zou and P. Gambetti. Cham, Springer International Publishing**:** 25-43.

Mitteregger, G., M. Vosko, B. Krebs, W. Xiang, V. Kohlmannsperger, S. Nolting, G. F. Hamann and H. A. Kretzschmar (2007). "The role of the octarepeat region in neuroprotective function of the cellular prion protein." Brain Pathol **17**(2): 174-183.

Moore, J., T. Tatum, S. Hwang, C. Vrentas, M. H. West Greenlee, Q. Kong, E. Nicholson and J. Greenlee (2020). "Novel Strain of the Chronic Wasting Disease Agent Isolated From Experimentally Inoculated Elk With LL132 Prion Protein." Sci Rep **10**(1): 3148.

Moore, R. A., L. M. Taubner and S. A. Priola (2009). "Prion protein misfolding and disease." Curr Opin Struct Biol **19**(1): 14-22.

Moore, S. J., M. Simmons, M. Chaplin and J. Spiropoulos (2008). "Neuroanatomical distribution of abnormal prion protein in naturally occurring atypical scrapie cases in Great Britain." Acta Neuropathol **116**(5): 547-559.

Moore, S. J., C. E. Vrentas, S. Hwang, M. H. West Greenlee, E. M. Nicholson and J. J. Greenlee (2018). "Pathologic and biochemical characterization of PrP(Sc) from elk with PRNP polymorphisms at codon 132 after experimental infection with the chronic wasting disease agent." BMC Vet Res **14**(1): 80.

Müller, H., O. Brener, O. Andreoletti, T. Piechatzek, D. Willbold, G. Legname and H. Heise (2014). "Progress towards structural understanding of infectious sheep PrP-amyloid." Prion **8**(5): 344-358.

Nalls, A. V., E. E. McNulty, A. Mayfield, J. M. Crum, M. K. Keel, E. A. Hoover, M. G. Ruder and C. K. Mathiason (2021). "Detection of Chronic Wasting Disease Prions in Fetal Tissues of Free-Ranging White-Tailed Deer." Viruses **13**(12): 2430.

Nathanson, N., J. Wilesmith and C. Griot (1997). "Bovine spongiform encephalopathy (BSE): causes and consequences of a common source epidemic." Am J Epidemiol **145**(11): 959-969.

Nečas, D. and P. Klapetek (2012). "Gwyddion: an open-source software for SPM data analysis." Open Physics **10**(1).

Nonno, R., M. A. Di Bari, L. Pirisinu, C. D'Agostino, I. Vanni, B. Chiappini, S. Marcon, G. Riccardi, L. Tran, T. Vikoren, J. Vage, K. Madslien, G. Mitchell, G. C. Telling, S. L. Benestad and U. Agrimi (2020). "Studies in bank voles reveal strain differences between chronic wasting disease prions from Norway and North America." Proc Natl Acad Sci U S A **117**(49): 31417-31426.

O'Rourke, K. I., T. E. Besser, M. W. Miller, T. F. Cline, T. R. Spraker, A. L. Jenny, M. A. Wild, G. L. Zebarth and E. S. Williams (1999). "PrP genotypes of captive and free-ranging Rocky Mountain elk (Cervus elaphus nelsoni) with chronic wasting disease." J Gen Virol **80 (Pt 10)**: 2765-2679.

O'Rourke, K. I., T. R. Spraker, L. K. Hamburg, T. E. Besser, K. A. Brayton and D. P. Knowles (2004). "Polymorphisms in the prion precursor functional gene but not the pseudogene are associated with susceptibility to chronic wasting disease in white-tailed deer." J Gen Virol **85**(Pt 5): 1339-1346.

O'Rourke, K. I., T. R. Spraker, D. Zhuang, J. J. Greenlee, T. E. Gidlewski and A. N. Hamir (2007). "Elk with a long incubation prion disease phenotype have a unique PrPd profile." Neuroreport **18**(18): 1935-1938.

Oh, J. M., H. Y. Shin, S. J. Park, B. H. Kim, J. K. Choi, E. K. Choi, R. I. Carp and Y. S. Kim (2008). "The involvement of cellular prion protein in the autophagy pathway in neuronal cells." Mol Cell Neurosci **39**(2): 238-247.

Orlova, E. V. and H. R. Saibil (2011). "Structural analysis of macromolecular assemblies by electron microscopy." Chem Rev **111**(12): 7710-7748.

Osiecka, K. M., H. Nieznanska, K. J. Skowronek, J. Karolczak, G. Schneider and K. Nieznanski (2009). "Prion protein region 23-32 interacts with tubulin and inhibits microtubule assembly." Proteins **77**(2): 279-296.

Otero, A., C. Duque Velasquez, C. Johnson, A. Herbst, R. Bolea, J. J. Badiola, J. Aiken and D. McKenzie (2019). "Prion protein polymorphisms associated with reduced CWD susceptibility limit peripheral PrP(CWD) deposition in orally infected white-tailed deer." BMC Vet Res **15**(1): 50.

Otero, A., C. Duque Velasquez, D. McKenzie and J. Aiken (2023). "Emergence of CWD strains." Cell Tissue Res **392**(1): 135-148.

Otero, A., C. D. Velasquez, J. Aiken and D. McKenzie (2021). "Chronic wasting disease: a cervid prion infection looming to spillover." Vet Res **52**(1): 115.

Palmer, M. S., A. J. Dryden, J. T. Hughes and J. Collinge (1991). "Homozygous prion protein genotype predisposes to sporadic Creutzfeldt-Jakob disease." Nature **352**(6333): 340-342.

Pan, K.-M., M. Baldwin, J. Nguyen, M. Gasset, I. Mehlhorn, Z. Huang, R. J. Fletterick, F. E. Cohenu and S. B. Prusiner (1993). "Conversion of a-helices into ,f-sheets features in the formation of the scrapie prion proteins." Proc. Natl. Acad. Sci. USA: 5.

Pan, T., B. S. Wong, T. Liu, R. Li, R. B. Petersen and M. S. Sy (2002). "Cell-surface prion protein interacts with glycosaminoglycans." Biochem J **368**(Pt 1): 81-90.

Parkin, E. T., N. T. Watt, I. Hussain, E. A. Eckman, C. B. Eckman, J. C. Manson, H. N. Baybutt, A. J. Turner and N. M. Hooper (2007). "Cellular prion protein regulates beta-secretase cleavage of the Alzheimer's amyloid precursor protein." Proc Natl Acad Sci U S A **104**(26): 11062-11067.

Parlee, B., K. Ahkimnachie, H. Cunningham, M. Jordan and E. Goddard (2021). ""“It’s important to know about this” - risk communication and the impacts of chronic wasting disease on indigenous food systems in Western Canada." Environmental Science & Policy **123**: 190-201.

Pastrana, M. A., G. Sajnani, B. Onisko, J. Castilla, R. Morales, C. Soto and J. R. Requena (2006). "Isolation and characterization of a proteinase K-sensitive PrPSc fraction." Biochemistry **45**(51): 15710-15717.

Pauly, P. C. and D. A. Harris (1998). "Copper stimulates endocytosis of the prion protein." J Biol Chem **273**(50): 33107-33110.

Perez, D. R., F. F. Damberger and K. Wuthrich (2010). "Horse prion protein NMR structure and comparisons with related variants of the mouse prion protein." J Mol Biol **400**(2): 121-128.

Petigara, M., C. Dridi and J. Unterschultz (2011). "The economic impacts of chronic wasting disease and bovine spongiform encephalopathy in alberta and the rest of Canada." J Toxicol Environ Health A **74**(22-24): 1609-1620.

Pettersen, E. F., T. D. Goddard, C. C. Huang, G. S. Couch, D. M. Greenblatt, E. C. Meng and T. E. Ferrin (2004). "UCSF Chimera--a visualization system for exploratory research and analysis." J Comput Chem **25**(13): 1605-1612.

Piana, S., J. L. Klepeis and D. E. Shaw (2014). "Assessing the accuracy of physical models used in protein-folding simulations: quantitative evidence from long molecular dynamics simulations." Curr Opin Struct Biol **24**: 98-105.

Pirisinu, L., L. Tran, B. Chiappini, I. Vanni, M. A. Di Bari, G. Vaccari, T. Vikoren, K. I. Madslien, J. Vage, T. Spraker, G. Mitchell, A. Balachandran, T. Baron, C. Casalone, C. M. Rolandsen, K. H. Roed, U. Agrimi, R. Nonno and S. L. Benestad (2018). "Novel Type of Chronic Wasting Disease Detected in Moose (Alces alces), Norway." Emerg Infect Dis **24**(12): 2210-2218.

Pritzkow, S. (2022). "Transmission, Strain Diversity, and Zoonotic Potential of Chronic Wasting Disease." Viruses **14**(7): 1390.

Prusiner, S. B. (1982). "Novel proteinaceous infectious particles cause scrapie." Science **216**(4542): 136-144.

Prusiner, S. B. (1998). "Prions." Proc Natl Acad Sci U S A **95**(23): 13363-13383.

Prusiner, S. B., D. C. Bolton, D. F. Groth, K. A. Bowman, S. P. Cochran and M. P. McKinley (1982). "Further purification and characterization of scrapie prions." Biochemistry **21**(26): 6942-6950.

Prusiner, S. B., M. P. McKinley, K. A. Bowman, D. C. Bolton, P. E. Bendheim, D. F. Groth and G. G. Glenner (1983). "Scrapie prions aggregate to form amyloid-like birefringent rods." Cell **35**(2 Pt 1): 349-358.

Prusiner, S. B., M. Scott, D. Foster, K. M. Pan, D. Groth, C. Mirenda, M. Torchia, S. L. Yang, D. Serban, G. A. Carlson and et al. (1990). "Transgenetic studies implicate

interactions between homologous PrP isoforms in scrapie prion replication." Cell **63**(4): 673-686.

Prusiner, S. B., M. R. Scott, S. J. DeArmond and F. E. Cohen (1998). "Prion protein biology." Cell **93**(3): 337-348.

Race, B., K. Meade-White, M. W. Miller, K. A. Fox and B. Chesebro (2011). "In vivo comparison of chronic wasting disease infectivity from deer with variation at prion protein residue 96." J Virol **85**(17): 9235-9238.

Race, B., K. D. Meade-White, M. W. Miller, K. D. Barbian, R. Rubenstein, G. LaFauci, L. Cervenakova, C. Favara, D. Gardner, D. Long, M. Parnell, J. Striebel, S. A. Priola, A. Ward, E. S. Williams, R. Race and B. Chesebro (2009). "Susceptibilities of nonhuman primates to chronic wasting disease." Emerg Infect Dis **15**(9): 1366-1376.

Race, B., K. D. Meade-White, K. Phillips, J. Striebel, R. Race and B. Chesebro (2014). "Chronic wasting disease agents in nonhuman primates." Emerg Infect Dis **20**(5): 833-837.

Race, B., K. Williams and B. Chesebro (2019). "Transmission studies of chronic wasting disease to transgenic mice overexpressing human prion protein using the RT-QuIC assay." Vet Res **50**(1): 6.

Race, B., K. Williams, C. D. Orru, A. G. Hughson, L. Lubke and B. Chesebro (2018). "Lack of Transmission of Chronic Wasting Disease to Cynomolgus Macaques." J Virol **92**(14): e00550-00518.

Rahman, A., B. Saikia, C. R. Gogoi and A. Baruah (2022). "Advances in the understanding of protein misfolding and aggregation through molecular dynamics simulation." Prog Biophys Mol Biol **175**: 31-48.

Raymond, G. J., A. Bossers, L. D. Raymond, K. I. O'Rourke, L. E. McHolland, P. K. Bryant, 3rd, M. W. Miller, E. S. Williams, M. Smits and B. Caughey (2000). "Evidence of a molecular barrier limiting susceptibility of humans, cattle and sheep to chronic wasting disease." EMBO J **19**(17): 4425-4430.

Riek, R. and D. S. Eisenberg (2016). "The activities of amyloids from a structural perspective." Nature **539**(7628): 227-235.

Riek, R., S. Hornemann, G. Wider, M. Billeter, R. Glockshuber and K. Wuthrich (1996). "NMR structure of the mouse prion protein domain PrP(121-231)." Nature **382**(6587): 180-182.

Riesner, D. (2003). "Biochemistry and structure of PrP(C) and PrP(Sc)." Br Med Bull **66**: 21-33.

Robinson, S. J., M. D. Samuel, K. I. O'Rourke and C. J. Johnson (2012). "The role of genetics in chronic wasting disease of North American cervids." Prion **6**(2): 153-162.

Rose, P. W., A. Prlic, A. Altunkaya, C. Bi, A. R. Bradley, C. H. Christie, L. D. Costanzo, J. M. Duarte, S. Dutta, Z. Feng, R. K. Green, D. S. Goodsell, B. Hudson, T. Kalro, R. Lowe, E. Peisach, C. Randle, A. S. Rose, C. Shao, Y. P. Tao, Y. Valasatava, M. Voigt, J. D. Westbrook, J. Woo, H. Yang, J. Y. Young, C. Zardecki, H. M. Berman and S. K. Burley (2017). "The RCSB protein data bank: integrative view of protein, gene and 3D structural information." Nucleic Acids Res **45**(D1): D271-D281.

Rossetti, G., X. Cong, R. Caliandro, G. Legname and P. Carloni (2011). "Common structural traits across pathogenic mutants of the human prion protein and their implications for familial prion diseases." J Mol Biol **411**(3): 700-712.

Safar, J., P. P. Roller, D. C. Gajdusek and C. J. Gibbs, Jr. (1993). "Conformational transitions, dissociation, and unfolding of scrapie amyloid (prion) protein." J Biol Chem **268**(27): 20276-20284.

Safar, J., H. Wille, V. Itri, D. Groth, H. Serban, M. Torchia, F. E. Cohen and S. B. Prusiner (1998). "Eight prion strains have PrP(Sc) molecules with different conformations." Nat Med **4**(10): 1157-1165.

Safar, J. G., M. D. Geschwind, C. Deering, S. Didorenko, M. Sattavat, H. Sanchez, A. Serban, M. Vey, H. Baron, K. Giles, B. L. Miller, S. J. Dearmond and S. B. Prusiner (2005). "Diagnosis of human prion disease." Proceedings of the National Academy of Sciences **102**(9): 3501-3506.

Sajnani, G., M. A. Pastrana, I. Dynin, B. Onisko and J. R. Requena (2008). "Scrapie prion protein structural constraints obtained by limited proteolysis and mass spectrometry." J Mol Biol **382**(1): 88-98.

Sajnani, G., C. J. Silva, A. Ramos, M. A. Pastrana, B. C. Onisko, M. L. Erickson, E. M. Antaki, I. Dynin, E. Vazquez-Fernandez, C. J. Sigurdson, J. M. Carter and J. R. Requena (2012). "PK-sensitive PrP is infectious and shares basic structural features with PK-resistant PrP." PLoS Pathog **8**(3): e1002547.

Salzano, G., G. Giachin and G. Legname (2019). "Structural Consequences of Copper Binding to the Prion Protein." Cells **8**(8): 770.

Sandberg, M. K., H. Al-Doujaily, C. J. Sigurdson, M. Glatzel, C. O'Malley, C. Powell, E. A. Asante, J. M. Linehan, S. Brandner, J. D. Wadsworth and J. Collinge (2010). "Chronic wasting disease prions are not transmissible to transgenic mice overexpressing human prion protein." J Gen Virol **91**(Pt 10): 2651-2657.

Sawaya, M. R., S. Sambashivan, R. Nelson, M. I. Ivanova, S. A. Sievers, M. I. Apostol, M. J. Thompson, M. Balbirnie, J. J. Wiltzius, H. T. McFarlane, A. O. Madsen, C. Riekel and D. Eisenberg (2007). "Atomic structures of amyloid cross-beta spines reveal varied steric zippers." Nature **447**(7143): 453-457.

Schätzl, H. M., F. Wopfner, S. Gilch, A. von Brunn and G. Jager (1997). "Is codon 129 of prion protein polymorphic in human beings but not in animals?" Lancet **349**(9065): 1603-1604.

Senatore, A., K. Frontzek, M. Emmenegger, A. Chincisan, M. Losa, R. Reimann, G. Horny, J. Guo, S. Fels, S. Sorce, C. Zhu, N. George, S. Ewert, T. Pietzonka, S. Hornemann and A. Aguzzi (2020). "Protective anti-prion antibodies in human immunoglobulin repertoires." EMBO Mol Med **12**(9): e12739.

Shannon, M. D., T. Theint, D. Mukhopadhyay, K. Surewicz, W. K. Surewicz, D. Marion, P. Schanda and C. P. Jaroniec (2019). "Conformational Dynamics in the Core of Human Y145Stop Prion Protein Amyloid Probed by Relaxation Dispersion NMR." Chemphyschem **20**(2): 311-317.

Shen, P. S. (2018). "The 2017 Nobel Prize in Chemistry: cryo-EM comes of age." Anal Bioanal Chem **410**(8): 2053-2057.

Shi, Y. (2014). "A glimpse of structural biology through X-ray crystallography." Cell **159**(5): 995-1014.

Sigurdson, C. J., K. P. Nilsson, S. Hornemann, M. Heikenwalder, G. Manco, P. Schwarz, D. Ott, T. Rulicke, P. P. Liberski, C. Julius, J. Falsig, L. Stitz, K. Wuthrich and A. Aguzzi (2009). "De novo generation of a transmissible spongiform encephalopathy by mouse transgenesis." Proc Natl Acad Sci U S A **106**(1): 304-309.

Sigurdson, C. J., K. P. Nilsson, S. Hornemann, G. Manco, N. Fernandez-Borges, P. Schwarz, J. Castilla, K. Wuthrich and A. Aguzzi (2010). "A molecular switch controls interspecies prion disease transmission in mice." J Clin Invest **120**(7): 2590-2599.

Sigurdson, C. J., T. R. Spraker, M. W. Miller, B. Oesch and E. A. Hoover (2001). "PrP(CWD) in the myenteric plexus, vagosympathetic trunk and endocrine glands of deer with chronic wasting disease." J Gen Virol **82**(Pt 10): 2327-2334.

Sigurdson, C. J., E. S. Williams, M. W. Miller, T. R. Spraker, K. I. O'Rourke and E. A. Hoover (1999). "Oral transmission and early lymphoid tropism of chronic wasting disease PrPres in mule deer fawns (Odocoileus hemionus)." J Gen Virol **80 (Pt 10)**: 2757-2764.

Sigurdsson, E. M., D. R. Brown, M. A. Alim, H. Scholtzova, R. Carp, H. C. Meeker, F. Prelli, B. Frangione and T. Wisniewski (2003). "Copper chelation delays the onset of prion disease." J Biol Chem **278**(47): 46199-46202.

Sim, V. L. and B. Caughey (2009). "Ultrastructures and strain comparison of under-glycosylated scrapie prion fibrils." Neurobiol Aging **30**(12): 2031-2042.

Smirnovas, V., G. S. Baron, D. K. Offerdahl, G. J. Raymond, B. Caughey and W. K. Surewicz (2011). "Structural organization of brain-derived mammalian prions examined by hydrogen-deuterium exchange." Nat Struct Mol Biol **18**(4): 504-506.

Soto, C. (2009). "Constraining the loop, releasing prion infectivity." Proc Natl Acad Sci U S A **106**(1): 10-11.

Spagnolli, G., M. Rigoli, S. Orioli, A. M. Sevillano, P. Faccioli, H. Wille, E. Biasini and J. R. Requena (2019). "Full atomistic model of prion structure and conversion." PLoS Pathog **15**(7): e1007864.

Spraker, T. R., M. W. Miller, E. S. Williams, D. M. Getzy, W. J. Adrian, G. G. Schoonveld, R. A. Spowart, K. I. O'Rourke, J. M. Miller and P. A. Merz (1997). "Spongiform encephalopathy in free-ranging mule deer (Odocoileus hemionus), white-tailed deer (Odocoileus virginianus) and Rocky Mountain elk (Cervus elaphus nelsoni) in northcentral Colorado." J Wildl Dis **33**(1): 1-6.

Stahl, N., D. R. Borchelt, K. Hsiao and S. B. Prusiner (1987). "Scrapie prion protein contains a phosphatidylinositol glycolipid." Cell **51**(2): 229-240.

Sunde, M., L. C. Serpell, M. Bartlam, P. E. Fraser, M. B. Pepys and C. C. Blake (1997). "Common core structure of amyloid fibrils by synchrotron X-ray diffraction." J Mol Biol **273**(3): 729-739.

Supattapone, S., T. Muramoto, G. Legname, I. Mehlhorn, F. E. Cohen, S. J. DeArmond, S. B. Prusiner and M. R. Scott (2001). "Identification of two prion protein regions that modify scrapie incubation time." J Virol **75**(3): 1408-1413.

Tamgüney, G., K. Giles, E. Bouzamondo-Bernstein, P. J. Bosque, M. W. Miller, J. Safar, S. J. DeArmond and S. B. Prusiner (2006). "Transmission of elk and deer prions to transgenic mice." J Virol **80**(18): 9104-9114.

Tamgüney, G., M. W. Miller, L. L. Wolfe, T. M. Sirochman, D. V. Glidden, C. Palmer, A. Lemus, S. J. DeArmond and S. B. Prusiner (2009). "Asymptomatic deer excrete infectious prions in faeces." Nature **461**(7263): 529-532.

Taylor, K. A. and R. M. Glaeser (1976). "Electron microscopy of frozen hydrated biological specimens." J Ultrastruct Res **55**(3): 448-456.

Telling, G. C., P. Parchi, S. J. DeArmond, P. Cortelli, P. Montagna, R. Gabizon, J. Mastrianni, E. Lugaresi, P. Gambetti and S. B. Prusiner (1996). "Evidence for the conformation of the pathologic isoform of the prion protein enciphering and propagating prion diversity." Science **274**(5295): 2079-2082.

Theint, T., Y. Xia, P. S. Nadaud, D. Mukhopadhyay, C. D. Schwieters, K. Surewicz, W. K. Surewicz and C. P. Jaroniec (2018). "Structural Studies of Amyloid Fibrils by Paramagnetic Solid-State Nuclear Magnetic Resonance Spectroscopy." J Am Chem Soc **140**(41): 13161-13166.

Tranulis, M. A., D. Gavier-Widen, J. Vage, M. Noremark, S. L. Korpenfelt, M. Hautaniemi, L. Pirisinu, R. Nonno and S. L. Benestad (2021). "Chronic wasting disease in Europe: new strains on the horizon." Acta Vet Scand **63**(1): 48.

Turk, E., D. B. Teplow, L. E. Hood and S. B. Prusiner (1988). "Purification and properties of the cellular and scrapie hamster prion proteins." Eur J Biochem **176**(1): 21-30.

Tycko, R., R. Savtchenko, V. G. Ostapchenko, N. Makarava and I. V. Baskakov (2010). "The alpha-helical C-terminal domain of full-length recombinant PrP converts to an in-register parallel beta-sheet structure in PrP fibrils: evidence from solid state nuclear magnetic resonance." Biochemistry **49**(44): 9488-9497.

Tzaban, S., G. Friedlander, O. Schonberger, L. Horonchik, Y. Yedidia, G. Shaked, R. Gabizon and A. Taraboulos (2002). "Protease-sensitive scrapie prion protein in aggregates of heterogeneous sizes." Biochemistry **41**(42): 12868-12875.

Urwin, P. J., J. M. Mackenzie, C. A. Llewelyn, R. G. Will and P. E. Hewitt (2016). "Creutzfeldt-Jakob disease and blood transfusion: updated results of the UK Transfusion Medicine Epidemiology Review Study." Vox Sang **110**(4): 310-316.

van der Kamp, M. W. and V. Daggett (2010). "Pathogenic mutations in the hydrophobic core of the human prion protein can promote structural instability and misfolding." J Mol Biol **404**(4): 732-748.

Vázquez-Fernández, E., M. R. Vos, P. Afanasyev, L. Cebey, A. M. Sevillano, E. Vidal, I. Rosa, L. Renault, A. Ramos, P. J. Peters, J. J. Fernandez, M. van Heel, H. S. Young, J. R. Requena and H. Wille (2016). "The Structural Architecture of an Infectious Mammalian Prion Using Electron Cryomicroscopy." PLoS Pathog **12**(9): e1005835.

Vázquez-Fernández, E., H. S. Young, J. R. Requena and H. Wille (2017). "The Structure of Mammalian Prions and Their Aggregates." Int Rev Cell Mol Biol **329**: 277-301.

Wadsworth, J. D., A. F. Hill, S. Joiner, G. S. Jackson, A. R. Clarke and J. Collinge (1999). "Strain-specific prion-protein conformation determined by metal ions." Nat Cell Biol **1**(1): 55-59.

Wadsworth, J. D. F., S. Joiner, J. M. Linehan, K. Jack, H. Al-Doujaily, H. Costa, T. Ingold, M. Taema, F. Zhang, M. K. Sandberg, S. Brandner, L. Tran, T. Vikoren, J. Vage, K. Madslien, B. Ytrehus, S. L. Benestad, E. A. Asante and J. Collinge (2022). "Humanized Transgenic Mice Are Resistant to Chronic Wasting Disease Prions From Norwegian Reindeer and Moose." J Infect Dis **226**(5): 933-937.

Walter, E. D., M. Chattopadhyay and G. L. Millhauser (2006). "The affinity of copper binding to the prion protein octarepeat domain: evidence for negative cooperativity." Biochemistry **45**(43): 13083-13092.

Walter, E. D., D. J. Stevens, A. R. Spevacek, M. P. Visconte, A. Dei Rossi and G. L. Millhauser (2009). "Copper binding extrinsic to the octarepeat region in the prion protein." Curr Protein Pept Sci **10**(5): 529-535.

Walter, E. D., D. J. Stevens, M. P. Visconte and G. L. Millhauser (2007). "The prion protein is a combined zinc and copper binding protein: Zn2+ alters the distribution of Cu2+ coordination modes." J Am Chem Soc **129**(50): 15440-15441.

Wan, W., H. Wille, J. Stohr, A. Kendall, W. Bian, M. McDonald, S. Tiggelaar, J. C. Watts, S. B. Prusiner and G. Stubbs (2015). "Structural studies of truncated forms of the prion protein PrP." Biophys J **108**(6): 1548-1554.

Wang, F., S. Yin, X. Wang, L. Zha, M. S. Sy and J. Ma (2010). "Role of the highly conserved middle region of prion protein (PrP) in PrP-lipid interaction." Biochemistry **49**(37): 8169-8176.

Wang, L. Q., K. Zhao, H. Y. Yuan, X. N. Li, H. B. Dang, Y. Ma, Q. Wang, C. Wang, Y. Sun, J. Chen, D. Li, D. Zhang, P. Yin, C. Liu and Y. Liang (2021). "Genetic prion disease-related mutation E196K displays a novel amyloid fibril structure revealed by cryo-EM." Sci Adv **7**(37): eabg9676.

Wang, L. Q., K. Zhao, H. Y. Yuan, Q. Wang, Z. Guan, J. Tao, X. N. Li, Y. Sun, C. W. Yi, J. Chen, D. Li, D. Zhang, P. Yin, C. Liu and Y. Liang (2020). "Cryo-EM structure of an amyloid fibril formed by full-length human prion protein." Nat Struct Mol Biol **27**(6): 598-602.

Wang, Z., K. Qin, M. V. Camacho, I. Cali, J. Yuan, P. Shen, J. Greenlee, Q. Kong, J. A. Mastrianni and W. Q. Zou (2021). "Generation of human chronic wasting disease in transgenic mice." Acta Neuropathol Commun **9**(1): 158.

Weissmann, C. (2004). "The state of the prion." Nat Rev Microbiol **2**(11): 861-871.

Wells, G. A., A. C. Scott, C. T. Johnson, R. F. Gunning, R. D. Hancock, M. Jeffrey, M. Dawson and R. Bradley (1987). "A novel progressive spongiform encephalopathy in cattle." Vet Rec **121**(18): 419-420.

Wells, M. A., G. S. Jackson, S. Jones, L. L. Hosszu, C. J. Craven, A. R. Clarke, J. Collinge and J. P. Waltho (2006). "A reassessment of copper(II) binding in the full-length prion protein." Biochem J **399**(3): 435-444.

Westaway, D., V. Zuliani, C. M. Cooper, M. Da Costa, S. Neuman, A. L. Jenny, L. Detwiler and S. B. Prusiner (1994). "Homozygosity for prion protein alleles encoding glutamine-171 renders sheep susceptible to natural scrapie." Genes Dev **8**(8): 959-969.

Westergard, L., J. A. Turnbaugh and D. A. Harris (2011). "A naturally occurring C-terminal fragment of the prion protein (PrP) delays disease and acts as a dominant-negative inhibitor of PrPSc formation." J Biol Chem **286**(51): 44234-44242.

Wik, L., S. Mikko, M. Klingeborn, M. Steen, M. Simonsson and T. Linne (2012). "Polymorphisms and variants in the prion protein sequence of European moose

(Alces alces), reindeer (Rangifer tarandus), roe deer (Capreolus capreolus) and fallow deer (Dama dama) in Scandinavia." Prion **6**(3): 256-260.

Will, R. G., J. W. Ironside, M. Zeidler, S. N. Cousens, K. Estibeiro, A. Alperovitch, S. Poser, M. Pocchiari, A. Hofman and P. G. Smith (1996). "A new variant of Creutzfeldt-Jakob disease in the UK." Lancet **347**(9006): 921-925.

Wille, H., W. Bian, M. McDonald, A. Kendall, D. W. Colby, L. Bloch, J. Ollesch, A. L. Borovinskiy, F. E. Cohen, S. B. Prusiner and G. Stubbs (2009). "Natural and synthetic prion structure from X-ray fiber diffraction." Proc Natl Acad Sci U S A **106**(40): 16990-16995.

Wille, H., L. Dorosh, S. Amidian, G. Schmitt-Ulms and M. Stepanova (2019). "Combining molecular dynamics simulations and experimental analyses in protein misfolding." Adv Protein Chem Struct Biol **118**: 33-110.

Wille, H., C. Govaerts, A. Borovinskiy, D. Latawiec, K. H. Downing, F. E. Cohen and S. B. Prusiner (2007). "Electron crystallography of the scrapie prion protein complexed with heavy metals." Arch Biochem Biophys **467**(2): 239-248.

Wille, H., M. D. Michelitsch, V. Guenebaut, S. Supattapone, A. Serban, F. E. Cohen, D. A. Agard and S. B. Prusiner (2002). "Structural studies of the scrapie prion protein by electron crystallography." Proc Natl Acad Sci U S A **99**(6): 3563-3568.

Wille, H., M. Shanmugam, M. Murugesu, J. Ollesch, G. Stubbs, J. R. Long, J. G. Safar and S. B. Prusiner (2009). "Surface charge of polyoxometalates modulates polymerization of the scrapie prion protein." Proceedings of the National Academy of Sciences **106**(10): 3740-3745.

Williams, E. S. (2003). "Scrapie and chronic wasting disease." Clin Lab Med **23**(1): 139-159.

Williams, E. S. (2005). "Chronic wasting disease." Vet Pathol **42**(5): 530-549.

Williams, E. S. and M. W. Miller (2002). "Chronic wasting disease in deer and elk in North America." Rev Sci Tech **21**(2): 305-316.

Williams, E. S. and S. Young (1980). "Chronic wasting disease of captive mule deer: a spongiform encephalopathy." J Wildl Dis **16**(1): 89-98.

Wilson, R., C. Plinston, N. Hunter, C. Casalone, C. Corona, F. Tagliavini, S. Suardi, M. Ruggerone, F. Moda, S. Graziano, M. Sbriccoli, F. Cardone, M. Pocchiari, L. Ingrosso, T. Baron, J. Richt, O. Andreoletti, M. Simmons, R. Lockey, J. C. Manson and R. M. Barron (2012). "Chronic wasting disease and atypical forms of bovine spongiform encephalopathy and scrapie are not transmissible to mice expressing wild-type levels of human prion protein." J Gen Virol **93**(Pt 7): 1624-1629.

Yu, K. H., M. Y. Huang, Y. R. Lee, Y. K. Lin, H. R. Chen and C. I. Lee (2021). "The Effect of Octapeptide Repeats on Prion Folding and Misfolding." Int J Mol Sci **22**(4): 1800.

Zahn, R., A. Liu, T. Luhrs, R. Riek, C. von Schroetter, F. Lopez Garcia, M. Billeter, L. Calzolai, G. Wider and K. Wuthrich (2000). "NMR solution structure of the human prion protein." Proc Natl Acad Sci U S A **97**(1): 145-150.

Zhou, H. X. and X. Pang (2018). "Electrostatic Interactions in Protein Structure, Folding, Binding, and Condensation." Chem Rev **118**(4): 1691-1741.

Ziarek, J. J., D. Baptista and G. Wagner (2018). "Recent developments in solution nuclear magnetic resonance (NMR)-based molecular biology." J Mol Med (Berl) **96**(1): 1-8.